



UPPSALA  
UNIVERSITET

*Digital Comprehensive Summaries of Uppsala Dissertations  
from the Faculty of Science and Technology 1767*

# Angle dependent light scattering of functional nanoparticle composites

JUNXIN WANG



ACTA  
UNIVERSITATIS  
UPSALIENSIS  
UPPSALA  
2019

ISSN 1651-6214  
ISBN 978-91-513-0559-2  
urn:nbn:se:uu:diva-374319

Dissertation presented at Uppsala University to be publicly examined in Polhemsalen, Ångströmlaboratoriet, Lägerhyddsvägen 1, Uppsala, Friday, 8 March 2019 at 13:15 for the degree of Doctor of Philosophy. The examination will be conducted in English. Faculty examiner: Professor Anand Srinivason (KTH Royal Institute of Technology).

### **Abstract**

Wang, J. 2019. Angle dependent light scattering of functional nanoparticle composites. *Digital Comprehensive Summaries of Uppsala Dissertations from the Faculty of Science and Technology* 1767. 89 pp. Uppsala: Acta Universitatis Upsaliensis. ISBN 978-91-513-0559-2.

Varies functional nanoparticles play crucial roles in energy- and optical- related applications. The incorporation of functional nanoparticles into non-absorbing polymers to form optical absorption and scattering thin films have attracted considerable interest due to a successful selection of particles and matrices, synergistic effects of separation and fixation of particles, and controllable layer thicknesses and structures. To investigate the optical parameters, especially absorption and scattering coefficients of the nanocomposites, it is critical to evaluate and optimize those particle based functional layers.

In this thesis, we mainly focus on developing approaches for the inversion of scattering and absorption coefficients from optically measured transmittance and reflectance spectra. A two-flux radiative transfer model is robust for this purpose, but its limitation lies in failing to converge the transmittance and reflectance spectra to experimental data owing to the approximation of the completely diffuse scattering patterns. We carried out thorough characterization of angle- and wavelength-resolved light scattering on those nanocomposites with metallic Au, ferromagnetic  $\text{Fe}_3\text{O}_4$  and photocatalytic  $\text{TiO}_2$  nanoparticles. We further developed an empirical scattering phase function, which can fully represent the scattering distributions for aggregated particles in the multiple scattering regime, as well as the single scattering in the Rayleigh, Mie and geometric optical scattering regimes. The incorporation of angle-resolved data into the two-flux theory to derive scattering and absorption coefficients have been validated using the functional nanoparticle composites. Several approximations are also proposed to obtain the scattering and absorption coefficients when angle resolved measurements were not available.

The optical performance was investigated on the nanocomposites mentioned above with varied sizes, shapes and concentrations using a spectrophotometer, an in-plane scatterometer and an out-of-plane goniometer. Single particle dark-field scattering spectra were also obtained for Au,  $\text{Fe}_3\text{O}_4$ , and  $\text{TiO}_2$  particles in the forward and backward directions.

*Keywords:* light scattering, nano particle, absorption, radiative transfer

*JunXin Wang, Department of Engineering Sciences, Solid State Physics, Box 534, Uppsala University, SE-751 21 Uppsala, Sweden.*

© JunXin Wang 2019

ISSN 1651-6214

ISBN 978-91-513-0559-2

urn:nbn:se:uu:diva-374319 (<http://urn.kb.se/resolve?urn=urn:nbn:se:uu:diva-374319>)

# List of Papers

This thesis is based on the following papers, which are referred to in the text by their Roman numerals.

- I Wang, J. X., Xu, C. G., Nilsson, A. M., Fernandes, D. L. A., Strömberg, M., Wang, J. F., Niklasson, G. A. (2019) General method for determining light scattering and absorption of nano-particle composites. *Adv. Opt. Mater.*, DOI: 10.1002/adom.201801315
- II Wang, J. X., Xu, C. G., Nilsson, A. M., Fernandes, D. L. A., Niklasson, G. A. (2019) Phase function of colloidal nanospheres in a layer from light scattering measurements. *Submitted*
- III Wang, J. X., Xu, C. G., Nilsson, A. M., Strömberg, M., Niklasson, G. A. (2019) Extraction of backscattering and absorption coefficients of magnetite nanosphere composites from light scattering measurements. *Manuscript*
- IV Wang, J. X., Nilsson, A. M., Wang, J. F., Niklasson, G. A. (2019) Direct spectrophotometric determination of light absorption and scattering parameters of colloidal gold nanoparticles. *Manuscript*

Reprints were made with permission from the respective publishers.

# My contribution to the appended papers

- I Part of the method design, most of the optical measurements, part of the sample preparation, most of the calculations, and part of the writing.
- II Part of sample preparation and optical measurements, most of the calculations and writing.
- III All calculations, part of sample preparation and optical measurements, and most of the writing.
- IV All optical measurements and calculations, part of sample preparation, and most of the writing.

Reprints were made with permission from the respective publishers.

## Publications not included in the thesis

- I     Yang, J. J., Wang, J. X., Strømme, M. Welch, K. (2019) Enhanced UV protection and water adsorption properties of transparent poly(methyl methacrylate) films through incorporation of amorphous magnesium carbonate nanoparticles. *Submitted*
- II    Wang, J. X., Nilsson, A. M., Fernandes, D. L. A., Niklasson, G. A. (2016) Angle dependent light scattering by gold nanospheres. *J. Phys.: Conf. Ser.* 682, 012018



# Contents

1. Introduction.....	11
1.1 Motivation and objective.....	12
1.2 Thesis outline .....	13
2. Scattering of light.....	15
2.1 Extinction, scattering and absorption of a medium containing nanoparticles.....	15
2.2 Classification of scattering processes.....	16
2.3 Mie theory .....	17
2.4 Scattering by a nanocomposite layer.....	22
2.5 Radiative transfer and N-flux theory.....	23
2.6 Angular distribution of light scattering .....	25
3. Material Synthesis and Characterization.....	32
3.1 Synthesis of nanoparticles and composite layers .....	32
3.2 Optical microscopy (OM) .....	33
3.3 Scanning electron spectroscopy (SEM) .....	34
3.4 Dynamic light scattering (DLS) .....	35
3.5 X-ray diffraction (XRD).....	35
4. Optical Characterization .....	37
4.1 Spectrophotometry .....	37
4.2 In-plane angle resolved scatterometer.....	38
4.3 Angle correction by Harvey's method .....	39
4.4 Out-of-plane goniometer .....	42
4.5 Single-particle scattering system.....	43
5. Results.....	44
5.1 Structure and morphology characterization.....	44
5.2 Measured transmittance and reflectance spectra .....	46
5.3 Three dimensional out-of-plane light scattering of nanoparticle composite layers.....	49
5.4 In-plane angle resolved results .....	53
5.5 Integration of angle resolved data .....	56
5.6 Conversion of angle resolved data into scattering phase function .....	57
5.7 Comparison of different scattering phase functions.....	60
5.8 Single-particle spectra for Au, Fe <sub>3</sub> O <sub>4</sub> and TiO <sub>2</sub> nanospheres .....	65

6. Determination of scattering and absorption coefficients from spectrophotometric data .....	68
6.1 Previous methods to determine scattering and absorption coefficients .....	68
6.2 New methods using angle resolved scattering information.....	69
6.3 Backscattering and absorption coefficients inversion of Kubelka-Munk model .....	71
6.4 Size dependent backscattering and absorption coefficients inversion of Kubelka-Munk model .....	74
7. Conclusions and future work .....	77
7.1 Conclusions .....	77
7.2 Future work .....	78
8. Swedish summary (Svensk sammanfattning) .....	80
Acknowledgements.....	82
References.....	84



# Abbreviations

SEM	scanning electron microscopy
XRD	X-ray diffraction
DLS	dynamic light scattering
ARS	angle resolved scattering
BSDF	bidirectional scattering distribution function
BRDF	bidirectional reflectance distribution function
BTDF	bidirectional transmittance distribution function
$T$	transmittance
$R$	reflectance
$T_{\text{tot}}$	total transmittance
$T_{\text{dif}}$	diffuse transmittance
$T_{\text{reg}}$	regular transmittance
$R_{\text{tot}}$	total reflectance
$R_{\text{dif}}$	diffuse reflectance
$R_{\text{spe}}$	specular reflectance
$S$	backscattering coefficient
$K$	absorption coefficient
$E$	extinction coefficient
$R_{\text{d}}$	diffuse reflectance
$R_{\text{df}}$	diffuse reflectance in forward direction
$R_{\text{db}}$	diffuse reflectance in backward direction
$R_{\text{c}}$	specular reflectance
$R_{\text{g}}$	total reflectance of the backside glass/air interface
$R_{\text{j}}$	total reflectance of the frontside glass/air interface
$q_0$	diffuse light fractions in the film close to the back interface
$q_{\text{d}}$	diffuse light fractions in the film close to the front interface
$d$	thickness of scattering layer
KM	Kubelka-Munk
$T_{\text{KM}}$	Kubelka-Munk approximation of transmittance
$R_{\text{KM}}$	Kubelka-Munk approximation of reflectance
HG	Henyey-Greenstain
RM	Reynolds-McCormick
CS	Cornette-Shanks
FF	Forand-Fournier
PARA	parabolic
MSLE	mean square logarithmic error

OT	one-term
TT	two-term
RTE	radiative transfer equation

# 1. Introduction

With the rise of nanotechnology, functional nanoparticles are playing crucial roles in energy- and optical- related applications. Tunable optical performance based on the size, shape, and types of the nanoparticles gives rise to a multitude of applications for pigment technology<sup>1-4</sup>, solids state lighting<sup>5</sup> and particle based optical devices<sup>6-8</sup>. Among these nanoparticles, the noble metal nanoparticles, for example gold, exhibit localized plasmon resonances in the visible region, and form the basis for the rapidly expanding field of plasmonics. Plasmonic materials exhibit enhanced light absorption and scattering and large electric field enhancement at the resonances. They have attracted extensive attention for solar energy harvesting,<sup>7-8</sup> color displays,<sup>9</sup> optical antennas<sup>10</sup> and biosensing.<sup>11</sup> Recently, dielectric nanostructures have also attracted considerable interest<sup>12</sup> due to their strong electric and magnetic Mie resonances<sup>13</sup> and low absorption at optical frequencies.<sup>14</sup> These properties offer the opportunities as building blocks for the design and construction of metamaterials and metasurfaces. Iron oxide nanoparticles show interesting optical as well as magnetic properties and can be used in diagnostic applications<sup>15</sup>. Titanium oxide is a well-known white pigment used in the paper industry<sup>3</sup>, as a component in sunscreen cosmetics<sup>16</sup>, in strongly photocatalytic material<sup>17</sup>, in electrochromic display devices<sup>18</sup>, and in dye-sensitized solar cells<sup>19</sup>.

The incorporation of functional nanoparticles into polymers may generate a large number of applications through the synergistic effects of separation and fixation of the nanoparticles. These nanocomposites consisting of functional nanoparticles are used in many applications, for example pigmented paints,<sup>4</sup> translucent sheets,<sup>20</sup> UV-absorbing films,<sup>21</sup> radiative cooling layers<sup>22</sup>, dichroic materials<sup>23</sup>, nanocomposite thin films for surface-enhanced Raman scattering (SERS) measurements<sup>24</sup>, superparamagnetic material<sup>25</sup> and high refractive index coatings<sup>26</sup>. In these applications, nanoparticles are stabilized by inclusion in a surrounding matrix material, forming a composite layer. The characterization of the two energy-attenuation mechanisms, absorption, and especially scattering, are crucial to fully understanding optical behavior of such particle-embedded scattering layers, thus pave the way for design and optimizing the optical performance of these nanocomposites.

When the nanoparticles are much smaller than the wavelength of the incident light, the optical properties of such composites can be described by the effective medium theory<sup>27-28</sup> and the effective optical constants of the composite layer can be obtained by the inversion of experimental transmittance ( $T$ )

and reflectance ( $R$ ) measurements by the well-known methods of thin film optics<sup>29</sup>. However, when the particles are in the order of or larger than the wavelength of incident light, light scattering becomes significant. In this case the description of the optical properties becomes complicated and the definition of the effective optical parameters of a composite layer is not straightforward.

The relation between reflectance and transmittance and the intrinsic optical scattering/absorption parameters of a nanocomposite can be described by Kubelka-Munk two-flux theory, but the inversion of measured data to obtain optical parameters has been notoriously difficult. The main difficulty lies in the prediction of the front and back interface reflectances inside the scattering layer. The reflectance requires a full characterization of the angular dependence of impinging light inside the scattering layer. Previous inversion procedures assume an isotropic scattering pattern of the particles, which fail to converge to the experimental transmittance and reflectance data.<sup>30</sup> Therefore, a thorough characterization of scattering behavior as a function of angle and wavelength is essential. Conversion between the outer measured angle resolved results into inner scattering phase function has been developed. Due to total internal reflection, the converted inner scattering phase function covers part of the whole angle range. Different empirical scattering phase functions are compared by fitting into experimental results. From the angle-resolved results, we further propose several approximations of the angular scattering profiles which are validated by our samples when angular measurements are not available. By the use of experimental angle resolved measurements, this approach can be extended to a wide range of isotropic, anisotropic and multiple scattering systems.

## 1.1 Motivation and objective

The motivation of this thesis was to obtain the scattering and absorption coefficients of light scattering materials from experimental measured transmittance and reflectance spectra.

We focus on materials having light scattering nanoparticles in a weakly absorbing (polymer) matrix. Such nanocomposite materials are becoming increasingly important, especially in photonics, where they make fascinating features possible. We choose different nanoparticles, for instance, metallic and dielectric nanoparticles with medium to high refractive indices. We want to explore the scattering performance of these nanocomposites. Therefore, the size of the nanoparticles is of the order of the wavelength, exhibiting a high scattering efficiency. In such nanocomposites, the effective medium theory is no longer valid since it assumes that scattering can be ignored. A two-flux radiative transfer approach is used to model the absorption and scattering coefficients. The limitation of two flux theory is that the interface reflectances

are unknown. To determine these quantities, the scattering phase function of the nanoparticles inside the layer is required.

Our objective is first to explore the transmittance and reflectance spectra of such functional nanoparticle composites, and to understand how these spectra are related to the materials properties, i.e., color and bandgap. The dependence of size, shape, concentration, and thickness of the composite layers should be explored. The transmittance and reflectance spectra give information in the forward and backward hemispheres as a whole. The scattering process is angle dependent, and a full characterization of the scattering as a function of angle needs to be carried out by means of an in-plane scatterometer and an out-of-plane goniometer. The integrated angle-resolved scattering results should be compared with total transmittance and reflectance spectra. How to relate the outer measured angle-resolved intensity to the scattering phase function inside the nanocomposite is critical. The converted inner scattering phase function can be compared with various empirical scattering phase functions, thus evaluating which empirical scattering phase functions are suitable in our study. The interface reflectance can then be obtained by integrating the inner scattering phase function over angle, in order finally to obtain scattering and absorption parameters.

Apart from the scattering measurements on nanoparticle composites, we intend to study light scattering on functional single nanospheres in the forward and backward directions by using a dark-field microscope equipped with a monochromator.

## 1.2 Thesis outline

In this doctoral thesis, the optical properties of plasmonic Au nanospheres and nanorods, ferromagnetic  $\text{Fe}_3\text{O}_4$  nanospheres and photocatalytic  $\text{TiO}_2$  nanospheres are studied. The optical measurements, especially the angular dependent light scattering measurements were carried out based on the above nanoparticle composites. Varied models are proposed and compared with the previous established methods to obtain the scattering and absorption parameters.

**Chapter 1** presents a brief introduction of the thesis, motivation and objective. **Chapter 2** gives background knowledge light scattering theory, the classification of the scattering process, Mie scattering theory, two-flux and many-flux theories, angle-resolved scattering, and bidirectional scattering distribution function. **Chapter 3** focuses on how the nanoparticles are synthesized and what types of techniques are used for material characterizations. In **Chapter 4**, optical performances of nanoparticle composites are studied by means of a spectrophotometer and angle and wavelength resolved scatterometer. **Chapter 5** presents the results of the structure and morphology of the nanoparticles, optical transmittance and reflectance, in-plane and out-of-plane angle-resolved results, comparison of different scattering phase functions and

single particle scattering spectra. **Chapter 6** summarizes previous methods to determine the scattering and absorption coefficients, and presents our approaches based on the angle-resolved light scattering and angle-free approximations.

## 2. Scattering of light

### 2.1 Extinction, scattering and absorption of a medium containing nanoparticles

Extinction is the attenuation of electromagnetic radiation when it passes through a medium.<sup>31</sup> The contribution to the extinction comes from the sum of both scattering and absorption. All waves incident on a particle are either absorbed or scattered.<sup>32</sup> Extinction, scattering and absorption can be quantified as extinction coefficient ( $\varepsilon$ ), scattering coefficient ( $\alpha$ ) and absorption coefficient ( $\beta$ ) by the relation:

$$\varepsilon = \alpha + \beta \quad (2.1)$$

The extinction is exponentially attenuated as a function of light path ( $d$ ) through the medium. The intensity reduces to  $I_t$  from the original  $I_0$ ,

$$\frac{I_t}{I_0} = \exp(-\varepsilon \cdot d) = \exp[-(\alpha + \beta) \cdot d] \quad (2.2)$$

However, it is difficult to separate the contribution from absorption and scattering. When the medium is homogeneous, the dominant attenuation comes from absorption, and the absorption coefficient can be approximately equal to the extinction coefficient. In a particulate medium, the scattering results from, for instance, the refractive index difference from the particle and the medium, the size of the particle, and volume fraction of the particle.

Scattering, absorption and extinction coefficients ( $\text{cm}^{-1}$ ) are related to particle cross sections ( $\text{cm}^2$ ) and particle density  $\rho$  ( $\text{cm}^{-3}$ ),

$$\varepsilon = \rho \cdot c_{\text{ext}} = \frac{f}{V} \cdot c_{\text{ext}} = \frac{f}{\frac{4}{3}\pi r^3} \cdot c_{\text{ext}} \quad (2.3)$$

$$\alpha = \rho \cdot c_{\text{sca}} = \frac{f}{V} \cdot c_{\text{sca}} = \frac{f}{\frac{4}{3}\pi r^3} \cdot c_{\text{sca}} \quad (2.4)$$

$$\beta = \rho \cdot c_{\text{abs}} = \frac{f}{V} \cdot c_{\text{abs}} = \frac{f}{\frac{4}{3}\pi r^3} \cdot c_{\text{abs}} \quad (2.5)$$

where  $c_{\text{ext}}$ ,  $c_{\text{abs}}$ ,  $c_{\text{sca}}$  are the extinction, absorption and scattering cross sections,  $f$  is the volume fraction,  $V$  is the volume of single nanosphere, and  $r$  is the radius of the nanosphere. The cross sections ( $c_{\text{ext}}$ ,  $c_{\text{abs}}$ ,  $c_{\text{sca}}$ ) are also related to the fractional efficiencies ( $Q_{\text{ext}}$ ,  $Q_{\text{abs}}$ ,  $Q_{\text{sca}}$ ),

$$c_{ext} = Q_{ext} \cdot A = Q_{ext} \cdot \pi r^2 \quad (2.6)$$

$$c_{abs} = Q_{abs} \cdot A = Q_{abs} \cdot \pi r^2 \quad (2.7)$$

$$c_{sca} = Q_{sca} \cdot A = Q_{sca} \cdot \pi r^2 \quad (2.8)$$

where  $A$  is the geometric cross section of the particle.

## 2.2 Classification of scattering processes

Scattering phenomena are classified in several different ways, i.e., single and multiple scattering, independent and dependent scattering, Rayleigh scattering ( $x < 0.1$ ), geometrical optics scattering ( $x > 20$ ), and Mie scattering (intermediate  $x$ ).<sup>33</sup> The size parameter is defined as  $2\pi r/\lambda$ , where  $r$  is the radius of the nanoparticle and  $\lambda$  is the wavelength of light.

Single particle scattering is when the electromagnetic plane wave impinges on a single particle which has a different refractive index from its surrounding medium. The scattering intensity is strongly dependent on the size parameter  $x$  and the ratio of the refractive index of the particle to the surrounding medium  $m$ . Mie first solved these problems of the spherical particle by using the Maxwell equation and appropriate boundary conditions.<sup>34</sup> Single scattering is different from multiple scattering. In a given volume containing  $N$  particles per unit volume, if a single ray passing the medium is only scattered once before leaving the medium, this is single scattering. If the scattering occurs more than once per single ray, this is multiple scattering. In single scattering region, the scattered intensity of the entire volume is simplified from the sum of the scattered intensity from an individual particle. For multiple scattering regions, differential radiative transfer equation is required. A simple way to test the existence of multiple scattering is to double the concentration of the particle and if the scattered intensity is doubled, then single scattering is dominant<sup>31</sup>. Another criterion is extinction, which is proportional to  $\exp(-\varepsilon \cdot d)$ , if  $(\varepsilon \cdot d)$  is smaller than 0.1, single scattering prevails; when  $(\varepsilon \cdot d)$  is in the range of 0.1 to 0.3, double scattering should be counted; for  $(\varepsilon \cdot d)$  larger than 0.3, then multiple scattering is dominant. Multiple scattering is complex, and no simple proportionality can be referred to.

The key factor determining the scattering is if it is independent scattering or dependent scattering. There are three nanoparticle-optical models depending on the particle volume fraction and the size parameter; namely, effective medium region, independent scattering region and dependent scattering region<sup>35</sup>, as shown in Figure 2.1. Dependent scattering happens when the scattering occurring in a single particle is influenced by the presence of its neighbors, while independent scattering is not affected by its neighbors. For example, van de Hulst<sup>31</sup> stated that independent scattering can be assumed if  $c/D > 0.5$ , where  $c$  is the distance between two particles and  $D$  is the diameter of the



particles. Hottel<sup>36</sup> et al introduced another parameter,  $c/\lambda$ , where  $\lambda$  is the wavelength of the incident light. They suggested the limits of independent scattering should be  $c/\lambda > 0.3$  and  $c/D > 0.4$ .

In the independent scattering region, the optical properties can be described in the framework of radiative transfer theory<sup>37</sup>. Effective medium theory<sup>27-28, 38</sup>, i.e., the Maxwell Garnett model<sup>39-40</sup> and the Bruggeman model<sup>41</sup>, is used when the containing particle diameter is much smaller than the wavelength of electromagnetic radiation, and the scattering process can be ignored.

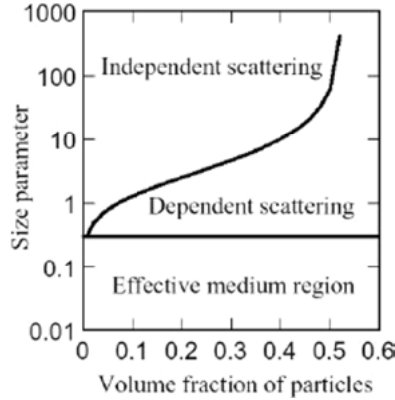


Figure 2.1. Three different models to predict the scattering behavior of a nanoparticle embedded coating. (adapted from reference<sup>35</sup>)

## 2.3 Mie theory

The scattering of light by a homogeneous sphere can be solved by Mie<sup>34</sup> using Maxwell's equation with the appropriate boundary conditions<sup>31</sup>. Non-spherical particles, such as cylindrical particles, are studied by the so-called T-matrix approach.<sup>42</sup> Particles with more complicated geometry can be solved by using the discrete-dipole approximation (DDA),<sup>43-44</sup> finite-element formulation,<sup>45</sup> and discrete source methods.<sup>46</sup> Among them, DDA approach is widely used for its conceptual simplicity. DDA is modeled by a collection of discrete interacting dipoles.

Mie theory<sup>34</sup> calculates the scattered electromagnetic field at all points within the particle and at all points of the homogeneous medium. The scattered field is carried out in the far-field zone, meaning at a large distance from a particle. The scattering from any finite particle can be characterized by its amplitude functions,  $S_1$ ,  $S_2$ ,  $S_3$  and  $S_4$ . Knowing these four parameters, the intensity and polarization of the scattered light, and the total scattering cross section of extinction, scattering and absorption can be calculated. For spherical particles, only  $S_1(\theta)$  and  $S_2(\theta)$  are required since  $S_3(\theta)$  and  $S_4(\theta)$  are equal to zero, where  $\theta$  is the scattering angle. The scattering phase function  $F(\theta, \varphi)$  defines

the intensity of the scattered light in an arbitrary direction, which is related by amplitude functions,

$$F(\theta, \varphi) = i_2(\theta) \cos^2(\varphi) + i_1(\theta) \sin^2(\varphi) \quad (2.9)$$

where  $i_1 = |S_1(\theta)|^2$  and  $i_2 = |S_2(\theta)|^2$ ,

the amplitude functions  $S_1(\theta)$  and  $S_2(\theta)$  are given by

$$S_1(\theta) = \sum_{n=1}^{\infty} \frac{2n+1}{n(n+1)} \{a_n \pi_n(\cos(\theta)) + b_n \tau_n(\cos(\theta))\} \quad (2.10)$$

$$S_2(\theta) = \sum_{n=1}^{\infty} \frac{2n+1}{n(n+1)} \{b_n \pi_n(\cos(\theta)) + a_n \tau_n(\cos(\theta))\} \quad (2.11)$$

The angle-dependent functions  $\pi_n$  and  $\tau_n$  are

$$\pi_n(\cos(\theta)) = \frac{1}{\sin(\theta)} P_n^1(\cos(\theta)) \quad (2.12)$$

$$\tau_n(\cos(\theta)) = \frac{d}{d(\theta)} P_n^1(\cos(\theta)) \quad (2.13)$$

The scattering coefficients  $a_n, b_n$ , are given by

$$a_n = \frac{m\psi_n(mx)\psi_n'(x) - \psi_n(x)\psi_n'(mx)}{m\psi_n(mx)\xi_n'(x) - \xi_n(x)\psi_n'(mx)} \quad (2.14)$$

$$b_n = \frac{\psi_n(mx)\psi_n'(x) - m\psi_n(x)\psi_n'(mx)}{\psi_n(mx)\xi_n'(x) - m\xi_n(x)\psi_n'(mx)} \quad (2.15)$$

The size parameter  $x$  and the relative refractive index  $m$  (the ratio of the refractive index of particles  $n_1$  to the refractive index of medium  $n_2$ ) are

$$x = \frac{2\pi r}{\lambda} \quad (2.16)$$

$$m = \frac{n_1}{n_2} \quad (2.17)$$

The scattering behaviour is influenced only by the diameter of the nanoparticle, the incident wavelength, and the refractive index of the particle and the medium. The extinction, scattering and absorption cross section can be calculated according to the following formulas:

$$c_{ext} = \frac{2\pi}{k^2} \sum_{n=1}^{\infty} (2n+1) \text{Re}(a_n + b_n) \quad (2.18)$$

$$c_{sca} = \frac{2\pi}{k^2} \sum_{n=1}^{\infty} (2n+1) (|a_n|^2 + |b_n|^2) \quad (2.19)$$

$$c_{abs} = c_{ext} - c_{sca} \quad (2.20)$$

The extinction, scattering and absorption efficiencies ( $Q_{ext}, Q_{sca}, Q_{abs}$ ) are defined as the extinction, scattering and absorption cross sections divided by the particles' physical cross section,  $\pi r^2$ . Figure 2.2 shows the  $Q_{ext}, Q_{sca}, Q_{abs}$  of gold nanosphere in the water medium simulated by Mie theory. The refractive

index of Au is adapted from Babar<sup>47</sup>. The absorption is dominant when particle size is much smaller than the wavelength of light (Figure 2.2a). Therefore,  $Q_{\text{ext}}$  and  $Q_{\text{abs}}$  almost overlap. When the particle size is in the order of the wavelength (Figure 2.2b), scattering becomes important. Figures 2.2c,d show those efficiencies when the particle size is further increased by one to two orders to the geometric optic regime. The scattering efficiency reaches its highest in Figure 2.2b, when the particle size is of the order of the wavelength. A smaller (Rayleigh scattering regime) or larger (geometric optics scattering regime) particle size reduces the scattering efficiency.

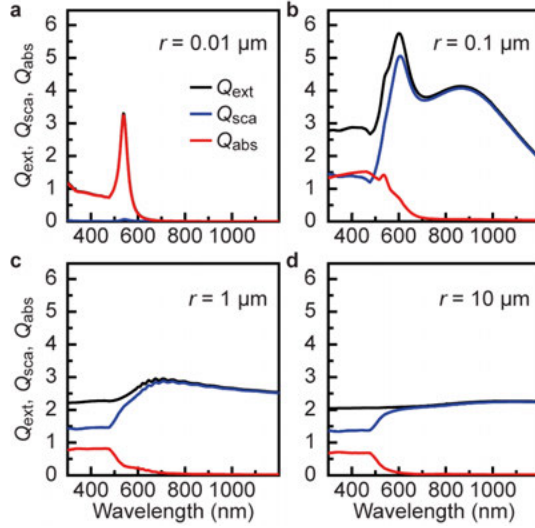


Figure 2.2. Extinction, scattering and absorption efficiencies  $Q_{\text{ext}}$ ,  $Q_{\text{sca}}$ ,  $Q_{\text{abs}}$  of a single Au nanosphere in water. The radii of the Au nanospheres are  $0.01 \mu\text{m}$  (a),  $0.1 \mu\text{m}$  (b),  $1 \mu\text{m}$  (c) and  $10 \mu\text{m}$  (d).

Figure 2.3 shows the scattering phase function of Au nanosphere in water as a function of the size of the nanosphere. The incident light is fixed at 600 nm. The radii of Au nanospheres are from  $0.01 \mu\text{m}$  till  $10 \mu\text{m}$ , corresponding to size parameters from 0.1, 1, 10.5 to 104.7. The peaked intensity value of phase function is increased with the larger size parameter. The scattering pattern is transformed from more isotropic one (Figure 2.3a) to forward peaked shapes (Figure 2.3b-d) as a result of larger size parameter.

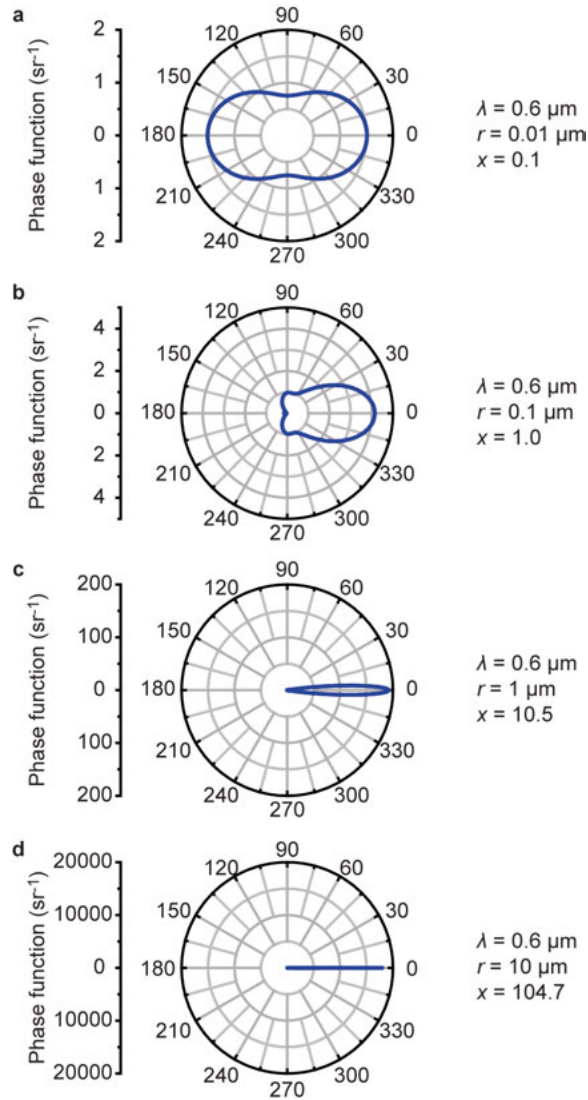


Figure 2.3. Scattering phase function of Au nanosphere in water. The wavelength of the incident light is 600 nm. The radius of the Au nanospheres are (a) 0.01  $\mu\text{m}$ , (b) 0.1  $\mu\text{m}$ , (c) 1  $\mu\text{m}$  and (d) 10  $\mu\text{m}$ .

Figure 2.4 shows the scattering phase function of Au nanosphere in water as a function of the incident light wavelength when the radius of the nanosphere is fixed at 100 nm. As a result, the size parameters are equal to 2.1 (when wavelength of incident light is 300 nm), 1.3 (500 nm), 0.9 (700 nm), and 0.7 (900 nm). The scattering peak intensity reduces as a result of reducing size parameter, and the scattering pattern becomes more isotropic for metallic spheres.

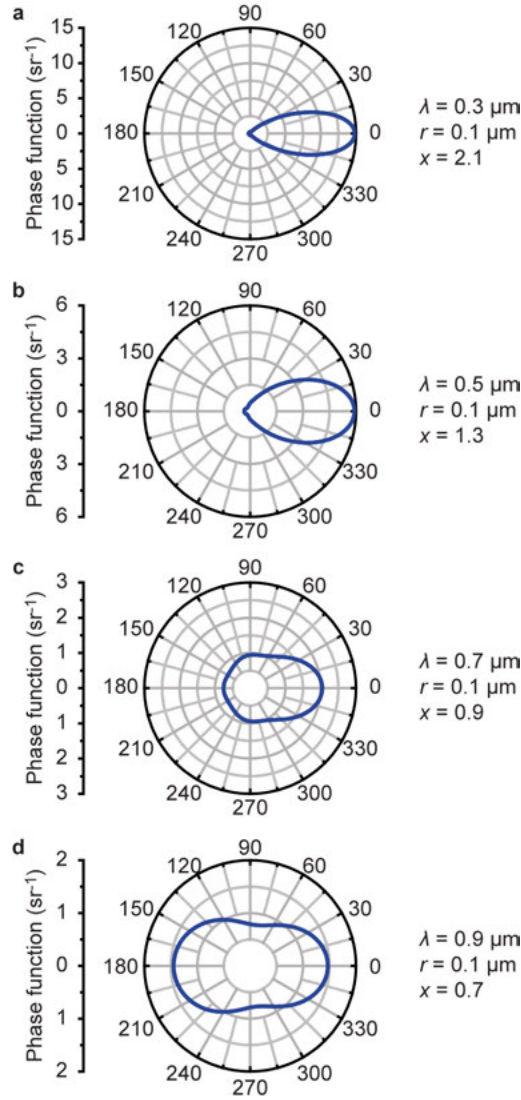


Figure 2.4. Scattering phase function of Au nanosphere in water. The radii of the Au nanospheres are 0.1 μm. The wavelengths of the incident lights are (a) 300, (b) 500, (c) 700, and (d) 900 nm.

With regard to dielectric spheres, the scattering phase function as a function of size parameters is shown in Figure 2.5 from Vargas et al.<sup>48</sup> As a result of an increment in the size parameter, the peak of the scattering pattern increases and the pattern tends to be dominated by the forward scattering.

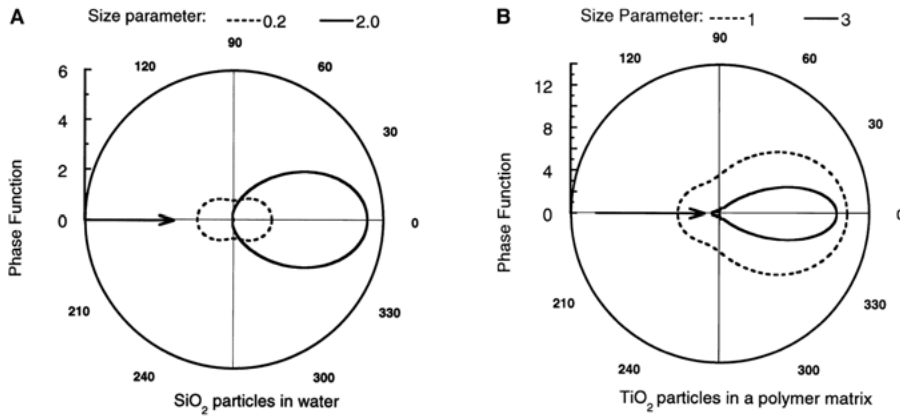


Figure 2.5. Polar plots of the phase function corresponding to (A) silica particles in water, and (B) titania pigments in a polymer matrix. The incident direction is from the left side of the figure. The particle size parameters are indicated. (B) In the phase function corresponding to  $x = 1$  has been multiplied by five. (adapted from reference<sup>48</sup>)

## 2.4 Scattering by a nanocomposite layer

In practical applications, the scattering happens with a cloud of nano/micro particles embedded in a layer of homogenous medium. Owing to the unique optical properties of nanoparticles together with tunable particle/medium refractive index contrast and particle volume fraction, the nanoparticle/medium composites' absorption/scattering spectra, transparency/reflectivity, specular/diffuse fraction, and the polarization of the hybrid system can all be tuned. Furthermore, the hybrid structure offers the probability of alignment of the nanoparticles by applying electrical, magnetic, thermal and shear fields<sup>49</sup>. The optical selectivity enables the nanoparticle composite materials to be applied as absorption/scattering enhanced layers in optoelectronic devices<sup>7</sup>, pigmented paints<sup>4</sup>, translucent sheets<sup>20</sup>, radiative cooling layers<sup>50</sup>, dichroism materials<sup>23</sup>, *etc.*

In a composite layer, if there is no surface scattering, then the volume scattering dominates. The transmitted region is the hemisphere where light propagates in the same direction as the incident light, while the reflectance region is the opposite hemisphere. If the composite is not opaque, a portion of the incident light is directly transmitted through the layer without interacting with the particle. The lower the  $(\epsilon \cdot d)$ , the more light is directly transmitted through the layer.

## 2.5 Radiative transfer and N-flux theory

Single scattering can be modeled by Mie theory, while multiple scattering can be numerically modeled with complex Monte Carlo simulations<sup>51-52</sup> or the radiative transfer equations (RTE)<sup>5, 53-55</sup>. RTE is the physical phenomenon of energy transfer in the form of electromagnetic wave. The radiative transfer process becomes:<sup>37</sup>

$$\mu \cdot \frac{\partial I(\tau, \mu)}{\partial \tau} = -I(\tau, \mu) + \frac{1}{2} \int_{-1}^1 p(\mu, \mu') I(\tau, \mu') d\mu' \quad (2.21)$$

where  $\tau$  is the optical depth which equals  $(\alpha + \beta)z$ ,  $\alpha$  and  $\beta$  are intrinsic scattering and absorption coefficients per unit length of the medium,  $z$  is a linear coordinate perpendicularly measured from the illuminated plane interface of the medium.  $\mu = \cos(\theta)$ , where  $\theta$  is the polar angle measured from the  $z$ -coordinate.  $I(\tau, \mu)$  is the intensity of the diffuse radiation emerging from multiple scattering events. The single particle phase function  $p(\mu, \mu')$  is the angular distribution of the radiation scattered by any of the particles in the medium. Within the Monte Carlo simulations of the radiative transfer approach,  $p(\mu, \mu')$  is the relative probability of a photon being scattered from the direction  $\theta'$  to the direction  $\theta$ . Varied analytical approaches<sup>56</sup> have been applied to solve the radiative transfer process under appropriate boundary conditions. A thorough review has been given by van de Hulst.<sup>57</sup> Monte Carlo simulations<sup>58-61</sup> have been extensively used to compute optical parameters of inhomogeneous media. Approximations with high numbers of flux channels permit an implicit description of the angular distribution of the propagating diffuse radiation.<sup>62-63</sup> For models with low flux channels, the computational implementation is quite simple, with accuracy sufficient for many applied science and technology applications.<sup>64</sup>

The first radiative transfer model of this type was formulated by Schuster<sup>65</sup> and Schwarzschild<sup>66</sup>, taking into account two isotropic diffuse components of the radiation field in the forward and backward hemispheres. In later studies by Kubelka and Munk<sup>67-68</sup>, a phenomenological two-flux model was proposed for analyzing the transmittance and reflectance of paint layers or other scattering coatings<sup>1, 69</sup>. The theory is formulated in terms of effective backscattering ( $S$ ) and absorption ( $K$ ) coefficients of the light scattering material, which are the fractions of backscattering/absorption of light per unit thickness. The Kubelka-Munk model is formulated in terms of two differential equations for radiation fluxes moving in the forward and backward direction in a material. It was originally derived for the case of completely diffuse radiation fluxes, but it can be reformulated in terms of total (the sum of collimated and diffuse) radiation fluxes in order to be applied to situations where the sample exhibits partly diffuse transmittance and reflectance<sup>2</sup>. The approximation tends to overestimate both attenuation by absorption and backscattering, and intensification by opposite-beam backscattering<sup>2</sup>. The total intensity in the forward  $I$  and backward  $J$  directions are coupled according to the differential equations:

$$\frac{dI}{dz} = -(S + K)I + SJ \quad (2.22)$$

$$\frac{dJ}{dz} = (S + K)J - SI \quad (2.23)$$

The solutions for the transmittance and reflectance for the case of a slab with backside internal reflectance  $R_g$  are given by

$$R_{KM} = \frac{1 - R_g[a - b \coth(bSd)]}{a - R_g + b \coth(bSd)} \quad (2.24)$$

$$T_{KM} = \frac{b(1 - R_g)}{(a - R_g) \sinh(bSd) + b \cosh(bSd)} \quad (2.25)$$

where  $a$  is equal to  $(1+K/S)$  and  $b$  is equal to  $(a^2-1)^{0.5}$ . Taking into account multiple reflections in the slab and reflections at the front interface we finally obtain

$$R = R_c + \frac{(1 - R_c)(1 - R_j)R_{KM}}{1 - R_j R_{KM}} \quad (2.26)$$

$$T = \frac{(1 - R_c)T_{KM}}{1 - R_j R_{KM}} \quad (2.27)$$

where  $R_c$  is the reflectance of the incident light on the front interface of the slab while  $R_j$  is the front side internal reflectance of the slab. It is seen that in order to invert the equations for  $R$  and  $T$ , in order to determine  $S$  and  $K$ , knowledge of the interface reflectance parameters is necessary. However, the calculation of these parameters from optical measurements is problematic, because the angular dependence of the radiation field in the material as well as the surface reflection coefficients are often not well characterized. Many flux models, *i.e.*, three-flux<sup>70-71</sup>, four-flux<sup>72</sup> and six-flux models<sup>73</sup> have been formulated. The four-flux model<sup>72</sup> provides simple relationships of regular transmittance and specular reflectance for non-scattering materials,

$$T_{reg} = \frac{(1 - R_c)^2 e^{-\varepsilon d}}{1 - R_c^2 e^{-2\varepsilon d}} \quad (2.28)$$

$$R_{spe} = R_c + \frac{R_c(1 - R_c)^2 e^{-2\varepsilon d}}{1 - R_c^2 e^{-2\varepsilon d}} \quad (2.29)$$

where  $R_c$  is the direct reflectance of the external interface, *i.e.*, glass/air interface, approximately equal to 0.04 if the refractive index of the glass is close to 1.5. With equation 2.28 and 2.29, direct reflectance  $R_c$  and extinction coefficient  $\varepsilon$  can be determined. The four-flux model is based on the following four coupled differential equations:

$$\frac{dI_c}{dz} = -(\alpha + \beta)I_c \quad (2.30)$$

$$\frac{dJ_c}{dz} = (\alpha + \beta)J_c \quad (2.31)$$



$$\frac{dI_d}{dz} = -\xi\beta I_d - \xi(1 - \sigma_d)\alpha I_d + \xi(1 - \sigma_d)\alpha J_d + \sigma_c\alpha I_c + (1 - \sigma_c)\alpha J_c \quad (2.32)$$

$$\frac{dJ_d}{dz} = \xi\beta J_d + \xi(1 - \sigma_d)\alpha J_d - \xi(1 - \sigma_d)\alpha I_d - \sigma_c\alpha J_c - (1 - \sigma_c)\alpha I_c \quad (2.33)$$

where  $\xi$  is an effective average pathlength parameter, ranging from 1 (totally collimated flux) to 2 (totally diffused flux).  $I$  and  $J$  denote the flux in the forward and backward directions. Subscript  $c$  and  $d$  denote collimated and diffused flux.  $\sigma_d$  is the forward scattering ratio for diffused flux, and  $\sigma_c$  is the forward scattering ratio for collimated flux. The models have been applied extensively using  $\sigma_c = \sigma_d$ <sup>74</sup>. The multiple scattering approach was introduced to calculate  $\xi$ ,  $\sigma_c$  and  $\sigma_d$ <sup>75-76</sup>. Four-flux model gives the scattering and absorption coefficients  $\alpha$  and  $\beta$ , while the two-flux model gives backscattering and absorption coefficients  $S$  and  $K$ , the relations between  $\alpha$  and  $\beta$  to  $S$  and  $K$  are<sup>77</sup>

$$\alpha = \frac{S}{\xi(1 - \sigma_d)} \quad (2.34)$$

$$\beta = \frac{K}{\xi} \quad (2.35)$$

From equation 2.4, 2.5, 2.34 and 2.35, the relation between  $S$ ,  $K$  to absorption and scattering cross sections from Mie theory can be obtained:

$$S = \frac{f}{\frac{4}{3}\pi r^3} \cdot c_{sca} \cdot \xi \cdot (1 - \sigma_d) \quad (2.36)$$

$$K = \frac{f}{\frac{4}{3}\pi r^3} \cdot c_{abs} \cdot \xi \quad (2.37)$$

## 2.6 Angular distribution of light scattering

Since the diffuse transmittance and reflectance are angular dependent, accurate characterization of the angle and wavelength dependence of radiation fluxes is essential. Light flux distributions are quantified by the Angle Resolved Scattering (ARS) function<sup>78-79</sup>. ARS corresponds to the radiant intensity portion within a solid angle, defined as the light power  $P_s$  scattered into a solid angle  $\Omega$  normalized by that solid angle and the incident light power  $P_i$

$$ARS(\beta) = \frac{P_s(\beta)}{P_i \times \Omega} \quad (2.38)$$

where  $\beta$  is the scattering angle.

Apart from ARS, the alternative bidirectional scattering distribution function (BSDF) represents the surface radiance scaled by the irradiance<sup>80-81</sup>. BSDF can be obtained by ARS with an additional cosine factor for the correction of the viewing angle:

$$\text{BSDF}(\beta) = \frac{\text{ARS}(\beta)}{\cos(\beta)} \quad (2.39)$$

The phase function (denoted as  $f$ ) is the angular distribution of light intensity scattered by a particle at a given wavelength.<sup>82</sup> It is given at an angle  $\theta$  which is relative to the incident light. It is the intensity (radiance) at  $\theta$ ,  $F(\theta)$ , relative to the normalized integral of the scattered intensity at all angles,<sup>82</sup>

$$f(\theta) = \frac{F(\theta)}{\int_0^\pi F(\theta) \sin(\theta) d\theta} \quad (2.40)$$

If the scattering is measured from a plane surface, phase function should be represented by BSDF which takes the viewing angle into consideration.

Scattering phase function can be derived by Mie theory<sup>31</sup> if the particle is comparable to the wavelength of light, and Rayleigh scattering if particle size  $< 1/10$  wavelength. The Rayleigh phase function describes the angular scattering distribution of unpolarized light by small particles.<sup>83</sup>

$$P_{\text{Rayleigh}}(\theta) = \frac{3}{4}(1 + \cos(\theta))^2 \quad (2.41)$$

The Rayleigh scattering function is symmetric, with maxima at  $0^\circ$  and  $180^\circ$  while minima appear at  $90^\circ$  and  $270^\circ$ . Mie and Rayleigh models give the solutions for angular distribution of a single particle. For multiple scattering with interactions between particles, we can refer to the empirical phase functions to approximate the angular functions. We first review a number of empirical phase functions that have been proposed previously. Reynold and McCormick (RM) proposed a phase function approximation which described highly anisotropic angular scattering distributions and has the following analytic form:<sup>84</sup>

$$f_{\text{RM}}(\theta, g, \alpha) = \frac{\alpha g(1 - g^2)^{2\alpha}}{\pi[1 + g^2 - 2g \cos(\theta)]^{\alpha+1}[(1 + g)^{2\alpha} - (1 - g)^{2\alpha}]} \quad (2.42)$$

When the fitting parameter  $\alpha$  equals 0.5, it reduces to the so-called Henyey-Greenstein (HG) phase function<sup>85</sup>:

$$f_{\text{HG}}(\theta, g) = \frac{1}{4\pi} \frac{1 - g^2}{[1 + g^2 - 2g \cos(\theta)]^{\frac{3}{2}}} \quad (2.43)$$

where  $g$  is the asymmetry factor, ranging from backscattering (-1) through isotropic scattering (0) to forward scattering (1). The HG function can also be writtent as an expansion of Legendre polynomials,  $P_n$ ,<sup>86</sup>

$$f_{\text{HG}}(\cos \theta, g) = \int_0^\infty (2n + 1) g^n P_n(\cos \theta) \quad (2.44)$$

The advantage of the RM phase function as compared to the HG phase function is that it better reproduces strongly anisotropic scattering angular distributions. However, both of them can fit only forward-peaked or backward-peaked scattering distributions, and fail for distributions that are both forward-

and backward- peaked. In order to overcome this deficiency and better represent the backscattering peak, a two-term modified HG phase function has been proposed (TTHG),<sup>87</sup>

$$f_{TTHG}(\theta, \gamma, g_1, g_2) = \gamma f_{HG}(\theta, g_1) + (1 - \gamma) f_{HG}(\theta, g_2) \quad (2.45)$$

This function has two parts with two different asymmetry factors, where  $g_1$  is positive and  $g_2$  is negative, in order to treat the forward and backward peaks in the phase function. The parameter  $\gamma$  gives the forward scattering fraction while  $(1-\gamma)$  is the backward scattering fraction. Since HG is a special case of RM when fitting parameter  $\alpha$  equals to 0.5, we therefore present the data on the fitting of HG and TTHG. Figure 2.6 shows the scattering phase functions simulated by HG with positive and negative asymmetry factor  $g$  (a,b) and TTHG (c). The HG phase function exhibits forward scattering peak with positive  $g$  and a backward scattering peak with negative  $g$ . However, both of them show monotonically increase or decrease trends, but fail to fit for profiles with both forward and backward peaks. Figure 2.6c gives examples of TTHG fits with different fitting parameters,  $g_1$ ,  $g_2$  and  $\gamma$ . TTHG can produce scattering phase function with both forward and backward peaked shapes. The profile shows a dominant forward scattering when  $\gamma$  is larger than 0.5 and a dominant backward scattering with  $\gamma$  less than 0.5.

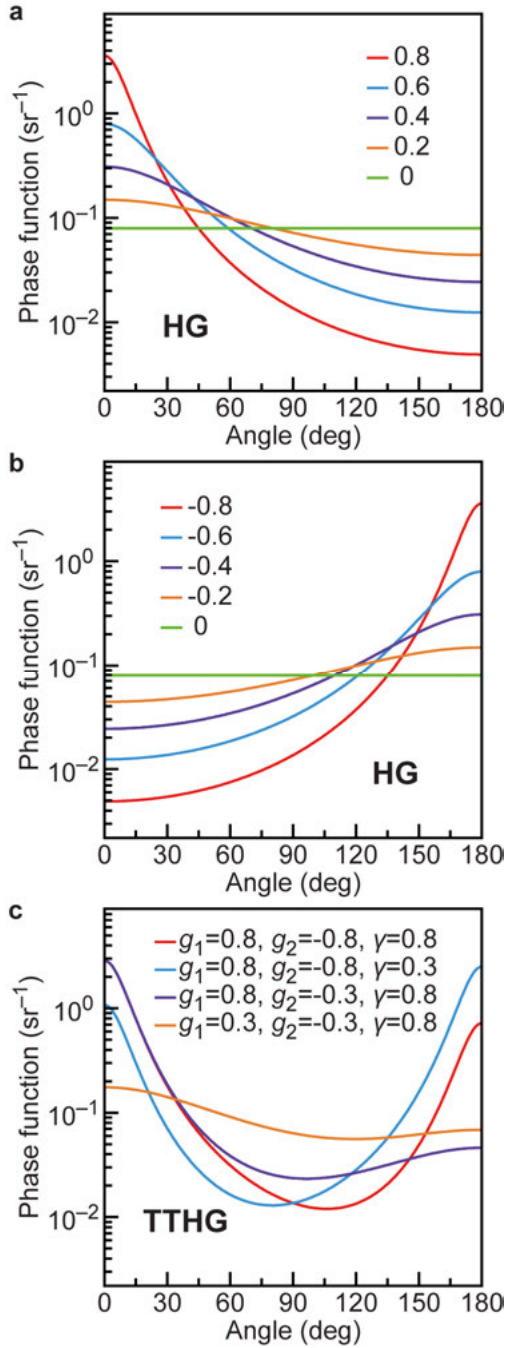


Figure 2.6. (a) Scattering phase function simulated from HG approximation with different asymmetry factor  $g$  from 0.8 to 0. (b) Scattering phase function simulated from HG approximation with different asymmetry factor  $g$  from -0.8 to 0. (c) Scattering phase function simulated from TTHG approximation with different asymmetry factor  $g_1$ ,  $g_2$ , and forward scattering portion  $\gamma$ .

Guided by the TTHG, we have revised the RM function in a similar way, and we denote this function as the two-term Reynolds-McCormick or TTRM phase function:

$$f_{TTRM}(\theta, g_1, g_2, \alpha_1, \alpha_2, \gamma) = \gamma f_{RM}(\theta, g_1, \alpha_1) + (1 - \gamma) f_{RM}(\theta, g_2, \alpha_2) \quad (2.46)$$

Compared to TTHG, TTRM has two more fitting parameters, namely  $\alpha_1$  and  $\alpha_2$ . In this thesis, apart from TTHG and TTRM, the Cornette Shanks (CS) phase function<sup>86</sup> was also used:

$$f_{CS}(\theta, g) = \frac{3[1 + \cos(\theta)]^2}{2(2 + g^2)} \frac{1 - g^2}{[1 + g^2 - 2g \cos(\theta)]^{\frac{3}{2}}} \quad (2.47)$$

The CS phase function, has only one variable, the asymmetry factor  $g$ . When  $g$  is close to 0 it converges to the Rayleigh phase function and when  $g$  is close to 1 it approaches the HG phase function. Therefore, it provides a realistic description of the scattering by small particles. The deficiency of the CS phase function is that it fails to reproduce the sharp forward/backward scattering peak. The Forand-Fournier phase function (FF) was first derived for scatterers in oceanic water, and considers the particle size distribution and mean index of refraction of the scattering particles<sup>88</sup>:

$$f_{FF}(u, v, \delta) = \frac{1}{4\pi} \frac{1}{(1 - \delta)^2 \delta^v} \left\{ [v(1 - \delta) - (1 - \delta^v)] + \frac{4}{u^2} [\delta(1 - \delta^v) - v(1 - \delta)] \right\} \quad (2.48)$$

where  $v = (3 - \mu)/2$ ,  $\delta = u^2/3(n-1)^2$ , and  $u = 2\sin(\theta/2)$ .

These empirical phase functions represent the scattering distribution of the cloud of nanoparticles as a whole. In the case when nanoparticles are encapsulated in plane layers, the light impinging on the nanoparticles propagates into different directions inside the nanocomposite layer because of previous scattering events. In order to characterize the radiation field inside the sample, the angular distribution of scattered light from the sample needs to be investigated. What we measured is the outer scattering distribution. The inner scattering distribution need to be calculated. The Snell's law of refraction<sup>89</sup> solves the problem of a ray travelling from one optical medium to another optical medium with different refractive indices,

$$n_1 \cdot \sin(\beta_1) = n_2 \cdot \sin(\beta_2) \quad (2.49)$$

where  $\beta_1$  is the incident light angle and  $\beta_2$  is the refracted light angle,  $n_1$  and  $n_2$  are the complex refractive index of the medium with incident light and refracted light (Figure 2.7).

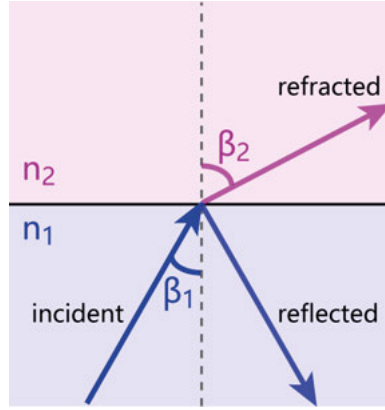


Figure 2.7. Schematic of incident, reflected and refracted light in between two mediums with different refractive indices.

The Fresnel reflection law<sup>89</sup> states the Fresnel reflection coefficients for the s-polarized and p-polarized light

$$r_s = \frac{n_1 \cdot \cos(\beta_1) - n_2 \cdot \cos(\beta_2)}{n_1 \cdot \cos(\beta_1) + n_2 \cdot \cos(\beta_2)} \quad (2.50)$$

$$r_p = \frac{n_2 \cdot \cos(\beta_1) - n_1 \cdot \cos(\beta_2)}{n_2 \cdot \cos(\beta_1) + n_1 \cdot \cos(\beta_2)} \quad (2.51)$$

where  $\beta_1$  is the angle of incident light and  $\beta_2$  is the angle of the refracted light, the reflection coefficients are

$$R_s = |r_s|^2 \quad (2.52)$$

$$R_p = |r_p|^2 \quad (2.53)$$

If we take into account Snell's law to replace  $\beta_2$  with  $\beta_1$

$$R_s = \left| \frac{n_1 \cdot \cos(\beta_1) - n_2 \cdot \sqrt{1 - \left[\frac{n_1}{n_2} \sin(\beta_1)\right]^2}}{n_1 \cdot \cos(\beta_1) + n_2 \cdot \sqrt{1 - \left[\frac{n_1}{n_2} \sin(\beta_1)\right]^2}} \right|^2 \quad (2.54)$$

$$R_p = \left| \frac{n_1 \cdot \sqrt{1 - \left[\frac{n_1}{n_2} \sin(\beta_1)\right]^2} - n_2 \cdot \cos(\beta_1)}{n_1 \cdot \sqrt{1 - \left[\frac{n_1}{n_2} \sin(\beta_1)\right]^2} + n_2 \cdot \cos(\beta_1)} \right|^2 \quad (2.55)$$

since unpolarized natural light contains the same amount of s- and p- polarized light,

$$R = R_s + R_p \quad (2.56)$$

Figure 2.8 shows the reflectance coefficients  $R_{s,p}$  and reflectance  $R$  when the light is shining from glass ( $n = 1.5$ ) to air ( $n = 1$ ). The angle when  $R_p$  equals to 0 is called Brewster's angle. The angle when  $R$  reaches unity (total reflectance) is called the critical angle ( $\theta_c$ ).  $\theta_c$  can be obtained by Snell's law:

$$\theta_c = \sin^{-1}\left(\frac{n_2}{n_1}\right) \quad (2.57)$$

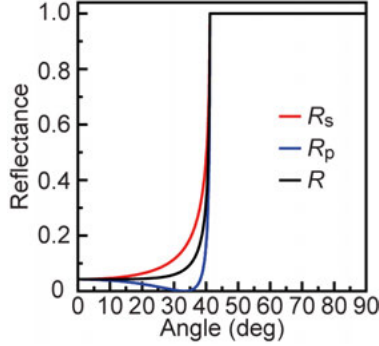


Figure 2.8.  $s$ -,  $p$ - polarized reflectances ( $R_{s,p}$ ) and unpolarized reflectance ( $R$ ) calculated by Fresnel's reflection law when light is shining from glass to air.

With knowledge from Snell's law and Fresnel's law, we can convert the outer measured scattering intensity into the scattering distribution inside the film. Equations 2.58 and 2.59 give the angle correction, from the outer measured angle  $\theta_o$  to the angle inside the scattering layer  $\theta_i$ , and finally the outer measured  $ARS(\theta_o)$  into the inner  $BSDF(\theta_o)$ .

$$\theta_i = \arcsin\left(\frac{\sin(\theta_o)}{\frac{n_i}{n_o}}\right) \quad (2.58)$$

$$f(\theta_i) = \frac{ARS(\theta_i)}{[1 - r(\theta_i)]\cos(\theta_i)} \quad (2.59)$$

### 3. Material Synthesis and Characterization

#### 3.1 Synthesis of nanoparticles and composite layers

Three types of nanoparticles, metallic Au, ferromagnetic  $\text{Fe}_3\text{O}_4$  and photocatalytic  $\text{TiO}_2$  were synthesized using a bottom-up wet chemistry method, which allows good control of the shape and size of nanostructures.

Au nanospheres with a diameter of around 200 nm were provided by Nanoseedz<sup>TM</sup>. The synthesis of the Au sample took advantage of seed-mediated growth together with mild oxidation, starting from small Au NSs, growing to nanopolyhedra, and reshaping to Au NSs with different diameters by etching the edges of the nanopolyhedra by oxidation using  $\text{HAuCl}_4$ <sup>90</sup>.

$\text{Fe}_3\text{O}_4$  nanospheres with diameters of 89 nm, 207 nm and 458 nm were prepared (denoted as NS89, NS207, NS458).

In a typical synthesis of  $\text{Fe}_3\text{O}_4$  NS89,  $\text{FeCl}_3 \cdot 6\text{H}_2\text{O}$  (0.05 g) and sodium acetate trihydrate ( $\text{NaAc} \cdot 3\text{H}_2\text{O}$ , 0.15 g) were dissolved in 20 mL of ethylene glycol during stirring and ultrasonic treatment. The homogeneous yellow mixture was then transferred to a 50 mL Teflon-lined stainless-steel autoclave which was sealed and heated to 200°C for 4 h. After reaction, the magnetic nanoparticles were collected by a magnet and suspended in 20 mL of ethylene glycol containing  $\text{FeCl}_3 \cdot 6\text{H}_2\text{O}$  (0.1 g), polyvinylpyrrolidone (PVP, MW: 40000, 4 g), sodium acetate trihydrate ( $\text{NaAc} \cdot 3\text{H}_2\text{O}$ , 0.3 g) and 1 mL of polyethylene glycol (PEG, MW: 300) during stirring and ultrasonic treatment. The mixture was again transferred to the autoclave which was sealed and heated to 200°C for 4 h. In order to obtain the  $\text{Fe}_3\text{O}_4$  NS89, the as-prepared solution was centrifuged at 1700 rpm for 1 min.  $\text{Fe}_3\text{O}_4$  NSs were collected from the supernatant by a magnet and washed with 50 mL distilled water. The centrifugation and washing processes were repeated 5 times. The  $\text{Fe}_3\text{O}_4$  NS89 was eventually obtained by drying overnight at 80°C.

In a typical synthesis of  $\text{Fe}_3\text{O}_4$  NS207,  $\text{FeCl}_3 \cdot 6\text{H}_2\text{O}$  (0.1 g), polyvinylpyrrolidone (PVP, MW: 40000, 4 g), sodium acetate trihydrate ( $\text{NaAc} \cdot 3\text{H}_2\text{O}$ , 0.3 g) and 1 mL of polyethylene glycol (PEG, MW: 300) were dissolved in ethylene glycol (20 mL) during stirring and ultrasonic treatment. The homogeneous yellow mixture was then transferred to a Teflon-lined stainless-steel autoclave which was sealed and heated to 200°C for 4 h. The  $\text{Fe}_3\text{O}_4$  NSs were formed and collected by a magnet, washed with distilled water (50 mL), and collected the precipitation by centrifugation at 1700 rpm for 20 min. The



washing and centrifugation processes were repeated 5 times. The Fe<sub>3</sub>O<sub>4</sub> NSs were eventually collected by drying overnight at 80°C.

In the synthesis of Fe<sub>3</sub>O<sub>4</sub> NS458, FeCl<sub>3</sub>·6H<sub>2</sub>O (0.8105 g), polyvinylpyrrolidone (PVP, MW: 40000, 2 g), and sodium acetate trihydrate (NaAc·3H<sub>2</sub>O, 1.225 g) were dissolved in 25 mL of ethylene glycol during stirring and ultrasonic treatment. The homogeneous yellow mixture was then transferred to a 50 mL Teflon-lined stainless-steel autoclave which was sealed and heated to 190°C for 12 h. The Fe<sub>3</sub>O<sub>4</sub> NSs were formed and collected the precipitation by centrifugation at 1600 rpm for 1 min, and washed with 10 mL distilled water. The washing and centrifugation processes were repeated 5 times. The Fe<sub>3</sub>O<sub>4</sub> NSs 500 were eventually collected by drying overnight at 80°C.

The TiO<sub>2</sub> NS200 were synthesized using a similar procedure previously described by Han<sup>91</sup> with minor modifications. Briefly, CaCl<sub>2</sub> solution (0.05 M, 200 µL) was added to methanol (50 mL) into a one-necked flask and stirred for 10 min. Titanium (IV) isopropoxide (850 µL) was added dropwise. The resulting solution was magnetically stirred for 24 h at room temperature. The synthesized TiO<sub>2</sub> NSs were subsequently washed with distilled water (50 mL) and collected by centrifugation at 1700 rpm for 20 min. The washing and centrifugation processes were repeated 5 times. The TiO<sub>2</sub> NSs were obtained by first ramping up to 450 °C at 5°C·min<sup>-1</sup> and keeping it for 2hr, and then cooling down to room temperature.

The Au, Fe<sub>3</sub>O<sub>4</sub> and TiO<sub>2</sub> NSs were homogeneously dispersed in water at a volume fraction of 0.1%, equivalent to a particle concentration of 2.39·10<sup>11</sup>·mL<sup>-1</sup>. Then PVP was added to the NS/water solution at a mass ratio of 0.8 (PVP/water). The volume fraction of nanospheres in the resultant water+PVP mixture was 0.066%. PVP has high viscosity and good binding capability to water. It dissolves at room temperature and is highly stable and nontoxic. The NS/water/PVP solution was vigorously shaken in a vortex mixer until the PVP powders dissolved completely. The viscous solution was deposited on a glass slide, and another glass side with a spacer ~80 µm in thickness was added on top. The as-made particle-incorporated sample was sealed with glue and measurements of their optical spectra took place after 20 days to ensure the sample was stable.

### 3.2 Optical microscopy (OM)

The optical microscope comprises a light source, lenses, eyepieces (oculars) and a camera. Light is an incandescent source. The overall magnification is given by the magnification of the objective times, the magnification by the eyepiece (Figure 3.1). The maximum resolution

$$R = \frac{0.61 \cdot \lambda}{N.A.} = \frac{0.61 \cdot \lambda}{n \sin(\alpha)} \quad (3.1)$$

where 0.61 is a geometrical term,  $\lambda$  is the wavelength of incident light,  $N.A.$  is the numerical aperture,  $n$  is the refractive index of the medium (for example, air,  $n=1$ , oil,  $n=1.515$ ),  $\alpha$  is the maximal half-angle of the cone of light that can enter or exit the lens. Therefore, the resolution improves (smaller  $R$ ) with a smaller  $\lambda$ , and larger  $n$  and  $\alpha$ .



Figure 3.1. Optical components of an optical microscope.

An Olympus BX60 optical microscope, a dark-field objective (10x, numerical aperture = 0.9), together with a camera were used to record the images of the nanoparticle composites. The resolution of our sample is in the range of 260 nm to 530 nm if wavelength  $\lambda$  is in the visible range from 380 nm to 780 nm.

### 3.3 Scanning electron spectroscopy (SEM)

Surface morphology can be studied by Scanning Electron Microscopy. When a focused electron beam scans the surface, several types of signals are produced and detected as a function of position on the surface, *i.e.*, secondary electrons, backscattered electrons, X-ray and Auger electrons. Secondary electrons give information of surface structure, backscattered electrons give information of surface structure and elemental information. X-rays and Auger electrons give the elemental composition with different thickness-sensitivity. The secondary electrons are attracted by a positively biased detector and translated into a signal. SEM has a large depth of field, 4 mm-0.4 mm, which allows it to see large amounts of the sample at one time. The magnification can go beyond 300,000x.

In our work, SEM imagings were performed on a Zeiss (LEO) 1530 FEG microscope at an acceleration voltage of 5 keV to examine the microstructure of synthesized nanoparticles.

### 3.4 Dynamic light scattering (DLS)

Dynamic light scattering is a technique that can be used to determine the size distribution profile of small particles in suspension or polymers in solution. The sample is illuminated by a laser beam and the fluctuations of the scattered light are detected at a known scattering angle  $\theta$  by a fast photon detector<sup>92-93</sup>. The diameter measured by DLS is a value that refers to how a particle moves within a liquid, called the hydrodynamic diameter. This is the diameter of a sphere that has the same translational diffusion coefficient as the particle.

The size of the particles can be determined from measurements of Brownian motion. Brownian motion is random movement of particles due to the bombardment by the solvent molecules that surround them. The variation of intensity with time contains information on the random motion of the particles. A larger particle will have a slower Brownian motion. Brownian motion also relates to the temperature, the higher the temperature the more rapid the Brownian motion will be. An accurate temperature needs to be known, as the viscosity of the solution is dependent on temperature. The relative error in the measured size is equal to the relative error in the solvent viscosity, *e.g.*, 5% error in viscosity will have 5% error in size. The hydrodynamic diameter  $d(H)$  of the particle is given by:

$$d(H) = \frac{kT}{3\pi\eta D} \quad (3.2)$$

where  $k$  is Boltzmann's constant,  $T$  is the absolute temperature,  $\eta$  is the viscosity and  $D$  is the diffusion coefficient, which is related to scattering vector  $q$  and relaxation time  $\tau$ .<sup>92-93</sup>

The polydispersity index (PDI) denotes the variation of the particle size distribution, defined by the square of the ratio of the standard deviation and the mean. A PDI of 0 to 0.08 means monodisperse particles, 0.08 to 0.7 is a mid-range polydispersity, and greater than 0.7 means very disperse. If PDI is larger than 0.7, care should be taken to interpret the data as the sample may not be suitable for this technique.

In our work, all the samples measured by DLS were first dispersed in water by ultrasound and the hydrodynamic diameter was determined by a Zetasizer Nano ZSP. The detection is made at a scattering angle of  $7^\circ$  compared to the incident light direction. The concentration of nanospheres in water was kept at  $20 \mu\text{g}\cdot\text{mL}^{-1}$ .

### 3.5 X-ray diffraction (XRD)

X-rays can be used to study the crystal structure, since in crystals the typical interatomic spacing is about  $2\text{-}3\text{\AA}$ . For different target metal, the wavelength from the inner shell  $K_\alpha$  is different. For example,  $K_\alpha$  for Mo is  $0.71\text{\AA}$ , Cu is  $1.54\text{\AA}$ , Co is  $1.79\text{\AA}$ , Fe is  $1.94\text{\AA}$ , Cr is  $2.29\text{\AA}$ . A beam of X-ray interacts

with the atom in the crystal. The electrons in the atom vibrate at the same frequency as the incoming X-rays. Because of the periodic structure of the crystal, the emitted radiation shows constructive or destructive interference. Bragg's equation explains the path difference between the parallel rays is dependent on the incident light wavelength. For constructive interference we have (Figure 3.2):

$$n\lambda = 2d_{hkl} \sin(\theta) \quad (3.3)$$

where  $n$  is an integer and represents the order of reflection.  $d_{hkl}$  is the space between the planes (for cubic system):

$$d_{hkl} = \frac{a}{\sqrt{h^2 + k^2 + l^2}} \quad (3.4)$$

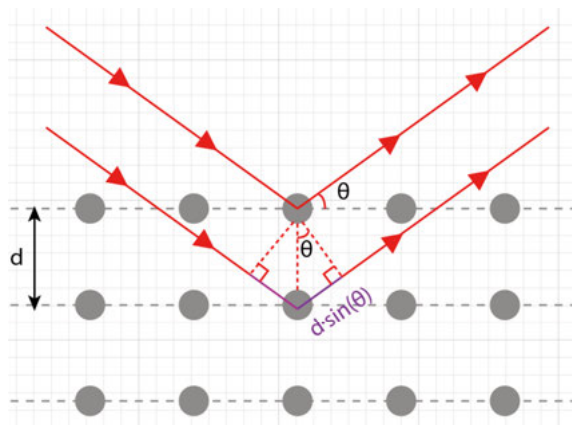


Figure 3.2. Construction for the derivation of the Bragg condition for constructive interference. The horizontal lines represent the lattice planes that are separated by a distance  $d$ . The oblique lines represent X-rays incident at an angle  $\theta$  against to the lattice plane.

The space between diffracting planes of atoms determines peak positions. Diffraction occurs when each object in a periodic array scatters radiation coherently, producing constructive interference at specific angles. Diffraction from different planes of atoms produces a diffraction pattern, which contains information about the atomic arrangement within the crystal.

In our work, the XRD patterns were measured by a SIEMENS D5000 diffractometer with Cu K $\alpha$  ( $\lambda = 1.54\text{\AA}$ ) radiation at a scanning speed of  $0.1^\circ\cdot\text{s}^{-1}$  from  $5^\circ$  till  $85^\circ$  at an interval of  $0.05^\circ$  in two-theta geometry.

## 4. Optical Characterization

### 4.1 Spectrophotometry

The transmittance and reflectance were recorded using a commercial Perkin-Elmer Lambda 900 spectrometer equipped with a 150 mm diameter Spectralon-coated integrating sphere. In the transmittance mode, the sample is placed normal to the incident light. In the reflectance mode, the angle between the incident light to the surface normal is  $8^\circ$ . A photomultiplier was used in the UV/VIS range and a lead sulfide (PbS) detector was used in the NIR range. The detector change occurred at 900 nm. The light source was a tungsten lamp. The scan speed was  $250 \text{ nm} \cdot \text{min}^{-1}$ , using a slit width of 3 nm in VIS and 2 nm in NIR region.

Total, diffuse, and regular/specular transmittance ( $T_{\text{tot}}$ ,  $T_{\text{dif}}$ ,  $T_{\text{reg}}$ ) and reflectance ( $R_{\text{tot}}$ ,  $R_{\text{dif}}$ ,  $R_{\text{spe}}$ ) can be obtained by measuring total and diffuse transmittance signals ( $S_{\text{tot}}$ ,  $S_{\text{dif}}$ ) and reflectance signals ( $U_{\text{tot}}$ ,  $U_{\text{dif}}$ ). The geometry of the integrating sphere is shown in Figure 4.1. In both transmittance and reflectance measurements, a spectralon reference with known reflectance  $R_{\text{refer}}$  was first placed at position 2 to record the background signal without a sample. In the transmittance mode, the sample was put at position 1, and the spectralon reference was placed at position 2 to record  $S_{\text{tot}}$ . By replacing the spectralon reference with a black cone,  $S_{\text{dif}}$  was obtained.  $T_{\text{tot}}$ ,  $T_{\text{dif}}$ ,  $T_{\text{reg}}$  can be derived by

$$T_{\text{reg}} = S_{\text{tot}} - S_{\text{dif}} \quad (4.1)$$

$$T_{\text{dif}} = S_{\text{dif}} \cdot R_{\text{refer}} \quad (4.2)$$

$$T_{\text{tot}} = T_{\text{reg}} + T_{\text{dif}} \quad (4.3)$$

In the reflectance mode, the sample was placed at position 2 with a black beam trap behind the sample, and  $U_{\text{tot}}$  was obtained. Then the exit port at position 3 was opened to obtain  $U_{\text{dif}}$ .  $R_{\text{tot}}$ ,  $R_{\text{dif}}$ ,  $R_{\text{spe}}$  can be derived by

$$R_{\text{spe}} = (U_{\text{tot}} - U_{\text{dif}}) \cdot 0.96 \quad (4.4)$$

$$R_{\text{dif}} = U_{\text{dif}} \cdot R_{\text{refer}} \quad (4.5)$$

$$R_{\text{tot}} = R_{\text{spe}} + R_{\text{dif}} \quad (4.6)$$

A factor of 0.96 corrected for differences between the reflectance of the reference plate and the coating on the integrating sphere, as well as for geometrical factors. The port angle for the regular transmittance (position 1) was  $\pm 4.6^\circ$  and  $\pm 7.4^\circ$  for specular reflectance (position 3), as shown in Figure 4.1. Light

scattered at angles larger than these were attributed to diffuse transmittance and reflectance.

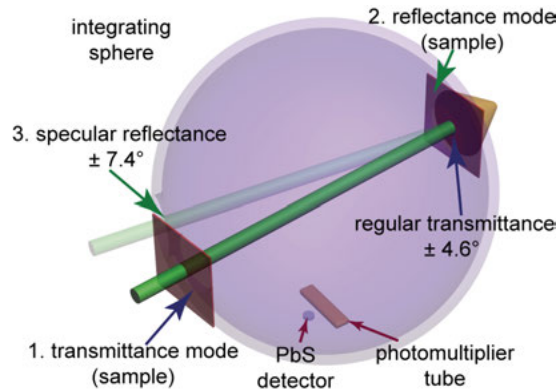


Figure 4.1. Schematic illustration of the integrating sphere used in the Lambda 900 spectrophotometer that shows the sample position in the transmittance and reflectance modes, and the regular transmittance/specular reflectance angle range from its geometry.

## 4.2 In-plane angle resolved scatterometer

The in-plane angle resolved scatterometer consists of a 250 W tungsten-halogen lamp with a stabilized dc power supply, a monochromator (SP-401), two gratings with blaze wavelength of 0.75  $\mu\text{m}$  and 2.0  $\mu\text{m}$ , a parabolic aluminum mirror with an off-axis distance of 80 mm and a focal length of 410 mm. A schematic illustration of the measurement light system together with the sample, is shown in Figure 4.2. The detector was a silicon diode with a spectral response region from 300 nm to 1100 nm, with a dimension of  $6.4 \times 6.4 \text{ mm}^2$ . Lock-in technique was used to monitor the signal from the detector (EG&G model 7260). The sample was centrally mounted and illuminated, and the silicon detector can be moved between  $0^\circ$  to  $180^\circ$ . In order to increase the dynamic range of the measurements, we applied different neutral density filters (Thorlabs) for measuring at different wavelengths. The filters were designed for 633 nm wavelength and mounted in a manual filter wheel. A 50% filter was used for the wavelength 350 nm (transmittance of 0.16258). A 1% filter was used for 400 nm (transmittance: 0.00266), 500 nm (transmittance: 0.00653), and 600 nm (transmittance: 0.00747). A 0.1% filter was used for 700 nm (transmittance: 0.00512), 800 nm (transmittance: 0.01159), 900 nm (transmittance: 0.01138), and 1000 nm (transmittance: 0.01012). The incident light spot was much smaller than the Si detector. The incident light intensity  $P_i$  was calculated using the measured intensity with the filter  $I_{\text{filter}}$ , divided by the filter transmittance at the specific wavelength.

The light spot spanned an angle within  $\pm 1^\circ$ . The transmittance and reflectance was measured as a function of angle at a fixed wavelength. An angle of  $10^\circ$  of the sample normal to the incident light was set in order to be able to measure the specular and near-specular reflected intensity. Subsequently the data was shifted by using Harvey's method<sup>94</sup> (refer to chapter 4.3). The measured radiant intensity was represented in the form of angle-resolved scattering (ARS), by normalizing with the incident light intensity  $P_i$  and solid angle  $\Omega$  of the detector:

$$ARS(\beta) = \frac{S(\beta)}{P_i \cdot \Omega} = \frac{S(\beta)}{\frac{S(0^\circ)}{T_{\text{filter}}} \cdot \frac{A}{R^2}} \quad (4.7)$$

where  $S(\beta)$  was the measured radiant intensity of the sample. In the small-angle region, i.e., lower than  $2^\circ$ , the measurements were conducted together with a filter and thereby the intensity was divided by the filter transmittance.  $S(0^\circ)$  was the measured intensity of the incident light with filter and without sample.  $T_{\text{filter}}$  is the transmittance of the filter at the desired wavelength,  $A$  is the surface area of the detector port,  $R$  is the distance from the sample to the detector, i.e., 20 cm. The solid angle  $\Omega$  was equal to  $6.4^2/200^2 = 0.00124024 \text{ sr}$ .

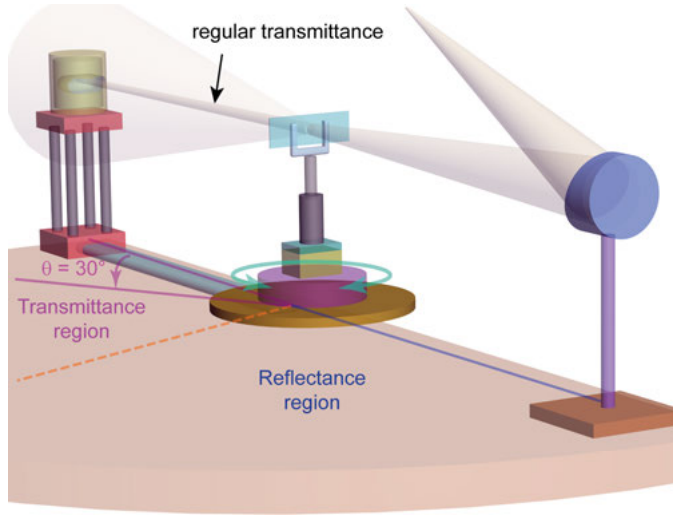


Figure 4.2. Schematic of the in-plane angle resolved scatterometer.

### 4.3 Angle correction by Harvey's method

Owing to the geometry of the in-plane angle resolved scatterometer, the direct reflectance from the sample at normal incidence is not available since the detector blocks the incident light. In order to get the reflectance information as

a function of angle at small angles, we need to rotate the sample so that the detector can record specular reflectance without blocking the incident light. Harvey<sup>94</sup> measured scattering from various reflecting surfaces with different scattering angles. The curves were extremely asymmetrical, but when the scattering intensity was represented by a correction of x-axis by  $\chi$ ,

$$\chi = \frac{\sin(\beta) - \sin(\beta_0)}{1 - \sin(\beta_0)} \quad (4.8)$$

the curves overlapped. The scattering from our sample mainly contributed from bulk scattering, instead of surface scattering, which was considered by Harvey<sup>94</sup>. We examined the angle resolved scattering from the TiO<sub>2</sub> sample when the sample was tilted at different angles (Figure 4.3a). The incident light was fixed at 600 nm. The value of the tilted angle was the same as the angle of specular reflection  $\beta_0$  since the scattering angle refers to the sample normal.

In Figure 4.3a, the sample was tilted from 0° to 70°. When the tilting angle is 0°, the specular reflection should also be 0°. However, we were not able to measure it due to the geometry of the system. The measurement was started from scattering angle at 16° in order that the detector not blocking the incident light. The specular peak positions were the same as the tilting angles. The curves are highly asymmetrical and the intensity of the peaks might come from the polarization of the light source at different angles. We used Harvey's approach to convert our results, and found that the curves with tilting angles 0°, 10°, 20° almost overlap (Figure 4.3b). The curves with higher tilting angles (higher than 30°) can not reproduce the curves in Figure 4.3b after the correction (Figure 4.3c). In our experiment for reflectance measurements on the in-plane scatterometer, the sample was tilted by 10° so that it was comparable to the Lambda 900 spectrophotometer where the specular reflectance is 8° from sample's normal. Therefore, we can correct the scattering angle  $\beta_{corrected}$  and get angular reflectance from 0° to 90° by using Harvey's method (Figure 4.3b,c) according to

$$\beta_{corrected} = \arcsin\left[\frac{\sin(\beta) - \sin(\beta_0)}{1 - \sin(\beta_0)}\right] \quad (4.9)$$



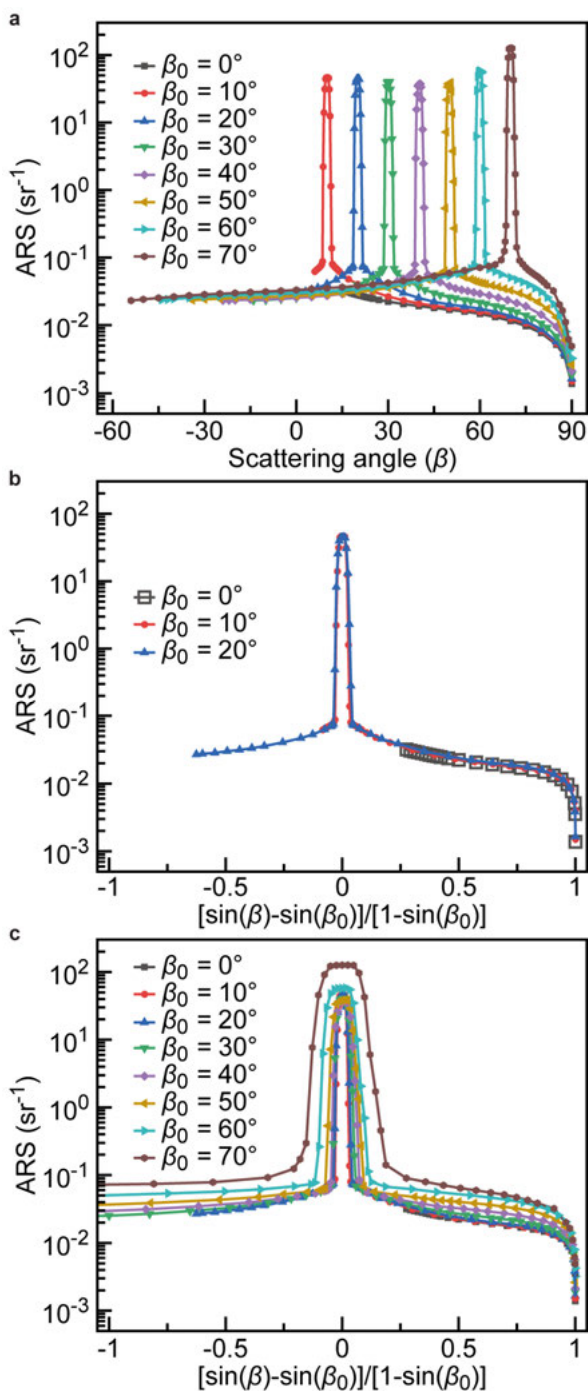


Figure 4.3. (a) Scattered intensity versus scattering angle when the sample was tilted at different angles from  $0^\circ$  to  $70^\circ$ . (b,c) Harvey's method to convert ARS results from (a) by modifying the x-axis when the sample was tilted by an angle of (b)  $0^\circ$  to  $20^\circ$ , and (c)  $0^\circ$  to  $70^\circ$ .

## 4.4 Out-of-plane goniometer

The ‘out-of-plane’ spatial scattering intensity distribution was measured using a home-built goniometer (Figure 4.4). The light source was a red HeNe laser (wavelength  $\lambda = 633$  nm). The position-controlled detector was mounted on a movable arm, thereby allowing the detector to move in a hemisphere. The radius of the semicircular arc was 45 cm. The sample was fixed at the center of the arc, and was free to rotate around a horizontal axis, in order to vary the angle of incidence. The sample holder, the detector, and the arc were controlled by stepping motors. Lock-in technique was used to monitor the signal from the detector (EG&G model 7260). The detector was a silicon diode with a spectral response region from 300 nm to 1100 nm with dimensions of  $2.5 \times 2.4$  mm<sup>2</sup>. The incident light intensity was measured using a neutral density filter with a transmittance of 0.0004821 at 633 nm. The shortest steps corresponded to an angle shift of  $0.0015^\circ$ . In transmittance mode, the incident light was parallel to the normal of the sample surface. In the reflectance mode, the incident light was incident at  $10^\circ$  to the sample normal, the same as in the in-plane scattering measurement. The position of the sample to the incident light was fixed, and we measured a half hemisphere both in transmittance and reflectance regions and mirrored their intensity distributions to the other half hemisphere. The data analysis was similar to the in-plane spectrometer, the intensity was divided by the incident light intensity  $P_i$  and the solid angle  $\Omega$  of the detector port. The arm moved from  $-90^\circ$  to  $90^\circ$  while the detector moved in the range from  $-68^\circ$  to  $68^\circ$  on the arm due to the geometry of the instrument.

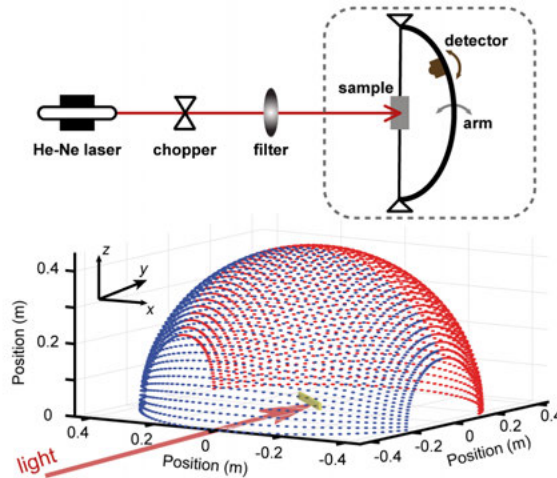


Figure 4.4. Schematic of the out-of-plane goniometer. The goniometer (upper) measures the intensity as the arm moves and the detector moves on the arm. It records the scattering in the forward (red) and backward (blue) half hemisphere (bottom).

## 4.5 Single-particle scattering system

The single-particle dark-field scattering spectra were recorded using an Olympus BX60 optical microscope integrated with a monochromator (Acton SpectraPro 2360i), a quartz-tungsten-halogen lamp (100 W), and a charge-coupled device camera (Princeton Instruments Pixis 400).<sup>90, 95-97</sup> The camera was thermoelectrically cooled to  $-70^{\circ}\text{C}$  during the measurements.

The nanoparticles were sparsely deposited on transparent ITO substrates. In the measurement of backward scattering, a dark-field objective (100x, numerical aperture = 0.9) was used to excite the nanoparticles with white light at an incidence angle of  $64^{\circ}$  in a circular ring, and then collecting the excited light within the angle range from  $0^{\circ}$  to  $60^{\circ}$  (Figure 4.5a). In the forward scattering measurement, the excitation light was introduced with a dark-field condenser below the sample at an incidence angle of  $68^{\circ}$  in a circular ring. The scattered light was collected above the sample using the same objective (Figure 4.5b). The exposure time for recording the spectra was from 20 seconds to 50 seconds, depending on the samples. The collected scattering spectra of the nanoparticles were corrected by subtracting the background spectra taken from the adjacent regions without particles, and then dividing by with the calibrated, normalized response curve of the entire optical system.

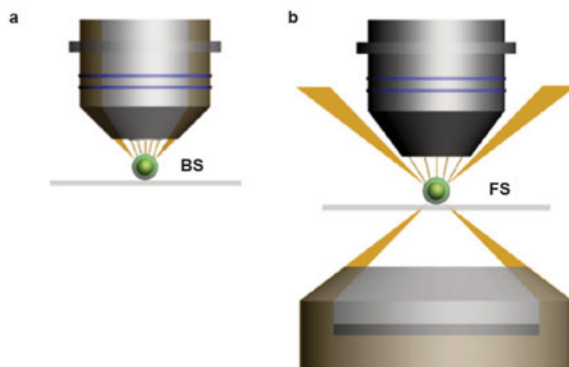


Figure 4.5. Schematics of the setups for the backward (a) and forward (b) scattering measurements. (adapted from reference <sup>97</sup>)

## 5. Results

### 5.1 Structure and morphology characterization

The Au,  $\text{Fe}_3\text{O}_4$  and  $\text{TiO}_2$  nanoparticles were synthesized by bottom-up wet chemistry approaches. The SEM images show similar diameters around 200 nm. Au nanospheres have a smoother surface compared to the metal oxide samples (Figure 5.1). The average diameter distributions are obtained from the SEM images shown in Figure 5.2, showing a narrower size distribution of Au nanospheres.

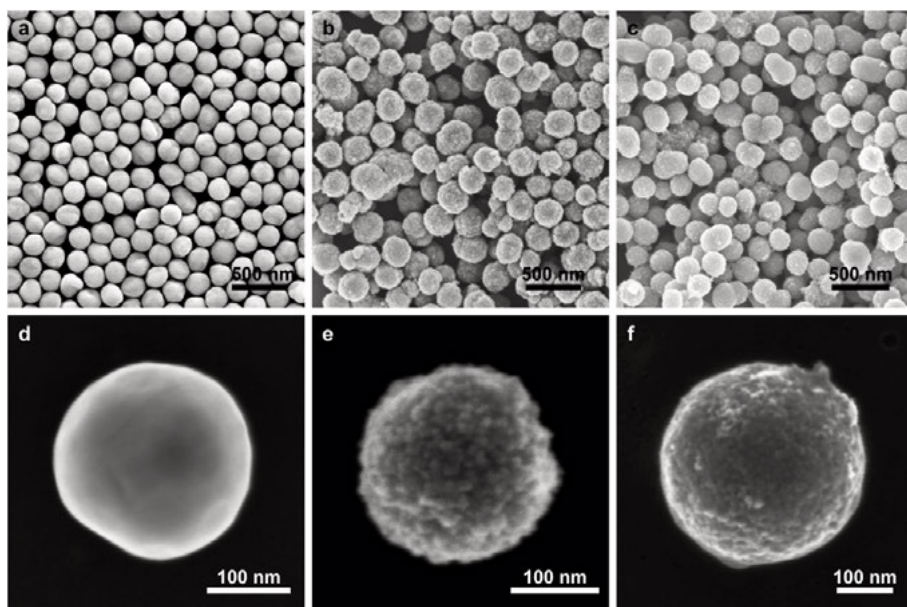


Figure 5.1. Scanning electron microscope images of the morphology of the (a) Au, (b)  $\text{Fe}_3\text{O}_4$  and (c)  $\text{TiO}_2$  nanospheres and zoom-in images of their single particles for (d) Au, (e)  $\text{Fe}_3\text{O}_4$  and (f)  $\text{TiO}_2$  samples.

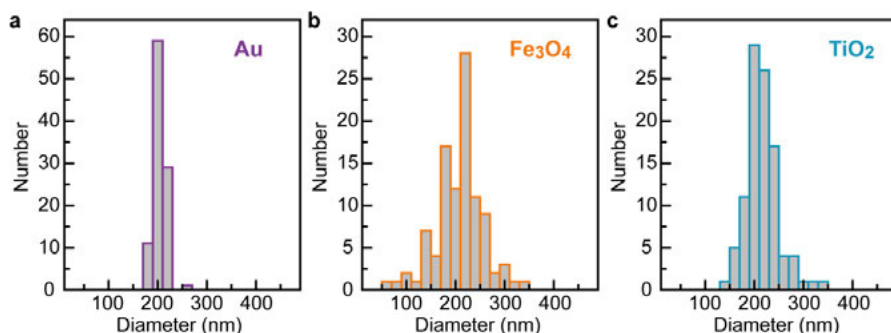


Figure 5.2. Histograms of the diameter distributions show that the average sizes with standard deviations were  $203 \pm 13$  nm,  $207 \pm 48$  nm and  $216 \pm 34$  nm for Au,  $\text{Fe}_3\text{O}_4$  and  $\text{TiO}_2$  spheres, respectively.

The XRD patterns show Au,  $\text{Fe}_3\text{O}_4$  and  $\text{TiO}_2$  samples are highly crystalline with the corresponding Joint Committee on Powder Diffraction Standards (JCPDS) cards (Figure 5.3).

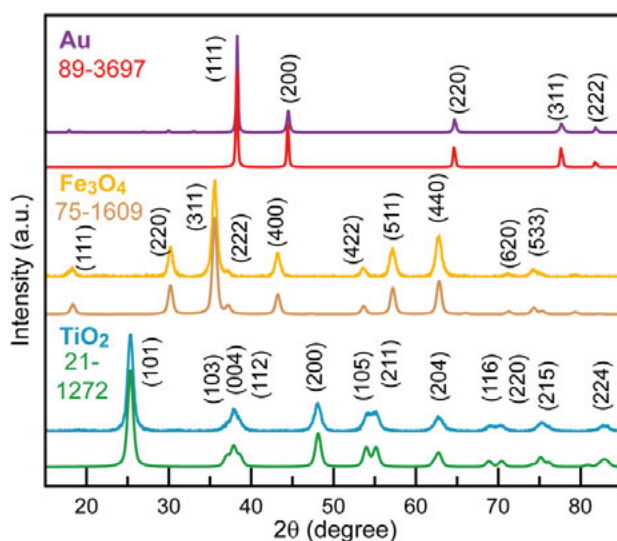


Figure 5.3. X-ray powder diffraction patterns of the three samples. Experimental XRD patterns (Au: purple,  $\text{Fe}_3\text{O}_4$ : yellow,  $\text{TiO}_2$ : blue) and corresponding JCPDS references, JCPDS # 89-3697 of the cubic phase of Au (red), JCPDS # 75-1609 of the orthorhombic phase of  $\text{Fe}_3\text{O}_4$  (dark yellow) and JCPDS # 21-1272 of the tetragonal phase of anatase  $\text{TiO}_2$  (green).

The dynamic light scattering results (refer to chapter 3) showed the hydrodynamic diameter of the three types of nanospheres in water (Figure 5.4). Au and  $\text{Fe}_3\text{O}_4$  nanospheres are well-dispersed in water; however, a lower degree

of dispersion was obtained for the TiO<sub>2</sub> nanospheres due to their high surface energy making them tend to aggregate.<sup>98</sup>

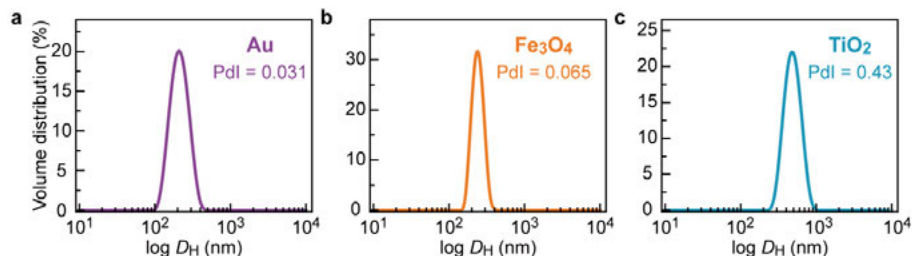


Figure 5.4. Hydrodynamic diameter distributions of the three samples in water. Dynamic light scattering profiles showing volume distributions of hydrodynamic diameter  $D_H$  at a concentration of  $20 \mu\text{g}\cdot\text{mL}^{-1}$  of a) Au  $204 \pm 56 \text{ nm}$  (polydispersity index (Pdl), 0.031), b) Fe<sub>3</sub>O<sub>4</sub>  $240 \pm 36 \text{ nm}$  (Pdl, 0.065), and c) TiO<sub>2</sub>  $652 \pm 116 \text{ nm}$  (Pdl, 0.43), respectively.

Three types of nanospheres were dispersed in water and PVP, and encapsulated into glass slides with a gap of around  $80 \mu\text{m}$  (chapter 3). The volume fraction of nanospheres in the resultant water+PVP mixture was 0.066%. The microscopic images of the three samples are shown in Figure 5.5, where samples are in stable state. It is observed that aggregation occurs for the samples.



Figure 5.5. Microscopic image (50 x) showing the dispersion of (a) Au, (b) Fe<sub>3</sub>O<sub>4</sub> and (c) TiO<sub>2</sub> nanospheres in the PVP matrix.

## 5.2 Measured transmittance and reflectance spectra

The reason for using PVP for sample preparation is that the refractive index of PVP is close to that of glass ( $\sim 1.5$  in the visible region), therefore, the reflection from the glass/(water+PVP) interface is negligible. The transmittance and reflectance of a glass/(water+PVP)/glass sample without adding the nanoparticles is close to that of a single glass slide (Figure 5.6), as measured in an integrating sphere. For example, at 600 nm,  $T_{\text{tot}}$  of glass (0.917), glass/(water+PVP)/glass (0.913), glass/(water)/glass (0.908),  $R_{\text{tot}}$  of glass (0.0804), glass/(water+PVP)/glass (0.0817), glass/(water)/glass (0.0870). The transmittance and reflectance of glass/(water+PVP)/glass is very close to that of glass,

the higher transmittance and lower reflectance compared to the glass/(water)/glass sample can be attributed to the refractive index of PVP being close to that of glass. Therefore, the interface between the scattering layer and glass can be ignored. The intermediate water and (water+PVP) layers were around 80  $\mu\text{m}$  in thickness.

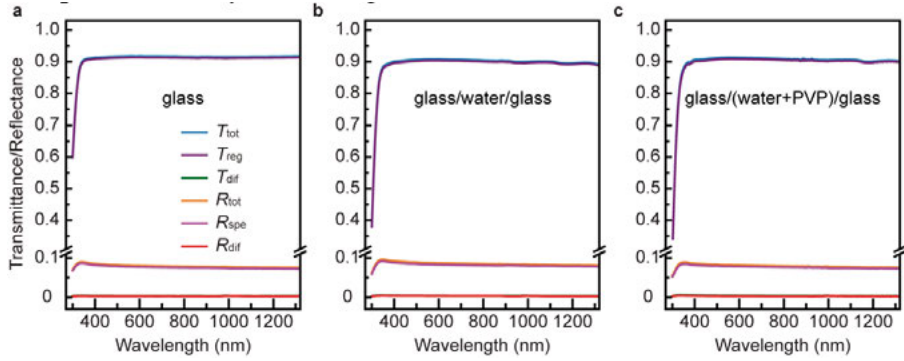


Figure 5.6. Total, diffuse, and regular/specular transmittance and reflectance spectra of a) a single glass, b) glass/water/glass, c) glass/(water+80wt% PVP)/glass.  $T_{\text{dif}}$  and  $R_{\text{dif}}$  of the three samples are close to zero, which indicates that no scattering occurs. Therefore,  $T_{\text{tot}}$  and  $R_{\text{tot}}$  overlap with  $T_{\text{reg}}$  and  $R_{\text{spe}}$ , respectively in (a-c).

Due to the similarity between the refractive index of the glass and the PVP, we can simply treat our sample as a slab where the nanoparticles are dispersed homogeneously. The absorption coefficient of the glass/(water+PVP)/glass sample (Figure 5.7) shows that the matrix is optically transparent and only absorbs light below 350 nm.

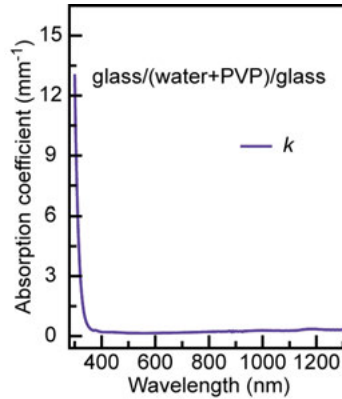


Figure 5.7. Absorption coefficient  $k$  of the glass/(water+PVP)/glass sample calculated from its  $T_{\text{reg}}$  and  $R_{\text{spe}}$  spectra use equations 2.28 and 2.29 ( $k$  is approximately equal to the extinction coefficient  $\epsilon$  when scattering can be ignored).



Total, regular/specular and diffuse transmittance and reflectance of the composite nanoparticle samples were measured in the wavelength range 300–1300 nm using a Perkin Elmer Lambda 900 spectrophotometer equipped with an integrating sphere detector.

The transmittance and reflectance components were obtained from the spectrophotometric measurements after standard corrections for sphere geometry and reflectance standard, and the results are depicted in Figure 5.8. The specular reflectance is slightly above 4% for all samples and primarily originates from the direct reflectance of the front side of the glass. The minimum in the total and regular transmittance at a wavelength of 580 nm of the Au sample (Figure 5.8a) originates from the localized surface plasmon resonance, which is the collective oscillation of free electrons in metallic particles. When the Au nanospheres are much smaller than the wavelength of light, the surface plasmon peak is located where the real part of the dielectric function of the metal is equal to  $-2\varepsilon_m$ , where  $\varepsilon_m$  is the dielectric constant of the surrounding medium. The real part of the dielectric constant of the metal determines the surface plasmon resonance peak (520 nm for Au) while the imaginary part determines its width<sup>99</sup>. As the Au nanospheres become larger, the resonance frequency moves towards longer wavelengths and is determined by the size of the Au nanoparticles.

Magnetite,  $\text{Fe}_3\text{O}_4$ , is a conducting oxide with optical intraband absorption extending down to zero energy and no well-defined band gap<sup>100</sup>. The optical absorption spectrum has additional contributions from interband transitions from the filled O 2*p* band and from Fe 3*d* states to the Fe 4*s* band<sup>100</sup>. The absorption coefficient increases steeply above about 1.5 eV, which is in qualitative agreement with the drop in transmittance below a wavelength of 800 nm in Figure 5.8b.

Anatase  $\text{TiO}_2$  is an indirect semiconductor<sup>17</sup>, where the conduction band consists of Ti 3*d* orbitals and the valence band is formed by O 2*p* orbitals. The experimental bandgap is 3.39 eV for anatase films and 3.20 eV for bulk anatase<sup>101</sup>. In Figure 5.8c, a sharp drop of transmittance below 400 nm signifies an absorption edge of  $\text{TiO}_2$  at 2.95 eV. It should be noted that diffuse transmittance is always higher than diffuse reflectance in these three samples, indicating larger forward scattering than backward scattering fluxes.



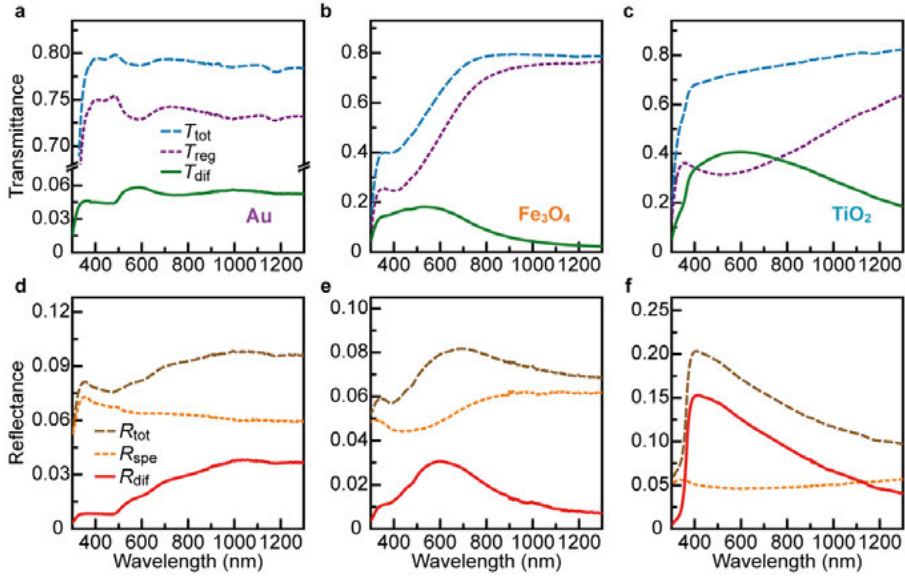


Figure 5.8. Transmittance and reflectance spectra of the Au, Fe<sub>3</sub>O<sub>4</sub> and TiO<sub>2</sub> nanoparticle samples from spectrophotometry. a-f) Total, diffuse and regular transmittance spectra (upper row) and total, diffuse, and specular reflectance spectra (lower row) of (a,d) Au, (b,e) Fe<sub>3</sub>O<sub>4</sub> and (c,f) TiO<sub>2</sub> nanoparticles dispersed in PVP+water. The thicknesses of the scattering layer of the Au, Fe<sub>3</sub>O<sub>4</sub> and TiO<sub>2</sub> samples were 81  $\mu$ m, 81  $\mu$ m, and 97  $\mu$ m, respectively.

### 5.3 Three dimensional out-of-plane light scattering of nanoparticle composite layers

We measured scattering intensity distributions from the samples by using a He-Ne laser with a wavelength of 633 nm. A three-dimensional goniometer was used to record the scattered light intensity in the forward and backward half hemispheres (Figure 5.9, chapter 2). The scattering intensity is presented as angle-resolved scattering (ARS)<sup>102</sup>. Forward scattering (*FS*) represents the light intensity in the hemisphere in the direction that the light propagates, *i.e.* for polar angle in the  $[0^\circ, 90^\circ]$  range, while the backward scattering (*BS*) denotes the light intensity in the opposite hemisphere when the  $\theta$  range is  $[90^\circ, 180^\circ]$  (Figure 5.9b). The forward and backward measured scattering intensity in a half hemisphere for three nanoparticle samples can be plotted as a function of spatial detector position ( $x,y,z$ ) (Figure 5.9c,d).

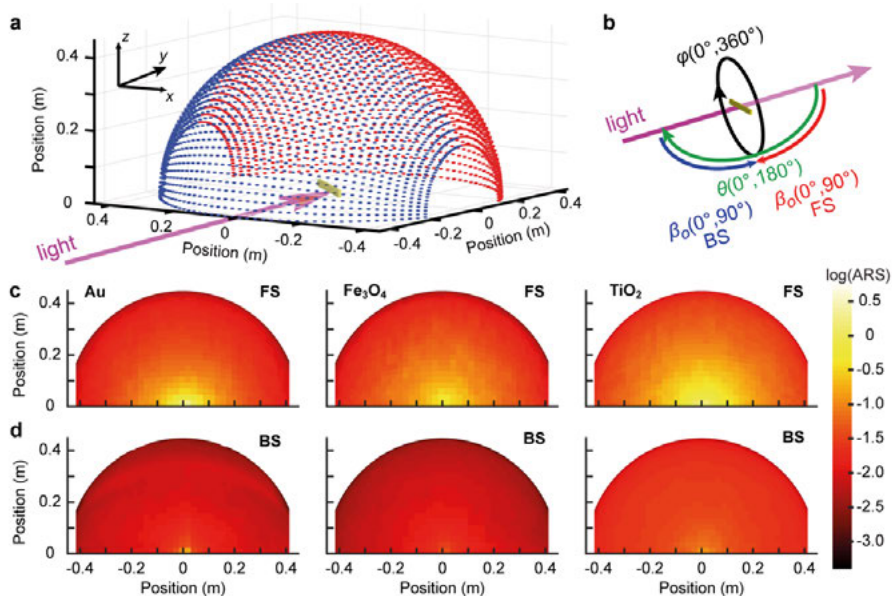


Figure 5.9. (a) The 3D goniometer records the scattering in the forward (red) and backward (blue) half hemisphere. (b) Sketch of the azimuthal angle  $\phi(0^\circ, 360^\circ)$ , polar angle  $\theta(0^\circ, 180^\circ)$  and scattering angle  $\beta_0(0^\circ, 90^\circ)$  in relation to the incident light and sample. Scattering angle  $\beta_0(0^\circ, 90^\circ)$  corresponds to  $\theta(0^\circ, 90^\circ)$  in the forward region and  $\theta(180^\circ, 90^\circ)$  in the backward region. Half hemisphere forward (c) and backward (d) scattering diagrams for Au,  $\text{Fe}_3\text{O}_4$  and  $\text{TiO}_2$  nanoparticles in PVP (logarithmic scale). The incident light is from a He–Ne laser with 633 nm wavelength.

By mirroring the intensity to the other half hemisphere, an extended scattering distribution can be plotted, as in Figure 5.10a-c for the forward and Figure 5.11a-c for the backward hemisphere. It is clearly observed that a strong peak appears in the direct forward and backward directions, and there is a large drop in intensity towards higher angles. There is an order of magnitude higher intensity in the forward peak compared to the backward peak for all three nanoparticle composites.

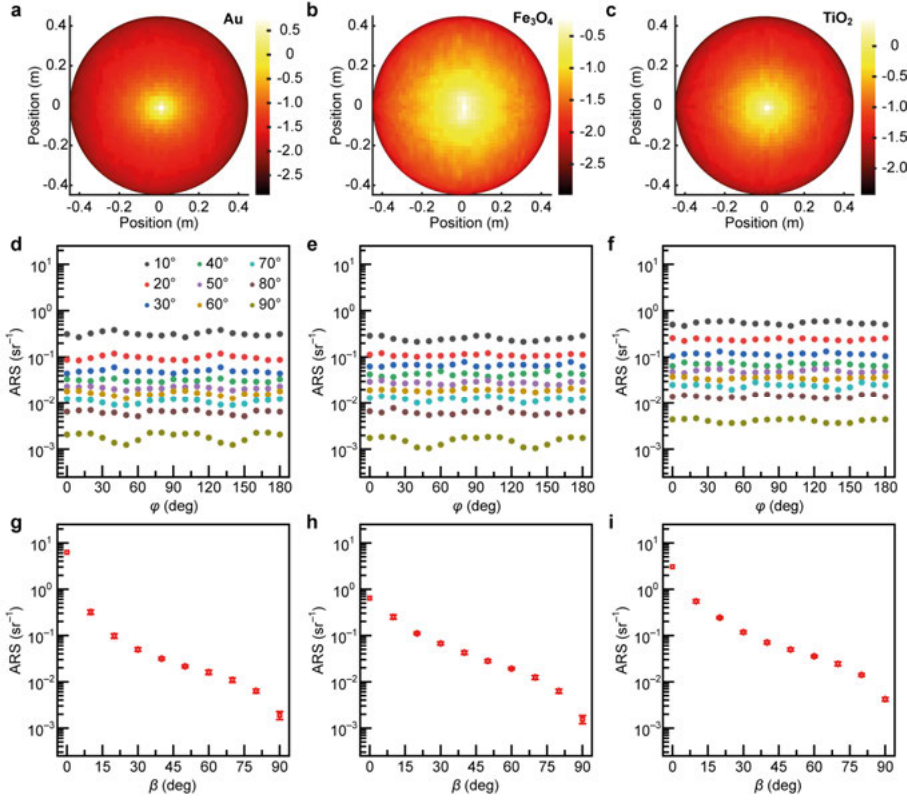


Figure 5.10. (a-c) Top view of the forward angle resolved scattering (ARS) for three nanoparticle scattering layers (in logarithmic scale). (d-f) Forward ARS as a function of azimuth angle taken at different scattering angles from 0° to 90° at an interval of 10°. (g-i) Forward ARS plotted as a function of the scattering angle.

We then plotted measured scattering data as a function of scattering angle ( $\beta$ ) and the azimuth angle ( $\varphi$ ). Figure 5.10d-f shows ARS of forward scattering at various scattering angles as a function of azimuth angle in logarithmic scale. Figure 5.10g-i gives the ARS of forward scattering as a function of the scattering angle. Figure 5.10d clearly shows that scattering is only dependent on the scattering angle, and insensitive to the azimuth angle. Figure 5.11d-i shows corresponding backward scattering data as a function of scattering/azimuth angle. Since the backward scattering is lower than the forward scattering, higher measurement fluctuations may occur. The data still show clear evidence of negligible dependence on the azimuth angle, indicating that scattering is only dependent on the scattering angle.

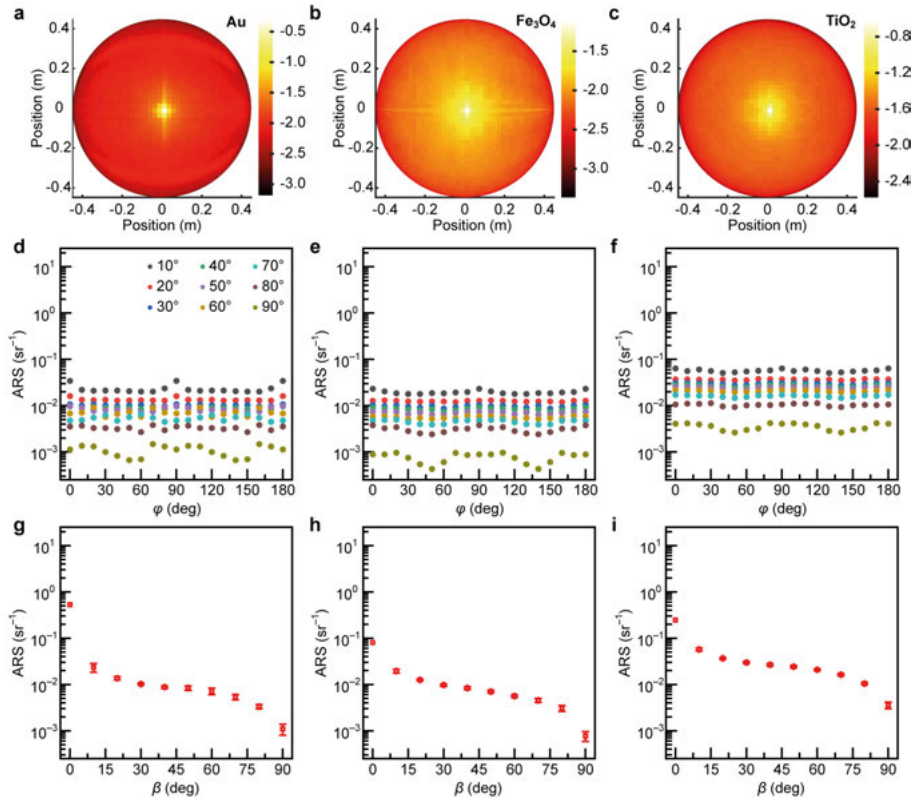


Figure 5.11. (a-c) Top view of the backward ARS for three nanoparticle scattering layers (in logarithmic scale). (d-f) Backward ARS as a function of the azimuth angle, taken at different scattering angles (inset) from 0° to 90°, at an interval of 10°. (g-i) Backward ARS plotted as a function of the scattering angle. The three columns give data for Au, Fe<sub>3</sub>O<sub>4</sub> and TiO<sub>2</sub> nanoparticle layers in PVP, respectively.

The accuracy and reproducibility of the out-of-plane goniometer are validated on measurements which took in different days on TiO<sub>2</sub> sample for forward (red) and backward (blue) directions (Figure 5.12), and indicating the good reproducibility of the instrument.

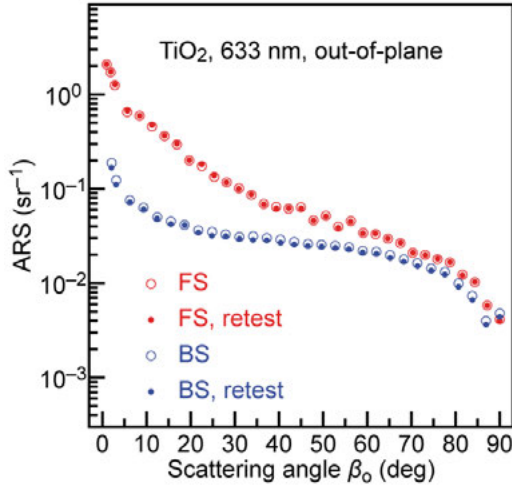


Figure 5.12. Forward and backward scattering intensity ( $\text{sr}^{-1}$ ), converted to angle-resolved scattering (ARS) by normalization of the incident light intensity and the solid angle of the detector, is shown as a function of the scattering angle measured on different days (open circle and solid dot) for a  $\text{TiO}_2$  sample ( $\lambda = 633 \text{ nm}$ ).

## 5.4 In-plane angle resolved results

From knowledge of out-of-plane light scattering measurements, the scattering is solely dependent on scattering angle. We therefore studied the in-plane angle dependent performance as a function of the scattering angle in different wavelength ranges. Figure 5.13 shows the angle-resolved scattering intensity measured from the in-plane angle resolved scatterometer on Au,  $\text{Fe}_3\text{O}_4$  and  $\text{TiO}_2$  nanosphere composites with average diameters of around 200 nm. The measurement covers the spectral range of incident light from 350 to 1000 nm, which contains the whole visible regimes and extends to a small portion of the UV and NIR regimes. The scattering angle  $\beta_0$  is recorded in the forward and backward directions from  $0^\circ$  to  $2^\circ$  (Figure 5.13a-c),  $2^\circ$  to  $90^\circ$  in forward (Figure 5.13d-f) and backward (Figure 5.13g-i) directions. In the small-angle region depicted in Figure 5.13a-c, the scattering intensity mainly consists by collimated incident light not absorbed or scattered by the nanoparticles. A minor portion comes from light scattered by the particle which is redirected into a small angle. This can be estimated by extrapolation from scattering profiles at angles larger than  $2^\circ$ . In the large-angle region, Figure 5.13d-i, the scattered intensity in the transmittance and reflectance regions drops rapidly for angles up to  $15^\circ$ , and is an order of magnitude higher in the transmittance region than the reflectance region. The scattering behavior is angle- and wavelength-dependent in a complex and sample-dependent manner. For the Au sample in the transmittance region, shorter wavelengths (less than 600 nm) have stronger scattering at lower angles (less than  $20^\circ$ ) while longer wavelengths have

stronger scattering at higher angles. For the  $\text{Fe}_3\text{O}_4$  sample, the intermediate wavelengths (600 nm) showed the strongest scattering in the transmittance and reflectance regions. The weak scattering for  $\text{TiO}_2$  at 350 nm in the transmittance and reflectance regions can be attributed to the bandgap absorption in that range.

The plots in Figure 5.13 can be converted to the scattering intensity as a function of wavelength at different scattering angles (Figure 5.14). The forward to backward ratios (Figure 5.14j-l) are lower (close to unity at  $80^\circ$ ) at high angles. Shorter wavelengths gave higher forward to backward ratios for the samples, apart from a minimum at around 400 nm for  $\text{TiO}_2$  sample.

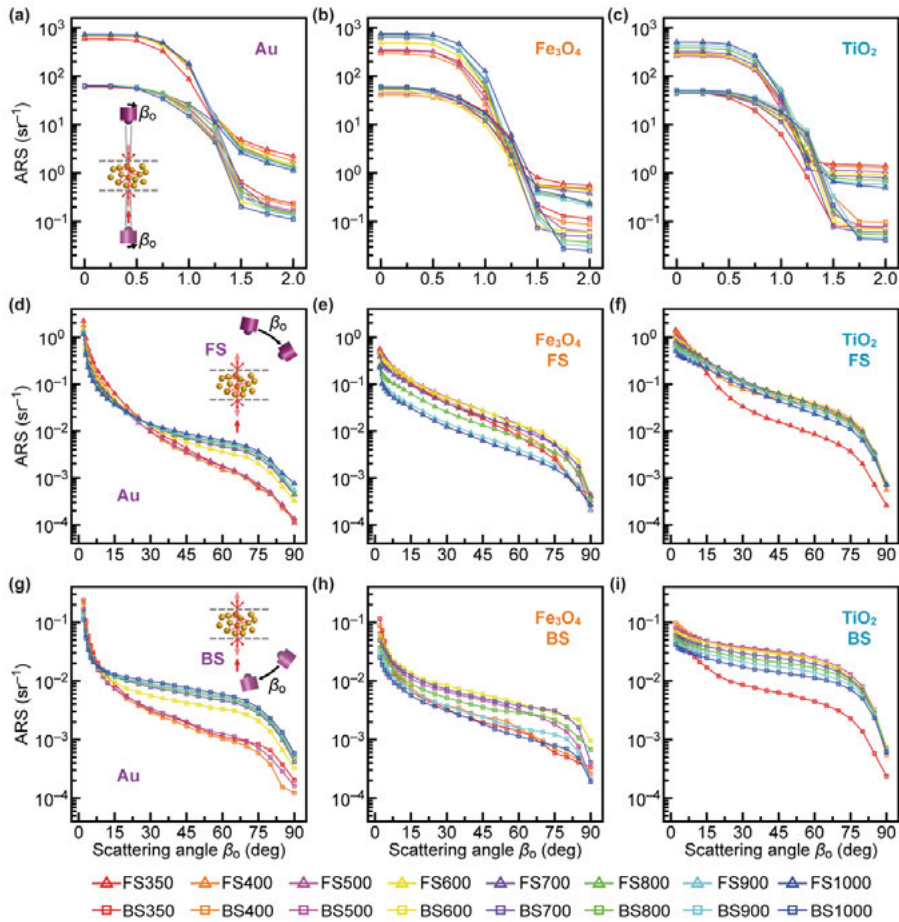


Figure 5.13. Angular and spectral resolved scattering properties from an in-plane angle resolved spectrometer. a-c) Small-angle forward (triangles) and backward (squares) scattering intensity, d-f) forward scattering, and g-i) backward scattering for Au (left column),  $\text{Fe}_3\text{O}_4$  (middle column), and  $\text{TiO}_2$  (right column) as a function of scattering angle and at wavelengths from 350 nm to 1000 nm (see legend below the figure). The insets in (a), (d), (g) show the detector's trajectory at small-angle, forward, and backward regions.



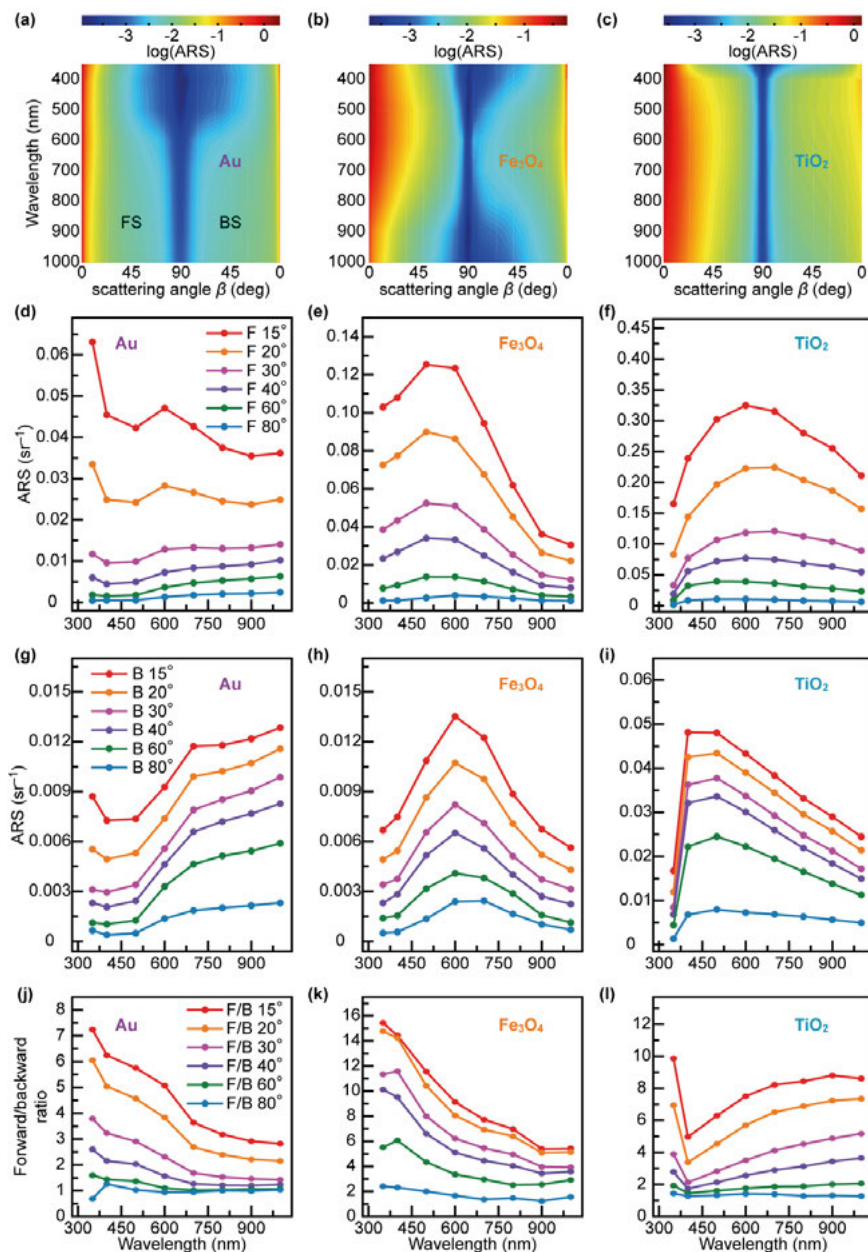


Figure 5.14. Spectral forward and backward scattering profiles. a-c) Measured forward and backward scattering intensity as a function of wavelength at different scattering angles for (a) Au, (b)  $\text{Fe}_3\text{O}_4$  and (c)  $\text{TiO}_2$ . d-i) Selected forward and backward scattering spectra at varied angles as a function of wavelength for (d,g) Au (e,h)  $\text{Fe}_3\text{O}_4$  and (f,i)  $\text{TiO}_2$ . j-l) Forward to backward intensity ratio at selected angles as a function of wavelength for (j) Au, (h)  $\text{Fe}_3\text{O}_4$  and (i)  $\text{TiO}_2$ . At higher angles, the forward to backward ratio decreases and becomes close to unity when the scattering angle is equal to  $80^\circ$ .

The accuracy and reproducibility of the angle-resolved measurements are verified in Figure 5.15, measuring the forward and backward scattering intensity on different days for TiO<sub>2</sub> sample with an incident light of 900 nm.

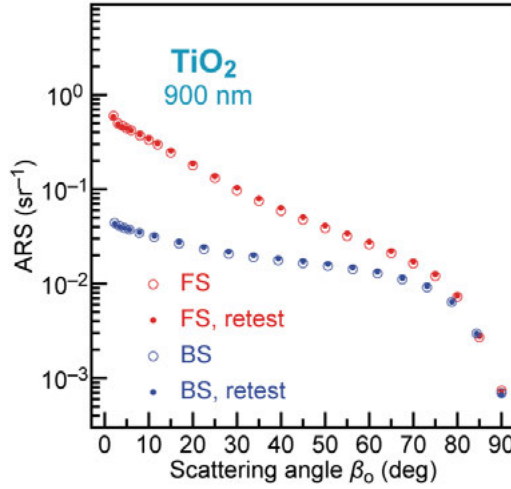


Figure 5.15. Forward and backward scattering intensity ( $\text{sr}^{-1}$ ) as a function of angle conducted on different days (open circle and solid dot) on the TiO<sub>2</sub> sample ( $\lambda = 900$  nm).

## 5.5 Integration of angle resolved data

The measured angle-resolved scattering intensity can be integrated over the forward and backward hemispheres in order to obtain the diffuse and regular/specular transmittance and reflectance. We then compared the integrated  $ARS(\beta)$  with measured values of  $T_{\text{dif}}$ ,  $R_{\text{dif}}$ ,  $T_{\text{reg}}$  and  $R_{\text{spe}}$  obtained from the spectrophotometer. In the case when the scattering is not dependent on the azimuthal angle, the integration was carried out according to<sup>89</sup>

$$T_{\text{dif}} = \int_{\text{reg}}^{90^\circ} 2\pi ARS(\beta) \sin(\beta) d\beta \quad (5.1)$$

$$R_{\text{dif}} = \int_{\text{spe}}^{90^\circ} 2\pi ARS(\beta) \sin(\beta) d\beta \quad (5.2)$$

$$T_{\text{reg}} = T(0^\circ) + \int_{0^\circ}^{2^\circ} 2\pi ARS_{\text{ext}}(\beta) \sin(\beta) d\beta + \int_{2^\circ}^{\text{reg}} 2\pi ARS(\beta) \sin(\beta) d\beta \quad (5.3)$$

$$R_{\text{spe}} = R(0^\circ) + \int_{0^\circ}^{2^\circ} 2\pi ARS_{\text{ext}}(\beta) \sin(\beta) d\beta + \int_{2^\circ}^{\text{spe}} 2\pi ARS(\beta) \sin(\beta) d\beta \quad (5.4)$$

Here *reg* and *spe* represent the upper limit of the angular ranges for  $T_{\text{reg}}$  and  $R_{\text{spe}}$ , as determined by the geometry of the integrating sphere of the spectrophotometer, *i.e.* 4.6° and 7.4°. The  $ARS_{\text{ext}}(\beta)$  denotes the extrapolation of the diffuse scattering intensity from 2° to 0°.  $T(0^\circ)$  and  $R(0^\circ)$  are the measured



transmittance and reflectance with the detector positioned at  $0^\circ$ . Figure 5.16 shows the integrated ARS results in comparison with the transmittance and reflectance spectra measured by the spectrophotometer. The results are in good agreement, proving the accuracy of the instruments and the measurement procedures.

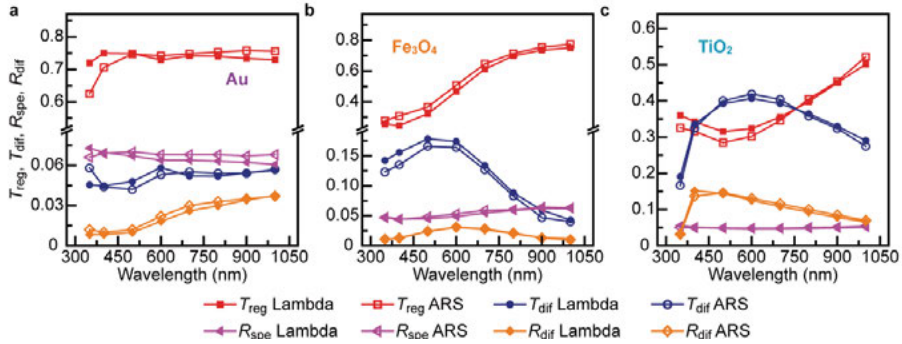


Figure 5.16. Comparison of  $T_{\text{reg}}$ ,  $T_{\text{dif}}$ ,  $R_{\text{spe}}$ ,  $R_{\text{dif}}$  from Lambda 900 to those from the integrated ARS at different wavelengths for (a) Au, (b)  $\text{Fe}_3\text{O}_4$  and (c)  $\text{TiO}_2$  nanoparticle samples.

## 5.6 Conversion of angle resolved data into scattering phase function

With knowledge of the angular scattering profiles outside the scattering layer, the scattering phase function of the nanoparticle composite inside the scattering layer can be obtained by considering Snell's law and Fresnel's law (Chapter 2.6). Figure 5.17 shows a typical example of converting the observed outer forward  $\text{ARS}_f(\beta_o)$  and backward  $\text{ARS}_b(\beta_o)$  intensities into  $\text{ARS}_{f,b}(\beta_i)$  for the Au sample at a wavelength of 600 nm. Scattering phase function should exclude the collimated incident beam, i.e. angles smaller than  $2^\circ$  outside the film, which are converted to  $1.3^\circ$  inside the film (Figure 5.17a).  $\text{ARS}_{f,b}(\beta_i)$  was converted into the BSDF  $f_{t,r}(\beta_i)$  (equation 2.58 and 2.59) as shown in Figure 5.17b. As the phase function spans from  $0^\circ$  to  $180^\circ$ , the inner scattering distribution values we derive from the ARS measurement are only a part of the complete phase function. An empirical phase function is needed to fill the gap at angles larger than the critical one. Herein, we use a two-term Reynolds-McCormick<sup>84</sup> phase function (denoted as TTRM, Chapter 2.6) in order to obtain an approximation of the whole scattering profile. The TTRM phase function is able to fit simultaneously peaked scattering intensities in forward and backward directions. The fitting range is  $1.3^\circ$  to  $39^\circ$  inside the film. We restrict the fit to  $39^\circ$  because of the lower measurement accuracy at outer angles close to  $90^\circ$ , together with errors due to scattered light coming from the sample edge.

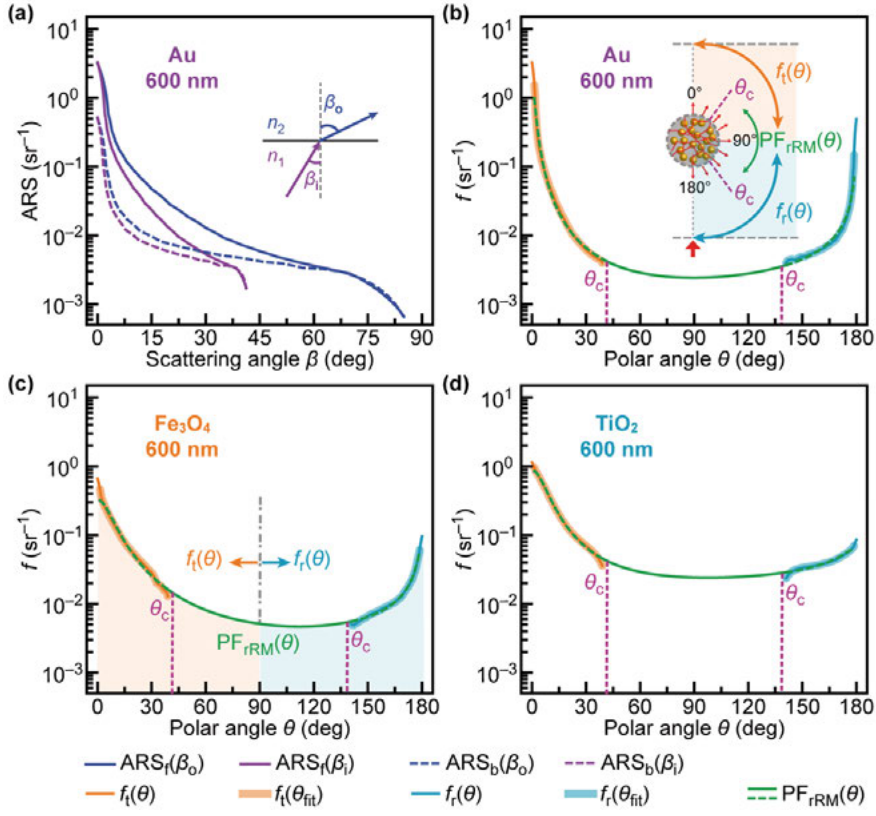


Figure 5.17. Rescaled forward and backward intensity distribution fitted by rRM phase function. a) Conversion of the observed outer  $\text{ARS}_{\text{f,b}}(\beta_o)$  into those inside the scattering layer  $\text{ARS}_{\text{f,b}}(\beta_i)$  by Snell's law. Inset shows the angle conversion due to the difference of refractive index between the scattering matrix and air at the interface. Fitting of the BSDF  $f_{\text{t,r}}(\theta)$  within the scattering layer by use of the rRM approach ( $\text{PF}_{\text{rRM}}(\theta)$ ) for b) Au, c)  $\text{Fe}_3\text{O}_4$ , and d)  $\text{TiO}_2$  samples at  $\lambda = 600$  nm. Inset in (b) illustrates the inner forward and backward scattering distribution  $f_{\text{t,r}}(\theta)$  and the rRM simulated regions within the film.

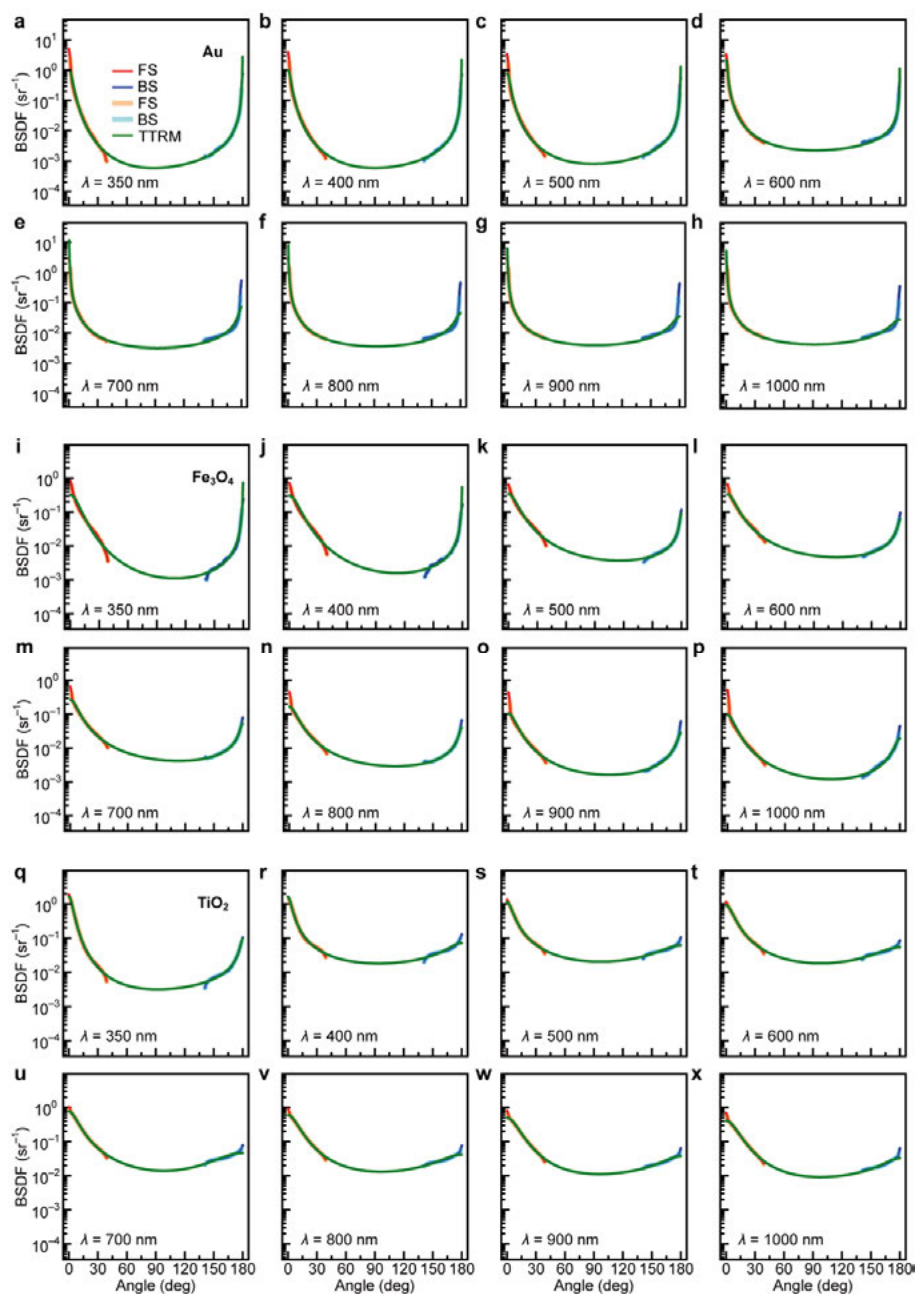


Figure 5.18. Fitting of the forward and backward scattering distributions for a Au (a-h),  $\text{Fe}_3\text{O}_4$  (i-p) and  $\text{TiO}_2$  (q-x) samples at wavelengths from 350 nm to 1000 nm by using of the TTRM phase function approximation.

A good agreement between the experimental forward and backward branches (orange and cyan thick lines) to the fitted TTRM (dotted green curve) can be

seen in Figure 5.17b-d for the samples at 600 nm. A more detailed TTRM fitting on three samples at varied wavelengths is shown in Figure 5.18, indicating that TTRM is suitable to use in different situations.

The final phase function inside the scattering layer  $f_{t,r}(\theta)$  is obtained by combining the converted forward and backward portion (orange and cyan) together with the TTRM fitting curve (solid green).

## 5.7 Comparison of different scattering phase functions

In chapter 2.6, different empirical scattering phase functions are introduced. Eight different analytic approximations to the phase function, namely, RM, TTRM, HG, TTHG, FF, TTFF, CS and PARA, were fitted to the experimental data. The above-mentioned phase functions emerge from physical arguments, apart from PARA, which is a mathematical analytic form we proposed for fitting forward and backward peaked scattering distribution based on a parabolic curve as below:

$$P_{PARA}(\theta, a, b, c) = \exp[a + b(\theta - c)^2] \quad (5.5)$$

The quality of fit was described by the mean square logarithmic error (MSLE) criterion, which was used to find the difference in the fitted curve to the BSDF from the experiment:

$$MSLE = \sqrt{\frac{\sum_0^\theta [\log[I(\theta_i)] - \log[F(\theta_i)]]^2}{N}} \quad (5.6)$$

The reason for taking logarithmic error is because there are orders of magnitude difference within the same scattering profiles, otherwise the fitting will be dominated by the largest values. The fitting curves (green) and the MSLE of the TTRM, TTHG, PARA, TTFF and CS approximations for a  $\text{Fe}_3\text{O}_4$  sample are plotted in Figure 5.19a-e. Among them, TTRM exhibits the lowest MSLE for all the samples at all wavelengths, followed by the TTHG and PARA approximations (Figure 5.19f-g). CS shows the worst fit among these five methods, probably because it only contains one fitting parameter,  $g$ , and is more suitable for fitting a Rayleigh-like scattering phase function.

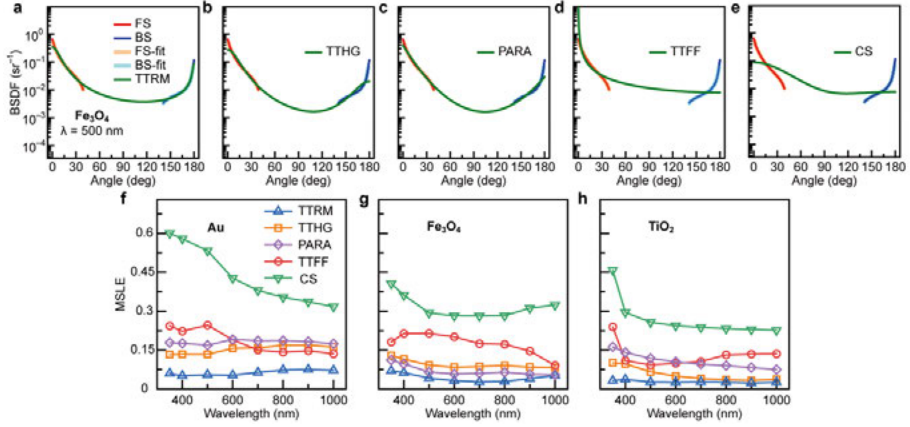


Figure 5.19. Fitting of the forward and backward scattering distributions for a  $\text{Fe}_3\text{O}_4$  nanosphere sample at a wavelength of 500 nm by the (a) TTRM, (b) TTHG, (c) PARA, (d) TTFF, and (e) CS empirical phase functions. (f-g) Mean square logarithmic error (MSLE) of the above five methods at wavelengths from 350 nm to 1000 nm, for Au (f),  $\text{Fe}_3\text{O}_4$  (g) and  $\text{TiO}_2$  (h) samples.

The MSLE of HG, RM, FF (chapter 2.6) are much higher than their two-term forms, mainly because they fail to reproduce the backscattering peaks (Figure 5.20).

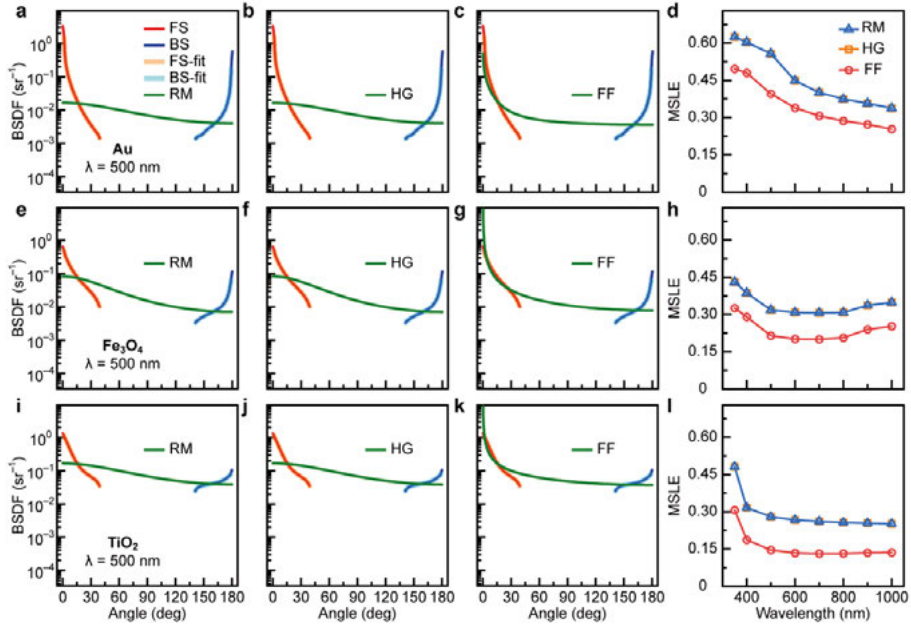


Figure 5.20. Fitting of the forward and backward scattering distributions for Au (a-c),  $\text{Fe}_3\text{O}_4$  (e-g) and  $\text{TiO}_2$  (i-k) samples at a wavelength of 500 nm, first column, RM, second column, HG, third column, FF phase functions. (d,h,l) Mean square logarithmic error (MSLE) of these three methods at wavelengths from 350 nm to 1000 nm (fourth column). HG and RM errors overlap.

TTRM has the lowest MSLE among these approximations and can fit our experimental scattering distribution with good accuracy. In order to verify the feasibility of the TTRM function in a broader context, we now compare TTRM with the Mie scattering phase function, which describes scattering from a single particle or the single scattering regime of a nanoparticle composite. Mie theory<sup>31</sup> calculates the far-field scattering pattern around the particle. The Mie phase function considering the measured size distributions of the three types of particles from SEM images with average diameters about 200 nm are plotted and fitted by the TTRM expression as a function of wavelength from 400 nm to 1200 nm (Figure 5.21). Results show that the TTRM function overlaps with the Mie phase functions in many cases, but slight discrepancies appear when there are oscillations in the Mie calculations due to interference effects. From the scattering phase function, one can notice that at shorter wavelengths, forward scattering is dominant while the backward portion increases with increasing wavelength.

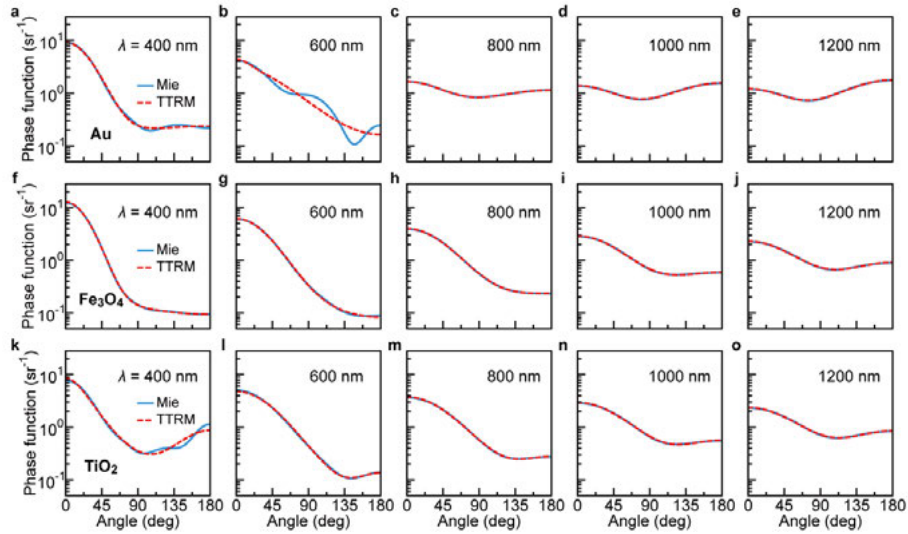


Figure 5.21. Comparison of TTRM (red) phase functions with Mie (blue) phase functions for Au (upper row),  $\text{Fe}_3\text{O}_4$  (middle row) and  $\text{TiO}_2$  (lower row) particles at wavelengths of 400 nm, 600 nm, 800 nm, 1000 nm and 1200 nm. The Mie calculations were carried out using the experimental size distributions of nanoparticles with average diameters around 200 nm.

We now explore the cases of phase functions from Mie theory for particles with diameters different from 200 nm. The size parameter,  $x$  is frequently used in the field of optical scattering to define different scattering domains. For  $x$  significantly less than one (with particle size  $< 1/10$  wavelength), one has Ray-



leigh scattering is used (chapter 2.6). For  $x > 20$  one enters the geometric optics regime and the intermediate regime is often called the Mie scattering regime.

In the Mie region, the scattering pattern becomes more anisotropic and forward scattering dominates more and more as the particle size increases. We chose Mie calculations for a wavelength of 600 nm, with diameters of the single particles equal to 50, 150, 300, 500 and 1000 nm, corresponding to size parameters  $x$  equal to 0.26, 0.79, 1.57, 2.62 and 5.24, and fitted them by using the TTRM function (Figure 5.22). Multiple peaks appear when  $x$  is larger than one. The fitting in the Rayleigh region (first column), and Mie region when  $x$  is smaller than unity (second column), between the TTRM and Rayleigh/Mie phase functions is excellent. The TTRM function still follows the trend when  $x$  is larger than 1, although it does not describe the multiple peaks occurring due to interference. However, in practical light scattering measurements, these peaks are usually smoothed, due to the size and shape distributions of the particles.

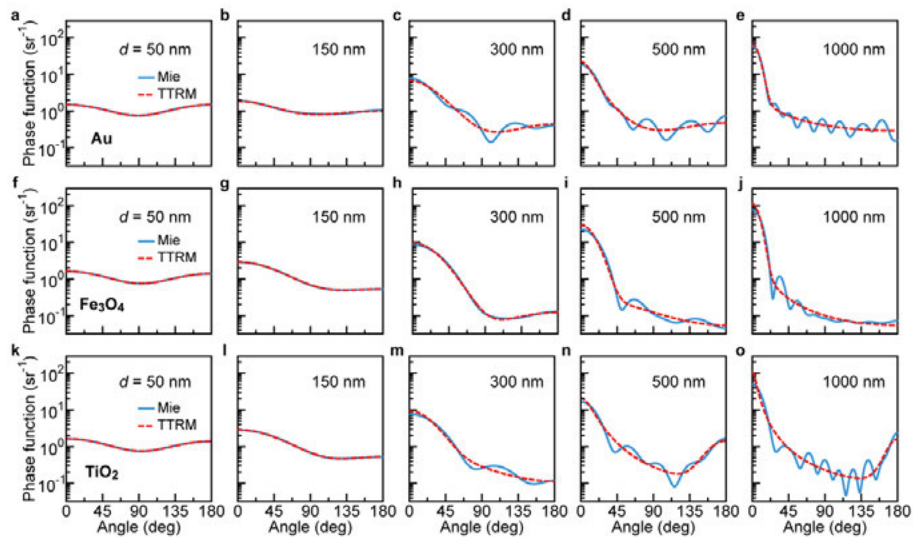


Figure 5.22. Comparison of the TTRM (red) phase function with Mie scattering model (blue) for Au (upper row),  $\text{Fe}_3\text{O}_4$  (middle row) and  $\text{TiO}_2$  (lower row) particles with diameters of 50 nm, 150 nm, 300 nm, 500 nm and 1000 nm. The simulation was conducted at a wavelength of 600 nm.

In addition, multiple scattering and the surface roughness of the particles may also contribute to this effect. Diameters of 2000 nm ( $x = 10.5$ ), 4000 nm ( $x = 21.0$ ), 10000 nm ( $x = 52.4$ ) are plotted in Figure 5.23, illustrating the fitting capability of the TTRM also in the geometric optics regime.

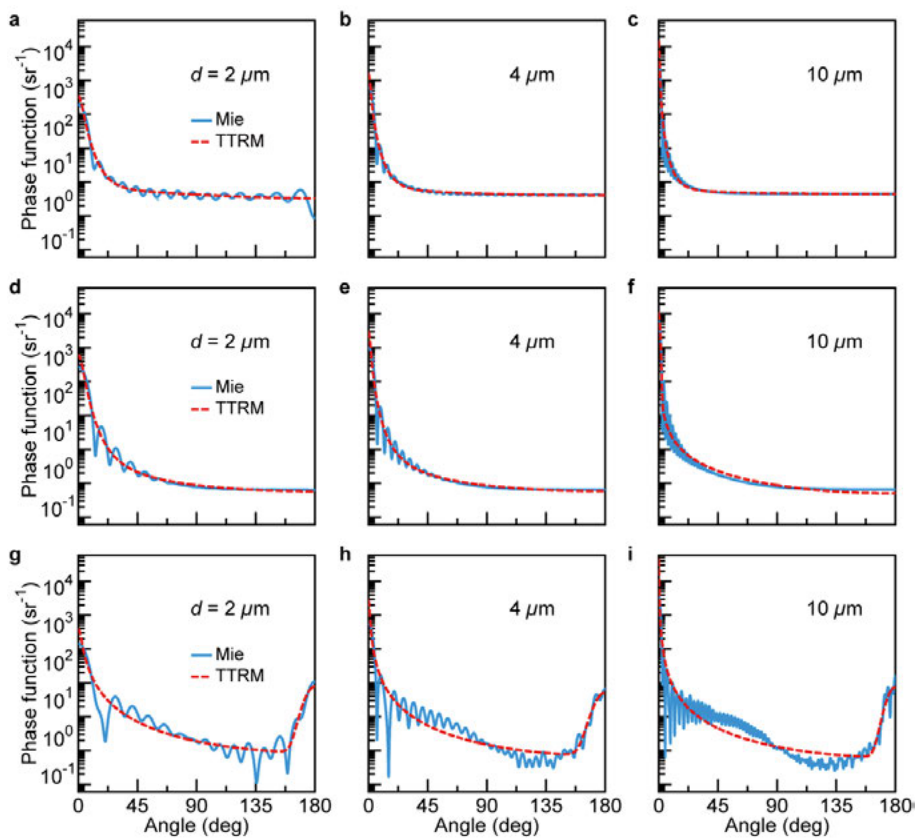


Figure 5.23. Comparison of TTRM phase function (red) with the phase function computed from Mie scattering models (blue) for Au (a-c), Fe<sub>3</sub>O<sub>4</sub> (d-f) and TiO<sub>2</sub> (g-i) at particle diameters of 2000 nm, 4000 nm and 10000 nm. The simulation is conducted at a wavelength of 600 nm.



## 5.8 Single-particle spectra for Au, Fe<sub>3</sub>O<sub>4</sub> and TiO<sub>2</sub> nanospheres

Previous study focused on a cloud of particles, the scattering behavior of which is influenced by multiple scattering. In this section, single-particle scattering spectra are evaluated for these metallic and dielectric nanospheres. The single nanoparticles, which were deposited on an ITO substrate, can be observed from SEM images (Figure 5.24). Both metallic and dielectric single particles can support strong scattering resonances at optical frequencies, as can be observed from the dark-field optical microscope (chapter 3) images in the forward and backward directions (Figure 5.24). The color difference of the different materials is due to differences in position of multipole resonance peaks<sup>12-13</sup>. The three types of particles have a similar size parameter with sizes around 200 nm. The only difference is the index of refraction for different types of nanoparticles, and therefore, the difference of dielectric permittivity which is negative for metals and positive for dielectrics.

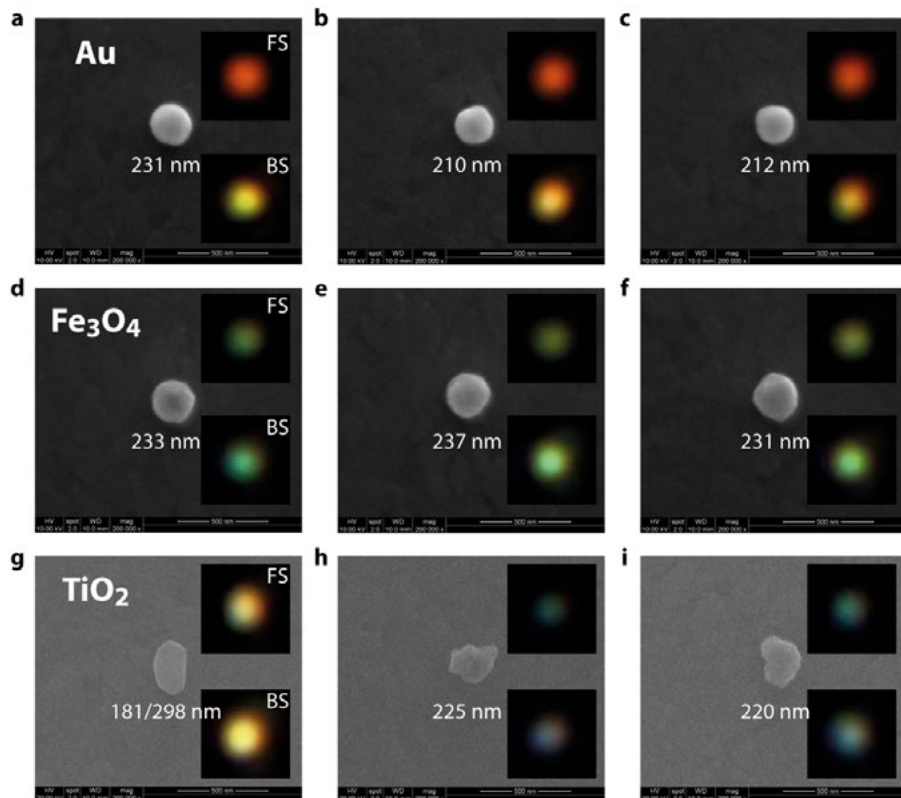


Figure 5.24. Scanning electron microscope images of three single particles (#1, #2, #3) of Au (a-c), Fe<sub>3</sub>O<sub>4</sub> (d-f), and TiO<sub>2</sub> (g-i). Insets are dark-field optical microscope images of the same particles for forward scattering (top right) and backward scattering (bottom right).

Small size nanoparticles mainly produce dipole resonances. With the increment of the size of the nanoparticle, multipolar resonances, such as quadrupolar, octupolar resonances, are generated. Metallic particles, such as Au, show localized surface plasmon resonances and mainly generate electric-dipoles. Dielectric particles support both electric- and magnetic- type resonances of comparable strength<sup>12</sup>. Figure 5.25 shows the Mie simulation results together with the dark-field scattering spectra of three particle types. The dark-field scattering spectra for three particles of the same type of material are similar. Only the #1 of the TiO<sub>2</sub> samples varied compared to the other two nanospheres, mainly because of the size and shape difference. The difference between experiments and Mie calculations is due to the fact that the nanospheres are located on the conducting ITO substrate, and interaction of ITO with the particles cannot be ignored. The Mie simulation assumes that the nanosphere is surrounded by air. The particle resonances interact with the substrate and thus modify the spectra which has been systematically studied by Videen<sup>103-105</sup> and Bobbert et al<sup>106</sup> for the sphere-substrate geometry. An assumption by Videen<sup>105</sup> is that the scattered field generated by the nanosphere is reflected off the surface and interacts with the nanosphere. It is thus incident upon the surface at near-normal incidence. Another reason for the spectra mismatch is that in Mie simulations, the scattering cross sections were integrated in the forward or backward hemispheres. In our experiments, the scattering spectra were only collected in a limited angular range due to the geometry of the optical systems (chapter 4). Further efforts are required: (i) The Mie spectra simulated in Figure 25 a-c should consider the particle-substrate interaction, (ii) the experimental scattering spectra should be multiplied by a correction factor as a function of wavelength. The correction factor is the ratio of the integrated intensity from the measured 120° angle range to the integrated intensity over a hemisphere, as determined from the scattering phase functions of the nanospheres.

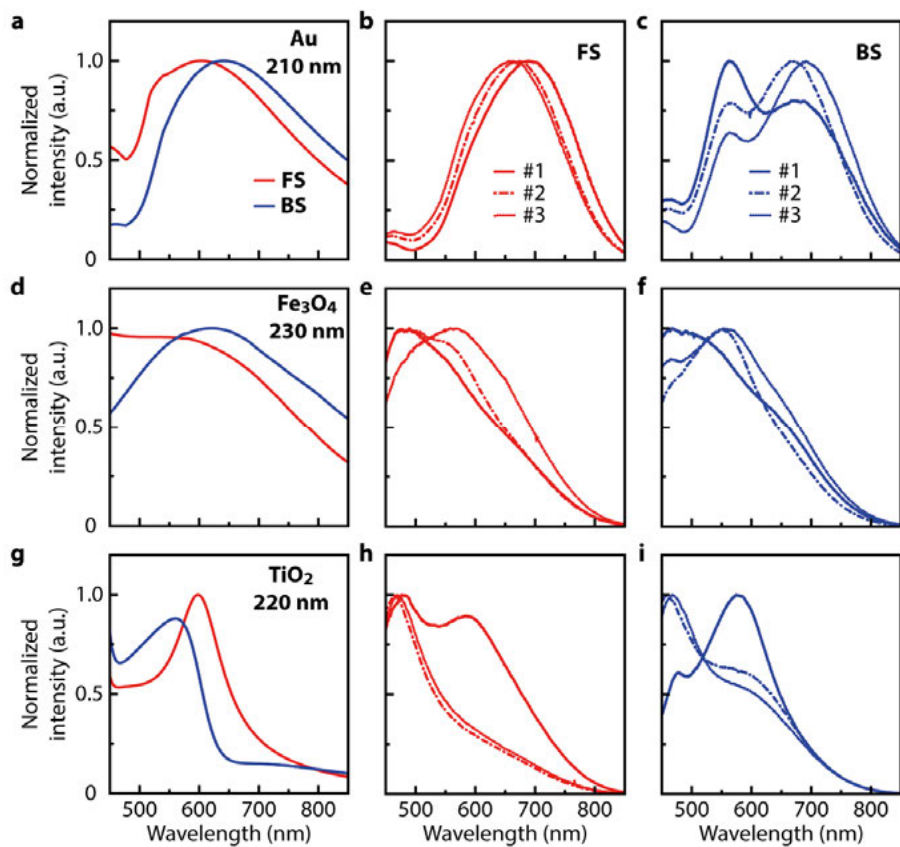


Figure 5.25. Forward and backward scattering cross section simulated by Mie theory on Au with 210 nm in diameter (a), Fe<sub>3</sub>O<sub>4</sub> with 230 nm in diameter (d), and TiO<sub>2</sub> with 220 nm in diameter (g). Dark-field scattering spectra of forward and backward scattering on Au (b,c), Fe<sub>3</sub>O<sub>4</sub> (e,f) and TiO<sub>2</sub> (h,i).

## 6. Determination of scattering and absorption coefficients from spectrophotometric data

### 6.1 Previous methods to determine scattering and absorption coefficients

The simplest theoretical description of the optical properties of a plane-parallel layer of an absorbing and scattering medium is the Kubelka-Munk two flux theory<sup>67-68, 107-108</sup>. The first radiative transfer model of this type was formulated by Schuster<sup>65</sup> and Schwarzschild<sup>66</sup>, taking into account two isotropic diffuse components of the radiation field in the forward and backward hemispheres. In later studies by Kubelka and Munk, the phenomenological two-flux model was proposed for analyzing the transmittance and reflectance of paint layers or other scattering coatings<sup>1, 69</sup>. The theory is formulated in terms of effective backscattering ( $S$ ) and absorption ( $K$ ) coefficients of the light scattering material. However, the calculation of these parameters from optical measurements is problematic, because the angular dependence of the radiation field in the material as well as the surface reflection coefficients are often not well characterized.

Previous methods for obtaining scattering and absorption coefficients from  $R$  and  $T$  measurements have disadvantages. The two-background method<sup>109</sup> depends on the accurate characterization of a white and a black reference material. Other approaches to the inverse problem are computationally complex and involve Monte-Carlo simulations<sup>51-52</sup> and comparisons with solutions of the general radiative transfer equation<sup>5, 53</sup>. A simpler alternative is offered by inversion schemes using the two-flux theory<sup>2, 30</sup>, but it was found that the  $T$  and  $R$  values obtained from the solutions for  $S$  and  $K$  in certain cases did not converge to the experimental data. We have identified this deficiency as being due to an assumption of isotropic diffuse scattering in the composite layer, as shown below. An advantage of the Kubelka-Munk theory is that it can be formulated in matrix form<sup>110</sup> and hence can be extended to multilayers in a straightforward way. This provides a possible route to determine the optical parameters of an unknown layer in an otherwise known multilayer stack.

## 6.2 New methods using angle resolved scattering information

In the Kubelka-Munk two flux theory to determine  $S$  and  $K$ , totally five parameters are unknown. They are  $S$ ,  $K$ ,  $R_c$ ,  $R_g$ , and  $R_j$ . There are two equations (equations 2.26 and 2.27), and  $R_c$  can be determined by equation 2.28 and 2.29. The main challenge is the interface reflectances  $R_g$  and  $R_j$ , which are dependent on angular scattering profiles of the nanoparticle composites. The challenge lies in the characterization of the inner scattering phase function of the nanocomposite, and therefore, the interface reflectances  $R_{g,j}$ . The real scattering phase function of the nanoparticle composite layer is highly dependent on the types of nanoparticle, volume fraction, size, etc. The degree of aggregation of the nanoparticles inside the scattering layer is also important as it can vary the scattering phase function. The interface reflectances  $R_{g,j}$  are given by

$$R_{g,j} = (1 - q_{0,d})R_c + q_{0,d}R_{df,db} \quad (6.1)$$

where  $q_0$  and  $q_d$  are defined as the diffuse light fractions in the film close to the back interface and front interface, according to

$$q_0 = \frac{I(0) - I_c(0)}{I(0)} \quad (6.2)$$

$$q_d = \frac{J(d) - J_c(d)}{J(d)} \quad (6.3)$$

The intensity passing towards the back interface is denoted  $I$  and the intensity towards the front interface is denoted  $J$ . In addition, the subscripts 0 and  $d$  represent the back and front interfaces, respectively, and the subscript  $c$  signifies the collimated light.  $q_{0,d}$  can be calculated from transmittance and reflectance spectra according to Barrios *et al*<sup>30</sup>

$$q_0 = \frac{T_{dif}(1 - R_c)}{T_{tot}(1 - R_c) - T_{reg}(R_{df} - R_c)} \quad (6.4)$$

$$q_d = \frac{R_{dif}(1 - R_c)}{R_{tot}(1 - R_c) - R_{spe}(R_{db} - R_c) + R_c R_{db} - R_c} \quad (6.5)$$

$T_{dif}$ ,  $T_{tot}$ ,  $T_{reg}$ ,  $R_{dif}$ ,  $R_{tot}$ ,  $R_{spe}$  are experimental results and  $R_c$  can be determined by equation 2.28 and 2.29. From the knowledge of diffuse interface reflectance  $R_{df,db}$  and the diffuse light fractions  $q_{0,d}$ , the total interface reflectances  $R_{g,j}$  can be determined by equation 6.1. The question is how to determine the interface reflectance  $R_{df,db}$ . In chapter 5 we introduced an experimental approach to determine the scattering phase function with the presence of the angle resolved scatterometer. We denoted this method as **ARS**. In the **ARS** approach, the forward and backward internal diffuse reflectance values at the back and front interface  $R_{df,db}$  can be written

$$R_{df,db} = \frac{\int_{0^\circ}^{90^\circ} f_{t,r}(\beta) r(\beta) \sin(2\beta) d\beta}{\int_{0^\circ}^{90^\circ} f_{t,r}(\beta) \sin(2\beta) d\beta} \quad (6.6)$$

$R_{df,db}$  can be derived by averaging the inner angular scattering pattern  $f_{t,r}(\beta)$  at the front and back interfaces, multiplied by the interface reflection coefficient  $r(\beta)$  (chapter 2), over the angles ( $0^\circ$ ,  $90^\circ$ ) from the forward and backward directions.

In the absence of an angle resolved scatterometer, approximations of the scattering profiles are essential. Previous models assume that the forward and backward scattering profiles are isotropic.<sup>2, 30</sup> The assumption fails for a weakly scattering film<sup>2</sup> and for larger particles with an asymmetric scattering phase function.<sup>30</sup> We denoted this approach as **dif**, and in this approximation we assumed an isotropic scattering profile of diffuse light for both forward and backward directions for the nanoparticle samples. We defined  $R_d$  as the total diffuse interface reflectance when light was incident from the sample to air,<sup>111</sup> therefore

$$R_{df} = R_{db} = R_d = \frac{\int_{0^\circ}^{90^\circ} r(\beta) \sin(2\beta) d\beta}{\int_{0^\circ}^{90^\circ} \sin(2\beta) d\beta} \quad (6.7)$$

We also proposed several approximations when angle resolved scatterometers are not available. In the **Mie** approximation,  $R_{df}$  and  $R_{db}$  were determined by the phase function of the nanospheres from Mie theory,

$$R_{df,db} = \frac{\int_{0^\circ}^{90^\circ} P_{f,b}(\beta) r(\beta) \sin(2\beta) d\beta}{\int_{0^\circ}^{90^\circ} P_{f,b}(\beta) \sin(2\beta) d\beta} \quad (6.8)$$

where  $P_f(\beta)$  is the phase function obtained from Mie calculations in the range ( $0^\circ$ ,  $90^\circ$ ) and  $P_b(\beta)$  is the phase function in the range ( $90^\circ$ ,  $180^\circ$ ), here converted to the  $\beta$  range ( $0^\circ$ ,  $90^\circ$ ).

In the **cri** approximation, we computed  $R_d$  in analogy to the **dif** method, but restricted the scattered light in the forward and backward directions to angles less than the critical angle, hence

$$R_{df} = R_{db} = \frac{\int_{0^\circ}^{\theta_c} r(\beta) \sin(2\beta) d\beta}{\int_{0^\circ}^{\theta_c} \sin(2\beta) d\beta} \quad (6.9)$$

The critical angle  $\theta_c$  is the angle above which total internal reflection occurs so that  $r_s=r_p=1$ , and it is wavelength-dependent. In our case it was determined for the glass/air interface.

In the **cri/dif** approximation, the scattering angle was restricted by the critical angle in the forward direction and went to the full  $90^\circ$  in the backward direction.

$$R_{df} = \frac{\int_{0^\circ}^{\theta_c} r(\beta) \sin(2\beta) d\beta}{\int_{0^\circ}^{\theta_c} \sin(2\beta) d\beta} \quad (6.10)$$

$$R_{db} = \frac{\int_{0^\circ}^{90^\circ} r(\beta) \sin(2\beta) d\beta}{\int_{0^\circ}^{90^\circ} \sin(2\beta) d\beta} \quad (6.11)$$

We now have five different approaches to determine the forward and backward internal diffuse reflectance at the back and front interface  $R_{df,db}$ , namely **ARS**, **Mie**, **cri**, **dif**, **cri/dif** as shown in Table 1.

Table 1. Methods for determining scattering and absorption coefficients.

<b>ARS method</b>	Method to determine scattering ( $S$ ) and absorption ( $K$ ) coefficients, wherein the light scattering distribution is obtained from the angle and wavelength resolved scattering measurements
<b>cri method</b>	Method to determine $S$ and $K$ , wherein the light scattering distribution is assumed to be restricted to angles below the critical angle in both forward and backward directions
<b>cri/dif method</b>	Method to determine $S$ and $K$ , wherein the light scattering distribution is assumed to be restricted by the critical angle in the forward direction and isotropic in the backward direction
<b>dif method</b>	Method to determine $S$ and $K$ , wherein the light scattering distribution is assumed to have an isotropic scattering profile in both forward and backward directions
<b>Mie method</b>	Method to determine $S$ and $K$ , wherein the light scattering distribution is obtained from the phase function computed from Mie theory

### 6.3 Backscattering and absorption coefficients inversion of Kubelka-Munk model

Five approximations with different diffuse reflectance at the back and front interface  $R_{df,db}$  are put into two flux equations (equation 6.1, 6.4, 6.5, 2.24, 2.25, 2.26, 2.27) to derive backscattering ( $S$ ) and absorption ( $K$ ) coefficients for Au, Fe<sub>3</sub>O<sub>4</sub> and TiO<sub>2</sub> samples. Their residual spectra are shown in Figure 6.1, demonstrating a failure of **dif** and **Mie** approximations. From the inner scattering phase function patterns used in the **ARS** method, we can now readily understand the failure of the **dif** method. It assumes isotropic diffuse scat-

tering in forward and backward directions. In our cases, however, the scattering patterns are anisotropic, exhibiting a strong increase towards small scattering angles. The failure of **Mie** is that it only considers the single particle scattering case. In real situations, however, multiple scattering and aggregation of the nanoparticles complicate the calculations. The **ARS**, **cri**, and **cri/dif** approximations converge. The most accurate method is based on the **ARS**, which exhibited the real scattering phase function derived from the experimental measurements.

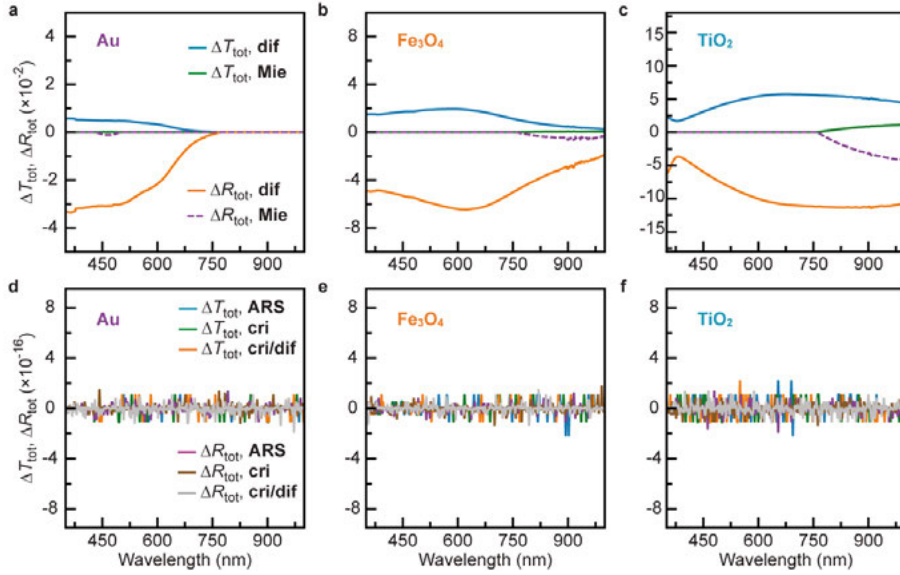


Figure 6.1. a–c) Residual spectra ( $T_{\text{tot}}(\text{experiment}) - T_{\text{tot}}(\text{simulation})$ ) and ( $R_{\text{tot}}(\text{experiment}) - R_{\text{tot}}(\text{simulation})$ ) of the **dif** and **Mie** methods for Au (a),  $\text{Fe}_3\text{O}_4$  (b) and  $\text{TiO}_2$  (c), showing significant differences between the experimental results and those of the fitting. d–f) Residual spectra of **ARS**, **cri**, and **cri/dif** methods for the three samples illustrate the good convergence of these methods.

Figure 6.2 gives the intermediate results of the internal diffuse reflectance at the back and front interface  $R_{\text{df,db}}$  and diffuse light fractions in the film close to the back interface and front interface  $q_{0,d}$  by the **ARS** approach for three samples. The higher value of  $R_{\text{db}}$  to  $R_{\text{df}}$  indicates that the backward scattering is more isotropic than the forward one, indicating more scattered light distribution at higher angles.  $q_{0,d}$  gives the diffuse light fraction, and a higher value represents a less collimated light contribution. For example,  $q_0$  of the  $\text{TiO}_2$  sample is very close to unity in the backward direction, indicating that the light flux mainly comes from the diffuse scattering of light.



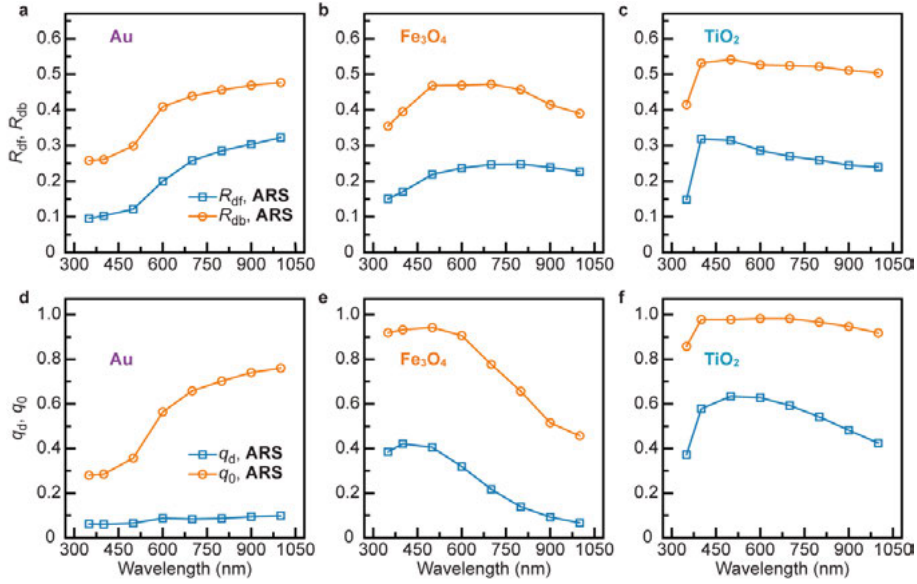


Figure 6.2. (a–c) Forward ( $R_{df}$ ) and backward ( $R_{db}$ ) diffuse interface reflectance from the **ARS** method for Au (a),  $Fe_3O_4$  (b) and  $TiO_2$  (c). d–f) diffuse light fractions in the film close to the back ( $q_0$ ) and front ( $q_d$ ) interface from the **ARS** method of the three samples.  $R_{df}$  and  $R_{db}$  from the **ARS** are interpolated between the wavelengths used in the angle resolved scattering measurements.

Wavelength dependent  $R_g$  and  $R_j$  derived from the **ARS**, **cri**, **cri/dif** methods are shown in Figure 6.3a–c for the three samples. Higher  $R_j$  than  $R_g$  values show that the backscattering fluxes are more isotropic than the forward ones, indicating a forward peaked scattering pattern. Now  $S$  and  $K$  can be numerically solved from the above equations (equation 6.1, 6.4, 6.5, 2.24, 2.25, 2.26, 2.27) and the results are given in Figure 6.3d–f ( $S$ ) and Figure 6.3g–i ( $K$ ). The results show that  $K$  is quite insensitive to the details of the model used to derive it. However,  $S$  derived by the **cri** method is much closer to the exact value from the **ARS** method, as compared with the **cri/dif** result. For all three samples, the  $R_g$  derived from the **ARS** method is between 0.05 and 0.25, indicating a less forward peaked scattering pattern than assumed in the **cri** and **cri/dif** methods. On the other hand,  $R_j$  from the **ARS** method is always between the values obtained from the **cri** and **cri/dif** methods, which indicates that the real backscattering pattern is somewhere between these assumptions. From the wavelength dependent  $R_g$  and  $R_j$  derived from **ARS**, we found that the  $TiO_2$  sample exhibited higher values than the Au and  $Fe_3O_4$  samples. This indicates a larger portion of light scattering at high angles (more diffuse) for  $TiO_2$ .

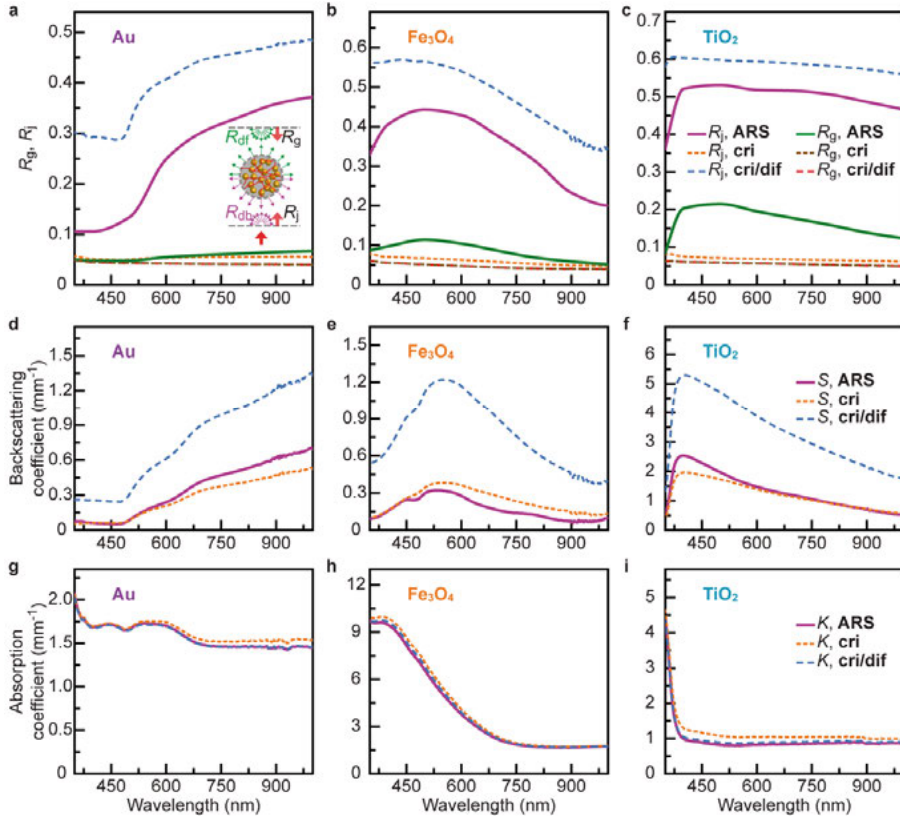


Figure 6.3. (a-c) Back interface reflectance  $R_g$  and front interface reflectance  $R_j$  (inset) calculated by **ARS**, **cri** and **cri/dif** methods for Au,  $\text{Fe}_3\text{O}_4$  and  $\text{TiO}_2$  samples. (d-f) Backscattering coefficient  $S$  derived from  $R_g$ ,  $R_j$  by **ARS**, **cri** and **cri/dif** methods. (g-i) Absorption coefficient  $K$  derived from  $R_g$ ,  $R_j$  by **ARS**, **cri** and **cri/dif** methods.

## 6.4 Size dependent backscattering and absorption coefficients inversion of Kubelka-Munk model

With the knowledge of the **ARS** and **cri** approaches, we further verify the derivation of these coefficients from experimental reflectance and transmittance data of  $\text{Fe}_3\text{O}_4$  samples with diameters of 89 nm (denoted as NS89), 207 nm (NS207) and 458 nm (NS458), and the results are shown in Figure 6.4. The **cri** approximation assumes that the forward and backward scattering distribution are constant out to the critical angle of total reflection, and that no light scattering takes place at higher angles.

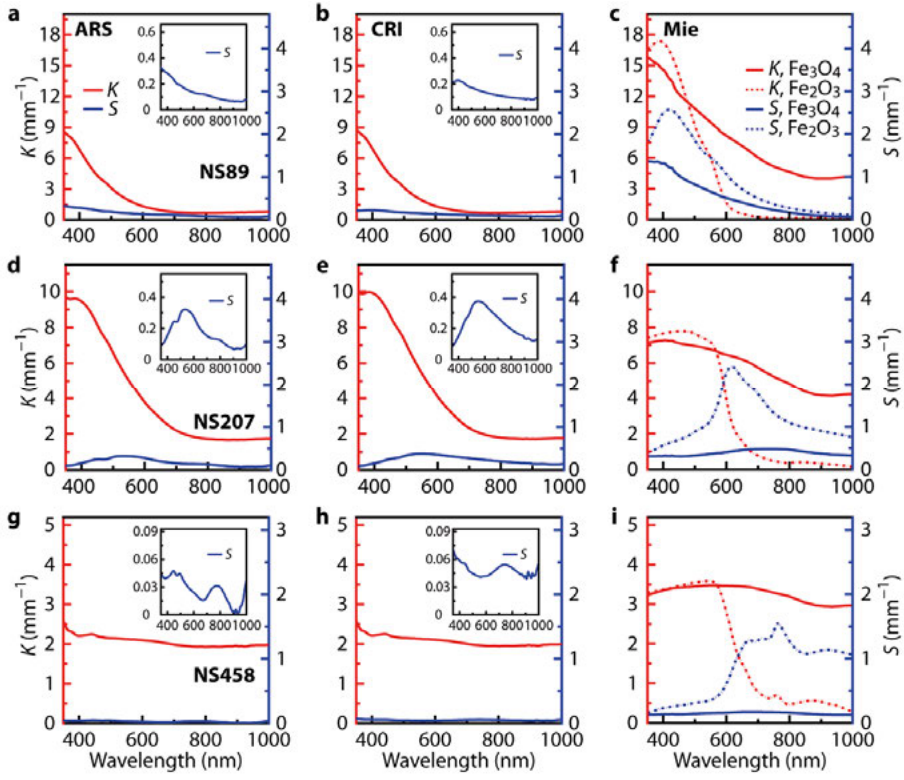


Figure 6.4. Fitted absorption coefficient  $K$  (red) and backscattering coefficient  $S$  (blue) by (a,d,g) the **ARS** and (b,e,h) **cri** methods for NS89, NS207 and NS458  $\text{Fe}_3\text{O}_4$  nanocomposite samples (insets show the backscattering coefficient  $S$  on an expanded scale). (c,e,i) Simulated  $K$  (red) and  $S$  (blue) by Mie theory for  $\text{Fe}_3\text{O}_4$  (solid) and  $\text{Fe}_2\text{O}_3$  (dotted) nanocomposites considering the particle size distributions of the NS89, NS207, and NS458 samples.

Both the **ARS** and **cri** methods converge and the calculated  $T_{\text{tot}}$  and  $R_{\text{tot}}$  reproduce the experimental results. The results from the **cri** method are shown in Figure 6.4 (b,e,h) and can be seen to be very similar to those of the **ARS** method in Figure 6.4 (a,d,g). The coefficients  $K$  and  $S$  can also be computed from single scattering Mie theory (equation 2.36 and 2.37, with unity for the effective average pathlength parameter  $\xi$ , and the forward scattering ratio  $\sigma_d$  was calculated from Mie theory). The Mie calculation takes into account the experimental size distribution of the nanoparticles and the results are shown in Figure 6.4 (c,f,i) for both the  $\text{Fe}_3\text{O}_4$  and  $\text{Fe}_2\text{O}_3$  particles. The reason for this is that an oxidized surface layer of  $\text{Fe}_2\text{O}_3$  may be present on the particles. There is no quantitative agreement between our data and the Mie simulations, probably due to effects of multiple scattering. However, qualitative similarities can be observed, most notably for the larger  $\text{Fe}_3\text{O}_4$  particles, NS458, where both  $S$  and  $K$  exhibit a similar shape to that of the Mie

simulation. For the smaller particles, the absorption shows similarities with both the  $\text{Fe}_3\text{O}_4$  and  $\text{Fe}_2\text{O}_3$  simulations, while the backscattering is in qualitative agreement with the computed one for  $\text{Fe}_3\text{O}_4$ . We assume that probably an oxidation layer is present on the small nanoparticles but has a minor influence on the larger particles. The differences in the magnitudes of  $S$  and  $K$  might be due to the particle deposition during the stabilization of the samples, as the data for as-prepared samples are closer in magnitude to the Mie simulation (Figure 6.5). It should, however, be noted that **ARS** measurements were always carried out on stabilized samples and therefore the inversion results become more uncertain for the as-prepared samples.

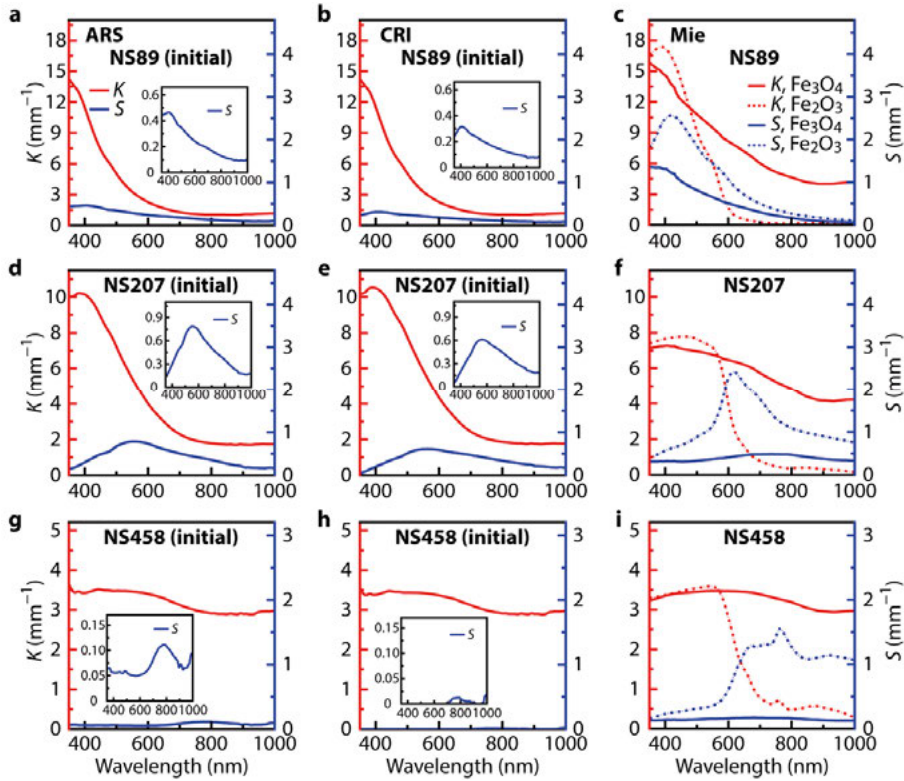


Figure 6.5. Fitted absorption coefficient  $K$  (red) and backscattering coefficient  $S$  (blue) by (a,d,g) the **ARS** and (b,e,h) **cri** methods of the NS89, NS207 and NS458  $\text{Fe}_3\text{O}_4$  nanocomposite samples in as-prepared state (Insets show a zoom-in of the backscattering coefficient  $S$ ). (c,f,i) Simulated  $K$  (red) and  $S$  (blue) by Mie theory for  $\text{Fe}_3\text{O}_4$  (solid) and  $\text{Fe}_2\text{O}_3$  (dotted) nanocomposites, considering the particle size distributions for the NS89, NS207, and NS458 samples.

## 7. Conclusions and future work

### 7.1 Conclusions

The overall aim of this work has been to develop methods for extracting scattering and absorption coefficients from transmittance and reflectance spectra. The optical properties of the scattering thin film containing functional nanoparticles (Au,  $\text{Fe}_3\text{O}_4$  and  $\text{TiO}_2$ ) were investigated by using a spectrophotometer equipped with integrating sphere, in-plane angle resolved scatterometer and out-of-plane goniometer. The particle size is of the order of the incident light, exhibiting a high scattering efficiency. Three dimensional scattering patterns of the nanoparticle composites in the forward and backward hemispheres indicated the scattering was only dependent on the polar angle, and insensitive to the azimuthal angle. Therefore, a two-dimensional in-plane scatterometer was used to characterize scattering flux as a function of angle and wavelength instead. The scattering was highly anisotropic. Scattering intensity spanned approximately seven orders of magnitude difference from the small angle regions (scattering angle  $< 2^\circ$ ) to high scattering angles close to  $90^\circ$ . We utilized filters to extend the dynamic range of our detecting system. The accuracy of the angle-resolved measurements was verified by integrating the angle-resolved results to compare with the spectra obtained from the spectrophotometer. We applied Harvey's approach to overcome the limitation of measuring angle-resolved scattering near specular reflectance regimes.

The development of the angle-resolved scheme is general for planar bulk materials containing scattering particles. In our thesis, the major purpose was to utilize this angle-resolved information to solve a problem: what is the angular light scattering distribution at front and back planar interfaces inside the film (assuming only bulk scattering without surface scattering)? We utilized Kubelka-Munk two-flux theory to solve the scattering and absorption coefficients from the input of the measured transmittance and reflectance spectra. However, knowledge of angle dependent inner interface reflectance is essential. The failure of previous attempts results from the assumption of the isotropic scattering pattern and cannot converge to the experimental transmittance and reflectance results.

In order to understand the scattering inside the film, corrections were made to convert the outer measured angle resolved results into inner scattering distribution close to the interfaces. Owing to the total internal reflectance, the

converted scattering patterns are incomplete. The scattering patterns were fitted with eight different empirical phase functions. We found that a two-term Reynolds-McCormick (TTRM) phase function provided the best fit to the experimental results. We further validated the TTRM approximation for the case of single scattering by comparing the TTRM function to calculations by Mie theory. We found that the TTRM is a good approximation for the Rayleigh and Mie scattering regimes, and can even be extended to the geometric optics regime.

The internal reflectances were obtained by integrating the whole scattering phase functions over angles, and the two-flux calculations of transmittance and reflectance were converged to the experimental data (**ARS** method). Apart from the **ARS** method, we found that results from the approximate **cri** method were very close to those of the **ARS** method. In this method it is assumed that the light scattering pattern is uniform for angles up to the critical angle of total internal reflection, and that no light scattering takes place at larger angles. The **cri** approach was verified for the convergence to experimental transmittance and reflectance spectra by Au and Fe<sub>3</sub>O<sub>4</sub> samples of varied size, shape and concentration. This approximation should be useful at least for samples containing particles of the order of or larger than the wavelength of light, where strongly forward peaked scattering patterns would be expected.

To summarize, this dissertation presents methods for evaluating scattering and absorption of coatings containing light-scattering particles that are not restricted by particle size, shape or state of aggregation. We expect that our method will be highly useful in the fields of optical coatings, displays, solar cells, metamaterials, biological materials and tissues, as well as others. Apart from nanocomposites, we also performed dark-field single particle scattering on Au, Fe<sub>3</sub>O<sub>4</sub> and TiO<sub>2</sub> nanospheres on ITO substrates, but further analysis of the spectra are required.

## 7.2 Future work

(i) Theoretical calculations for a single particle on a substrate to compare with experimental single-particle scattering spectra.

(ii) The diffuse forward and backward reflectances ( $R_{df}$ ,  $R_{db}$ ), backscattering and absorpton coefficients ( $S$  and  $K$ ) obtained by the **ARS** approach can be further applied into four-flux theory with other approximations in order to derive the intrinsic scattering and absorption coefficients ( $\alpha$  and  $\beta$ ), forward scattering ratio ( $\sigma$ ) and average pathlength parameters ( $\xi$ ). These parameters ( $\alpha$ ,  $\beta$ ,  $\sigma$ ,  $\xi$ ,  $R_c$ ,  $R_{df}$ ,  $R_{db}$ ) can be incorporated into four-flux theory to obtain simulated  $T_{tot}$ ,  $T_{reg}$ ,  $T_{dif}$ ,  $R_{tot}$ ,  $R_{reg}$ , and  $R_{dif}$  spectra that can be compared with the experimental transmittance and reflectance spectra.

(iii) Metamaterials with specially designed features, which show unique scattering performance, i.e., directional scattering can be investigated. Scattering in the infrared region is also of interest, and polarization effects can also be studied.

(iv) Explore the optical performance with optical switchable samples, where  $T(\beta)$  and  $R(\beta)$  can be tuned by the outer stimuli, i.e., temperature, electric potential and magnetic force, etc.

## 8. Swedish summary (Svensk sammanfattning)

Denna avhandling utforskar förfaranden för utvärdering av absorptions- och spridningskoefficienterna för olika material med nanopartiklar i en svagt absorberande polymermatris. Sådana material blir allt viktigare, särskilt inom energi- och optiska tillämpningar, där de möjliggör fascinerande egenskaper. De optiska egenskaperna hos tre typer av nanopartiklar: plasmoniska Au, ferromagnetiska  $\text{Fe}_3\text{O}_4$  och fotokatalytiska  $\text{TiO}_2$  med en partikelstorlek som är jämförbar med den infallande våglängden har undersökts.

Avhandlingen ger en översikt av olika tillvägagångssätt för att bestämma spridnings- och absorptionskoefficienter från experimentella transmittans- och reflektans-spektra, inklusive Monte Carlo-metoder och metoder baserade på radiativ transfer-teori. Teorierna används med de härledda spridnings- och absorptionskoefficienterna för att beräkna transmittans och reflektans. Vi tillämpade en robust två-flödes radiativ transfermodell för att bestämma absorptions- och spridningsbeteenden av de ovan nämnda funktionella nanopartiklarna inbäddade i polymera skikt. En förutsättning för att tillämpa två flödesmodellen är att man har kunskap om ljusspridningsmönstret inuti skiktet. Tidigare metoder antog ett isotropt mönster av ljusspridningen inuti filmen, men resultaten konvergerade ofta inte med experimentella transmittans och reflektionsspektra.

Vi genomförde en grundlig karakterisering av vinkel- och våglängdupplöst ljusspridning på nano-kompositerna genom användning av en spektrofotometer med integrerande sfär, en tvådimensionell ljusspridningsutrustning och en tredimensionell goniometer. Det tredimensionella spridningsmönstret från nanopartikel-kompositerna indikerade att spridningen endast var beroende av den polära vinkeln, och oberoende av den azimutala vinkeln. Därför kunde den tvådimensionella utrustningen användas för att karakterisera spridningen som funktion av vinkeln och våglängden. Spridningsmönstret var höggradigt anisotropt. Noggrannheten av de vinkelberoende mätningarna verifierades genom integrering över vinkel för att jämföra med de spektra som erhöles från spektrofotometern. Vi tillämpade Harveystrategin för att korrigera för att infallsvinkeln inte var normal i reflektansmätningarna.

För att förstå spridningen inuti filmen, omvandlades de yttre uppmätta vinkelupplösta resultaten till spridningsfördelningen nära gränsyterna inuti materialet. På grund av den totala interna reflektansen, blev det konverterade spridningsmönstret ofullständigt. Spridningsmönstren jämfördes med åtta olika empiriska funktioner. Vi fann att en två-terms Reynolds-McCormick



(TTRM) fasfunktion gav den bästa anpassningen till de experimentella resultaten. Vi validerade vidare TTRM approximationen för fallet med enpartikel-spridning genom att jämföra TTRM funktionen med beräkningar med hjälp av Mie teorin. Vi fann att TTRM är en god approximation för Rayleigh- och Miespridningsregimerna, och kan även användas i den geometriska optikregimen.

Med kännedom om spridningsmönstret inuti filmen, erhöles de inre gränsyte-reflektanserna genom integrering av hela spridningsfunktionen över vinklarna, och efter detta kan spridnings- och absorptionskoefficienterna bestämmas så att resultaten för transmittans och reflektans konvergerar till experimentella data. Denna två-flödesmodell kallar vi **ARS**-metoden. Andra modeller som kallas **cri**, **cri/dif**, **dif** och **Mi**metoderna föreslås också genom att anta olika spridningsmönster inuti filmen. Vi fann att resultaten från den ungefärliga **cri**-metoden var mycket nära dem för den exakta **ARS**-metoden. I denna metod antas det att ljusspridningsmönstret är konstant för vinklar upp till den kritiska vinkeln för total inre reflektion, och att ingen ljusspridning sker vid större vinklar. **Cri**-tillvägagångssättet verifierades genom mätningar på Au- och Fe<sub>3</sub>O<sub>4</sub>-prover med varierande partikelstorlek, form och koncentration.

Sammanfattningsvis, presenterar denna avhandling metoder för utvärdering av spridning och absorption hos beläggningar innehållande ljusspridande partiklar, som inte begränsas av partikelstorlek, form eller aggregationstillstånd. Vi förväntar oss att vår metod kommer att vara mycket användbar inom områdena optiska beläggningar, displayer, solceller, metamaterial, biologiska material och vävnader med flera. Vi utförde även optiska mätningar på enskilda på Au-, Fe<sub>3</sub>O<sub>4</sub>- och TiO<sub>2</sub>-nanosfärer belagda på ITO-substrat, men ytterligare teoretiska beräkningar krävs för att förstå dessa spektra.

# Acknowledgements

Many people have made great contributions to my research and thesis. I would like to express my greatest gratitude to:

First and foremost, my main supervisor Professor **Gunnar Niklasson**, for offering me the opportunity to pursue my Ph.D degree under your supervision. I was impressed by your profound knowledge and scientific attitude. I greatly appreciate your guidance, encouragement, enormous patience, tolerance, efficient working, and great support not only on my research but also for my life in Sweden as an international researcher. I gained lots of insights in the world of physics from you, improved my writing skills and also learned how to organize a paper in a logical way.

Thanks to my co-supervisor **Annica Nilsson**, for teaching me all the experimental skills related to optical measurements. Thanks for sharing your experience and knowledge with me on all of my projects. I wish to thank another co-supervisor, Professor **Lars Österlund**, for your input and comments on the low temperature photoluminescence project. Special thanks to Professor **Arne Roos** and **Roberta Roos**, for proof reading my thesis. **Arne** is also thanked for enabling my experiment by using your house-built angle resolved instruments. I would also like to thank Professor **Claes-Göran Granqvist**, for your advice in my professional and personal development.

Special thanks to **Daniel Fernandes**, my first roommate in Sweden, who also taught me how to use Matlab for coding my experimental data. **Chang-gang Xu**, for your sharing your experimental expertise in synthesizing nanoparticles and great co-working experience. **Mattias Strömberg**, for providing your support and input to my research. Many thanks for my previous supervisor in Hong Kong, Professor **Jianfang Wang**, for your continuous support to my academic career and providing samples for my research. My colleague in Hong Kong, **Xiaolu Zhuo**, for the single particle scattering measurements.

Also thanks to **Andreas Mattsson**, for your technical assistance on lab instruments. **David Langhammer**, for inspiring co-working experience on the photoluminescence project. **Daniel Hedlund**, for your magnetic measurements. **José Montero Amenedo**, **Idris Sorar**, and **Sofia Kontos**, it is my great pleasure to work with you in the same office. **José** is also thanked for sharing Mie scattering codes to me. **Sofia** is thanked for checking my summary in Swedish. **Zhen Qiu**, **Bo Tian**, **Yuxia Ji**, **Ruitao Wen**, **Huiying Qu**, **Xiaoqi Liao** and **Hui Xiong** are appreciated for sharing the coffee time together. Thank you **Bengt Götesson**, for a great time in the department.

Thanks to my colleagues, Professor **Tomas Edvinsson, Ilknur Bayrak Pehlivan, Mohammad Ziaur Rahman, Edgar Rojas, Henry Stopfel, Jakob Thyr, Seda Ulusoy, Serkan Akansel, Umut Çindemir, David Lingfors** for nice conversations and company in the same department. Many thanks to **Jiaojiao Yang, Shuyi Li, Wei Wei, Shihuai Wang, Xin Chen, Hua Wu, Yuanyuan Han, Dan Wu, Le Fu, Mengying Ren, Liyang Shi, Bo Xu, Yanran Zhao, Minzhi Jiao, Gaoyang Dai, Zhicheng Wang, Ruijun Pan, Ling Xie, Shuangshuang Zeng, Shijun Wang, Yang Hu, Beichen Xie, Lei You, Juan Le, Xia Chu, Xinxin Xu, Yu Tian, Yan Shao, Xin Li, Yu Liu, Hailiang Fang, Hao Cao, Chenjuan Liu, Xiao Yang, Yukai Yang, Jingying Yang, Xiaofang Cao, Jie Yang, Yiqing Wang, Zhaolun Fan** for the friendship and support.

Last but not the least, the most important support to my PhD study is from my parents, so please let me use my native language to express my gratitude to them:

谢谢爸爸妈妈，谢谢你们一直以来对我的支持，鼓励和包容！

# References

- (1) Curiel, F.; Vargas, W. E.; Barrera, R. G. Visible spectral dependence of the scattering and absorption coefficients of pigmented coatings from inversion of diffuse reflectance spectra. *Appl. Opt.* **2002**, *41*, 5969-5978.
- (2) Levinson, R.; Berdahl, P.; Akbari, H. Solar spectral optical properties of pigments—Part I: model for deriving scattering and absorption coefficients from transmittance and reflectance measurements. *Sol. Energy Mater. Sol. Cells* **2005**, *89*, 319-349.
- (3) Levinson, R.; Berdahl, P.; Akbari, H. Solar spectral optical properties of pigments—Part II: survey of common colorants. *Sol. Energy Mater. Sol. Cells* **2005**, *89*, 351-389.
- (4) Vargas, W. E.; Amador, A.; Niklasson, G. A. Diffuse reflectance of TiO<sub>2</sub> pigmented paints: Spectral dependence of the average pathlength parameter and the forward scattering ratio. *Opt. Commun.* **2006**, *261*, 71-78.
- (5) Meretska, M. L.; Uppu, R.; Vissenberg, G.; Lagendijk, A.; Ijzerman, W. L.; Vos, W. L. Analytical modeling of light transport in scattering materials with strong absorption. *Opt. Express* **2017**, *25*, A906-A921.
- (6) Islam, K.; Alnuaimi, A.; Battal, E.; Okay, A. K.; Nayfeh, A. Effect of gold nanoparticles size on light scattering for thin film amorphous-silicon solar cells. *Solar Energy* **2014**, *103*, 263-268.
- (7) Arinze, E. S.; Qiu, B.; Nyirjesy, G.; Thon, S. M. Plasmonic Nanoparticle Enhancement of Solution-Processed Solar Cells: Practical Limits and Opportunities. *ACS Photonics* **2016**, *3*, 158-173.
- (8) Carretero-Palacios, S.; Jiménez-Solano, A.; Míguez, H. Plasmonic Nanoparticles as Light-Harvesting Enhancers in Perovskite Solar Cells: A User's Guide. *ACS Energy Lett.* **2016**, *1*, 323-331.
- (9) Duan, X.; Kamin, S.; Liu, N. Dynamic plasmonic colour display. *Nat. Commun.* **2017**, *8*, 14606.
- (10) Novotny, L.; van Hulst, N. Antennas for light. *Nat. Photon.* **2011**, *5*, 83.
- (11) Shen, Y.; Zhou, J.; Liu, T.; Tao, Y.; Jiang, R.; Liu, M.; Xiao, G.; Zhu, J.; Zhou, Z.-K.; Wang, X.; Jin, C.; Wang, J. Plasmonic gold mushroom arrays with refractive index sensing figures of merit approaching the theoretical limit. *Nat. Commun.* **2013**, *4*, 2381.
- (12) Kuznetsov, A. I.; Miroshnichenko, A. E.; Brongersma, M. L.; Kivshar, Y. S.; Luk'yanchuk, B. Optically resonant dielectric nanostructures. *Science* **2016**, *354*.
- (13) Yang, Z.-J.; Jiang, R.; Zhuo, X.; Xie, Y.-M.; Wang, J.; Lin, H.-Q. Dielectric nanoresonators for light manipulation. *Phys. Rep.* **2017**, *701*, 1-50.
- (14) Manuel, D.; Isabelle, S. Resonant dielectric nanostructures: a low-loss platform for functional nanophotonics. *J. Opt.* **2016**, *18*, 103001.
- (15) Lee, H.; Shin, T.-H.; Cheon, J.; Weissleder, R. Recent Developments in Magnetic Diagnostic Systems. *Chem. Rev.* **2015**, *115*, 10690-10724.

- (16) Egerton, T. A.; Tooley, I. R. UV absorption and scattering properties of inorganic-based sunscreens. *Int. J. Cosmet. Sci.* **2012**, *34*, 117-122.
- (17) Schneider, J.; Matsuoka, M.; Takeuchi, M.; Zhang, J.; Horiuchi, Y.; Anpo, M.; Bahnemann, D. W. Understanding TiO<sub>2</sub> Photocatalysis: Mechanisms and Materials. *Chem. Rev.* **2014**, *114*, 9919-9986.
- (18) Bach, U.; Corr, D.; Lupo, D.; Pichot, F.; Ryan, M. Nanomaterials-Based Electrochromics for Paper-Quality Displays. *Adv. Mater.* **2002**, *14*, 845-848.
- (19) Al-Attafi, K.; Nattestad, A.; Yamauchi, Y.; Dou, S. X.; Kim, J. H. Aggregated mesoporous nanoparticles for high surface area light scattering layer TiO<sub>2</sub> photoanodes in Dye-sensitized Solar Cells. *Sci Rep* **2017**, *7*, 10341.
- (20) Jonsson, J. C.; Smith, G. B.; Deller, C.; Roos, A. Directional and angle-resolved optical scattering of high-performance translucent polymer sheets for energy-efficient lighting and skylights. *Appl. Opt.* **2005**, *44*, 2745-2753.
- (21) Koziej, D.; Fischer, F.; Kränzlin, N.; Caseri, W. R.; Niederberger, M. Nonaqueous TiO<sub>2</sub> Nanoparticle Synthesis: a Versatile Basis for the Fabrication of Self-Supporting, Transparent, and UV-Absorbing Composite Films. *ACS Appl. Mater. Interfaces* **2009**, *1*, 1097-1104.
- (22) Zhai, Y.; Ma, Y.; David, S. N.; Zhao, D.; Lou, R.; Tan, G.; Yang, R.; Yin, X. Scalable-manufactured randomized glass-polymer hybrid metamaterial for daytime radiative cooling. *Science* **2017**.
- (23) Zhang, Y.; Liu, Q.; Mundoor, H.; Yuan, Y.; Smalyukh, I. I. Metal Nanoparticle Dispersion, Alignment, and Assembly in Nematic Liquid Crystals for Applications in Switchable Plasmonic Color Filters and E-Polarizers. *ACS Nano* **2015**, *9*, 3097-3108.
- (24) Rao, V. K.; Radhakrishnan, T. P. Tuning the SERS Response with Ag-Au Nanoparticle-Embedded Polymer Thin Film Substrates. *ACS Appl. Mater. Interfaces* **2015**, *7*, 12767-12773.
- (25) Kim, S. B.; Cai, C.; Sun, S.; Sweigart, D. A. Incorporation of Fe<sub>3</sub>O<sub>4</sub> Nanoparticles into Organometallic Coordination Polymers by Nanoparticle Surface Modification. *Angew. Chem. Int. Ed.* **2009**, *48*, 2907-2910.
- (26) Lü, C.; Cui, Z.; Guan, C.; Guan, J.; Yang, B.; Shen, J. Research on Preparation, Structure and Properties of TiO<sub>2</sub>/Polythiourethane Hybrid Optical Films with High Refractive Index. *Macromol. Mater. Eng.* **2003**, *288*, 717-723.
- (27) Niklasson, G. A.; Granqvist, C. G.; Hunderi, O. Effective medium models for the optical properties of inhomogeneous materials. *Appl. Opt.* **1981**, *20*, 26-30.
- (28) Aspnes, D. E. Local-field effects and effective-medium theory: A microscopic perspective. *Am. J. Phys.* **1982**, *50*, 704-709.
- (29) Azzam, R. M. A.; Bashara, N. M., *Ellipsometry and polarized light*. North-Holland Pub. Co.. Amsterdam: 1977.
- (30) Barrios, D.; Vergaz, R.; Sanchez-Pena, J. M.; Granqvist, C. G.; Niklasson, G. A. Toward a quantitative model for suspended particle devices: Optical scattering and absorption coefficients. *Sol. Energy Mater. Sol. Cells* **2013**, *111*, 115-122.
- (31) Hulst, H. C., *Light Scattering by Small Particles*, New York. Wiley: 1957.
- (32) Bohren, C.; Huffman, D. R., *Absorption and Scattering of Light by Small Particles*. John Wiley & Sons, New York: 1998.
- (33) Tien, C. L.; Drolen, B. L., Thermal radiation in particulate media with dependent and independent scattering. In *Annual review of numerical fluid mechanics and heat transfer*. Washington, DC, Hemisphere Publishing Corp., 1987; Vol. 1, pp 1-32.
- (34) Mie, G. Beiträge zur Optik trüber Medien, speziell kolloidaler Metallösungen. *Annalen der Physik* **1908**, *330*, 377-445.

- (35) Niklasson, G. A., *Modeling the optical properties of nanoparticles*. SPIE Newsroom: 2006.
- (36) Hottel, H. C.; Sarofim, A. F.; Dalzell, W. H.; Vasalos, I. A. Optical Properties of Coatings. Effect of Pigment Concentration. *AIChE Journal* **1971**, *9*, 1895-1898.
- (37) Ishimaru, A., *Wave Propagation and Scattering in Random Media*. Wiley, San Diego: 1999.
- (38) Niklasson, G. A.; Granqvist, C. G. Optical properties and solar selectivity of coevaporated Co-Al<sub>2</sub>O<sub>3</sub> composite films. *J. Appl. Phys.* **1984**, *55*, 3382-3410.
- (39) Maxwell Garnett, J. C. Colours in Metal Glasses and in Metallic Films. *Philos. Trans. R. Soc. London, Ser. A* **1904**, *203*, 385-420.
- (40) Maxwell Garnett, J. C. VII. Colours in metal glasses, in metallic films, and in metallic solutions.—II. *Philos. Trans. R. Soc. London, Ser. A* **1906**, *205*, 237-288.
- (41) Bruggeman, D. A. G. Berechnung verschiedener physikalischer Konstanten von heterogenen Substanzen. I. Dielektrizitätskonstanten und Leitfähigkeiten der Mischkörper aus isotropen Substanzen. *Annalen der Physik* **1935**, *416*, 636-664.
- (42) Mishchenko, M. I.; Travis, L. D.; Mackowski, D. W. T-matrix computations of light scattering by nonspherical particles: A review. *J. Quant. Spectrosc. Radiat. Transfer* **1996**, *55*, 535-575.
- (43) Draine, B. T.; Flatau, P. J. Discrete-Dipole Approximation For Scattering Calculations. *J. Opt. Soc. Am. A* **1994**, *11*, 1491-1499.
- (44) Yurkin, M. A.; Hoekstra, A. G. The discrete dipole approximation: an overview and recent developments. *J. Quant. Spectrosc. Radiat. Transf.* **2007**, *106*, 558-589.
- (45) Volakis, J. L.; Chatterjee, A.; Kempel, L. C. Review of the finite-element method for three-dimensional electromagnetic scattering. *J. Opt. Soc. Am. A* **1994**, *11*, 1422-1433.
- (46) Wriedt, T.; Doicu, A. Formulations of the extended boundary condition method for three-dimensional scattering using the method of discrete sources. *J. Mod. Opt.* **1998**, *45*, 199-213.
- (47) Babar, S.; Weaver, J. H. Optical constants of Cu, Ag, and Au revisited. *Appl. Opt.* **2015**, *54*, 477-481.
- (48) Vargas, W. E.; Niklasson, G. A. Light-scattering from particles. . In: *Encyclopedia of surface and colloid science*. New York: Marcel Dekker; **2002**, 3044-3056.
- (49) Sarkar, B.; Alexandridis, P. Block copolymer–nanoparticle composites: Structure, functional properties, and processing. *Prog. Polym. Sci.* **2015**, *40*, 33-62.
- (50) Zhai, Y.; Ma, Y.; David, S. N.; Zhao, D.; Lou, R.; Tan, G.; Yang, R.; Yin, X. Scalable-manufactured randomized glass-polymer hybrid metamaterial for daytime radiative cooling. *Science* **2017**, *355*, 1062-1066.
- (51) Liang, X.; Li, M.; Lu, J. Q.; Huang, C.; Feng, Y.; Sa, Y.; Ding, J.; Hu, X.-H. Spectrophotometric determination of turbid optical parameters without using an integrating sphere. *Appl. Opt.* **2016**, *55*, 2079-2085.
- (52) Levine, Z. H.; Streater, R. H.; Lieberman, A.-M. R.; Pinter, A. L.; Cooksey, C. C.; Lemailet, P. Algorithm for rapid determination of optical scattering parameters. *Opt. Express* **2017**, *25*, 26728-26746.
- (53) Leyre, S.; Leloup, F. B.; Audenaert, J.; Durinck, G.; Hofkens, J.; Deconinck, G.; Hanselaer, P. Determination of the bulk scattering parameters of diffusing materials. *Appl. Opt.* **2013**, *52*, 4083-4090.

- (54) Herman, B. M.; Browning, S. R. A Numerical Solution to the Equation of Radiative Transfer. *J. Atmos. Sci.* **1965**, *22*, 559-566.
- (55) Haskell, R. C.; Svaasand, L. O.; Tsay, T.-T.; Feng, T.-C.; McAdams, M. S.; Tromberg, B. J. Boundary conditions for the diffusion equation in radiative transfer. *J. Opt. Soc. Am. A* **1994**, *11*, 2727-2741.
- (56) I. Frankel, J. Computational attributes of the integral form of the equation of transfer. *J. Quant. Spectrosc. Radiat. Transfer* **1991**, *46*, 329-342.
- (57) Van De Hulst, H. C., *Multiple light scattering. Tables, formulas and applications*. Academic Press, New York: 1980.
- (58) Raeside, D. E. Monte Carlo principles and applications. *Phys. Med. Biol* **1976**, *21*, 181.
- (59) Briton, J.-P.; Maheu, B.; Gréhan, G.; Gouesbet, G. Monte Carlo Simulation of Multiple Scattering in arbitrary 3-D geometry. *Part. Part. Syst. Char.* **1992**, *9*, 52-58.
- (60) Graaff, R.; Koelink, M. H.; de Mul, F. F. M.; Zijlstra, W. G.; Dassel, A. C. M.; Aarnoudse, J. G. Condensed Monte Carlo simulations for the description of light transport. *Appl. Opt.* **1993**, *32*, 426-434.
- (61) Wang, L. V. Rapid modeling of diffuse reflectance of light in turbid slabs. *J. Opt. Soc. Am. A* **1998**, *15*, 936-944.
- (62) Mudgett, P. S.; Richards, L. W. Multiple Scattering Calculations for Technology. *Appl. Opt.* **1971**, *10*, 1485-1502.
- (63) Mudgett, P. S.; Richards, L. W. Multiple scattering calculations for technology II. *J. Colloid Interface Sci.* **1972**, *39*, 551-567.
- (64) Kuhn, J.; Korder, S.; Arduini - Schuster, M. C.; Caps, R.; Fricke, J. Infrared - optical transmission and reflection measurements on loose powders. *Rev. Sci. Instrum.* **1993**, *64*, 2523-2530.
- (65) Schuster, A. Radiation through a foggy atomosphere. *Astrophys J.* **1905**, *21*, 1-22.
- (66) Schwarzschild, K. Ueber das Gleichgewicht der Sonnenatmosphäre. *Nachrichten von der Gesellschaft der Wissenschaften zu Göttingen, Mathematisch-Physikalische Klasse* **1906**, *1906*, 41-53.
- (67) Kubelka, P. Ein beitrag zur optik der farbanstriche. *Z tech Phys.* **1931**, *12*, 593-601.
- (68) Kubelka, P. New Contributions to the Optics of Intensely Light-Scattering Materials. Part I. *J. Opt. Soc. Am.* **1948**, *38*, 448-457.
- (69) Brewster, M. Q.; Tien, C. L. Examination of the two-flux model for radiative transfer in particular systems. *Int. J. Heat Mass Transfer* **1982**, *25*, 1905-1907.
- (70) The scattering of light by turbid media.—Part I. *Proceedings of the Royal Society of London. Series A* **1931**, *131*, 451-464.
- (71) Reichman, J. Determination of Absorption and Scattering Coefficients for Nonhomogeneous Media. 1: Theory. *Appl. Opt.* **1973**, *12*, 1811-1815.
- (72) Maheu, B.; Letoulouzan, J. N.; Gouesbet, G. Four-flux models to solve the scattering transfer equation in terms of Lorenz-Mie parameters. *Appl. Opt.* **1984**, *23*, 3353-3362.
- (73) Chu, C.-M.; Churchill, S. W. Numerical Solution of Problems in Multiple Scattering of Electromagnetic Radiation. *J. Phys. Chem.* **1955**, *59*, 855-863.
- (74) Niklasson, G. A. Comparison between four flux theory and multiple scattering theory. *Appl. Opt.* **1987**, *26*, 4034-4036.
- (75) Vargas, W. E.; Niklasson, G. A. Forward average path-length parameter in four-flux radiative transfermodels. *Appl. Opt.* **1997**, *36*, 3735-3738.

- (76) William, E. V.; Gunnar, A. N. Forward-scattering ratios and average path-length parameter in radiative transfer models. *J. Phys.: Condens. Matter* **1997**, *9*, 9083.
- (77) Vargas, W. E. Two-flux radiative transfer model under nonisotropic propagating diffuseradiation. *Appl. Opt.* **1999**, *38*, 1077-1085.
- (78) Stover, J. C., *Optical scattering : measurement and analysis*. SPIE Optical Engineering Press: Bellingham, Wash., USA, 1995.
- (79) von Finck, A.; Trost, M.; Schröder, S.; Duparré, A. Parallelized multichannel BSDF measurements. *Opt. Express* **2015**, *23*, 33493-33505.
- (80) Nicodemus, F. E.; Richmond, J. C.; Hsia, J. J.; Ginsberg, I. W.; Limperis, T., Geometrical considerations and nomenclature for reflectance. In *Radiometry*, Jones and Bartlett Publishers, Inc., USA: 1977; pp 94-145.
- (81) Standard practice for goniometric optical scatter measurements. *Am. Soc. Test. Mater.* **2011**, *ASTM E2387-05*.
- (82) Seinfeld, J. H.; Pandis, S. N., *Atmospheric Chemistry and Physics: From Air Pollution to Climate Change. 2nd Edition*. John Wiley & Sons, New York: 2006.
- (83) Bohren, C. F.; Huffman, D. R., *Absorption and scattering of light by small particles*. Wiley, New York: 1983.
- (84) Reynolds, L. O.; McCormick, N. J. Approximate two-parameter phase function for light scattering. *J. Opt. Soc. Am.* **1980**, *70*, 1206-1212.
- (85) Henyey, L. C.; Greenstein, J. L. Diffuse radiation in the galaxy. *Astrophys. J.* **1941**, *93*, 70-83.
- (86) Cornette, W. M.; Shanks, J. G. Physically reasonable analytic expression for the single-scattering phase function. *Appl. Opt.* **1992**, *31*, 3152-3160.
- (87) Haltrin, V. I. One-parameter two-term Henyey-Greenstein phase function for light scattering in seawater. *Appl. Opt.* **2002**, *41*, 1022-1028.
- (88) Fournier, G. R.; Forand, J. L. Analytic phase function for ocean water. *Proc SPIE* **1994**, *2258*, 194-201.
- (89) Germer, T. A.; Zwinkels, J. C.; Tsai, B. K. Spectrophotometry: accurate measurement of optical properties of materials. *Experimental methods in the physical sciences* **2014**, *46*.
- (90) Ruan, Q.; Shao, L.; Shu, Y.; Wang, J.; Wu, H. Growth of monodisperse gold nanospheres with diameters from 20 nm to 220 nm and their core/satellite nanostructures. *Adv. Opt. Mater.* **2014**, *2*, 65-73.
- (91) Han, C.; Luque, R.; Dionysiou, D. D. Facile preparation of controllable size monodisperse anatase titania nanoparticles. *Chem. Commun.* **2012**, *48*, 1860-1862.
- (92) Berne, B. J.; Pecora, R., *Dynamic light scattering*. John Wiley & Sons Inc., New York: 1976.
- (93) Brown, W., *Dynamic light scattering - The method and some applications*. Oxford University Press Inc., New York: 1993.
- (94) Harvey, J. E. Surface scatter phenomena: a linear, shift-invariant process. *Proc SPIE* **1990**, *1165*, 87-99.
- (95) Zhuo, X.; Yip, H. K.; Ruan, Q.; Zhang, T.; Zhu, X.; Wang, J.; Lin, H.-Q.; Xu, J.-B.; Yang, Z. Broadside Nanoantennas Made of Single Silver Nanorods. *ACS Nano* **2018**, *12*, 1720-1731.
- (96) Qin, F.; Cui, X.; Ruan, Q.; Lai, Y.; Wang, J.; Ma, H.; Lin, H.-Q. Role of shape in substrate-induced plasmonic shift and mode uncovering on gold nanocrystals. *Nanoscale* **2016**, *8*, 17645-17657.



- (97) Zhang, S.; Jiang, R.; Xie, Y.-M.; Ruan, Q.; Yang, B.; Wang, J.; Lin, H.-Q. Colloidal Moderate-Refractive-Index  $\text{Cu}_2\text{O}$  Nanospheres as Visible-Region Nanoantennas with Electromagnetic Resonance and Directional Light-Scattering Properties. *Adv. Mater.* **2015**, *27*, 7432-7439.
- (98) Xiang, B.; Jiang, G.; Zhang, J. Surface modification of  $\text{TiO}_2$  nanoparticles with silane coupling agent for nanocomposite with poly(butyl acrylate). *Plast. Rubber Compos.* **2015**, *44*, 148-154.
- (99) Hu, M.; Chen, J.; Li, Z.-Y.; Au, L.; Hartland, G. V.; Li, X.; Marquez, M.; Xia, Y. Gold nanostructures: engineering their plasmonic properties for biomedical applications. *Chem. Soc. Rev.* **2006**, *35*, 1084-1094.
- (100) Schlegel, A.; Alvarado, S. F.; Wachter, P. Optical properties of magnetite ( $\text{Fe}_3\text{O}_4$ ). *J. Phys. C: Solid State Phys.* **1979**, *12*, 1157-1164.
- (101) Miao, L.; Jin, P.; Kaneko, K.; Terai, A.; Nabatova-Gabain, N.; Tanemura, S. Preparation and characterization of polycrystalline anatase and rutile  $\text{TiO}_2$  thin films by rf magnetron sputtering. *Appl. Surf. Sci.* **2003**, *212-213*, 255-263.
- (102) Germer, T. A.; Zwinkels, J. C.; Tsai, B. K., *Spectrophotometry: Accurate measurement of optical properties of materials*. Elsevier Science: Amsterdam ;, 2014.
- (103) Videen, G. Light scattering from a particle on or near a perfectly conducting surface. *Opt. Commun.* **1995**, *115*, 1-7.
- (104) Videen, G. Light scattering from a sphere on or near a surface: errata. *J. Opt. Soc. Am. A* **1992**, *9*, 844-845.
- (105) Videen, G. Light scattering from a sphere on or near a surface. *J. Opt. Soc. Am. A* **1991**, *8*, 483-489.
- (106) Bobbert, P. A.; Vlieger, J. Light scattering by a sphere on a substrate. *Physica A Stat. Mech. Appl.* **1986**, *137*, 209-242.
- (107) Bohren, C. F. Multiple scattering of light and some of its observable consequences. *Am. J. Phys.* **1987**, *55*, 524-533.
- (108) Vargas, W. E.; Niklasson, G. A. Applicability conditions of the Kubelka-Munk theory. *Appl. Opt.* **1997**, *36*, 5580-5586.
- (109) Patterson, E. M.; Shelden, C. E.; Stockton, B. H. Kubelka-Munk optical properties of a barium sulfate white reflectance standard. *Appl. Opt.* **1977**, *16*, 729-732.
- (110) Edstr, P. A Fast and Stable Solution Method for the Radiative Transfer Problem. *SIAM Rev.* **2005**, *47*, 447-468.
- (111) Judd, D. B. Fresnel reflection of diffusely incident light. *J. Res. Nat. Bur. Stand.* **1942**, *29*, 329-332.

# Acta Universitatis Upsaliensis

*Digital Comprehensive Summaries of Uppsala Dissertations  
from the Faculty of Science and Technology 1767*

Editor: The Dean of the Faculty of Science and Technology

A doctoral dissertation from the Faculty of Science and Technology, Uppsala University, is usually a summary of a number of papers. A few copies of the complete dissertation are kept at major Swedish research libraries, while the summary alone is distributed internationally through the series Digital Comprehensive Summaries of Uppsala Dissertations from the Faculty of Science and Technology. (Prior to January, 2005, the series was published under the title "Comprehensive Summaries of Uppsala Dissertations from the Faculty of Science and Technology".)



ACTA  
UNIVERSITATIS  
UPSALIENSIS  
UPPSALA  
2019

Distribution: [publications.uu.se](http://publications.uu.se)  
urn:nbn:se:uu:diva-374319